N°d'ordre NNT : 2019LYSEI102

THESE de DOCTORAT DE L'UNIVERSITE DE LYON
opérée au sein de
INSA Lyon, CREATIS
CEA, LETI

Ecole Doctorale N° 160
Électronique, Électrotechnique, Automatique (EEA)

Spécialité de doctorat : Traitement du Signal et de l'Image

Soutenue publiquement le 22/11/2019, par :
Odran PIVOT

Scatter correction for spectral computed tomography

Devant le jury composé de :

RODET, Thomas	Professeur (ENS CACHAN)	Président
BUVAT, Irène	Directeur de recherche (Université Paris Sud)	Rapporteure
MAIER, Andreas	Professeur (FAU Erlangen-Nürnberg)	Rapporteur
DESBAT, Laurent	Professeur (Université Grenoble Alpes)	Examinateur
LÉTANG, Jean Michel	Maître de Conférences HDR (INSA Lyon)	Directeur de thèse
FOURNIER, Clarisse	Ingénieur chercheur (CEA/LETI)	Invitée
TABARY, Joachim	Ingénieur chercheur (CEA/LETI)	Invité
RIT, Simon	Chargé de recherche (CNRS)	Invité

Département FEDORA – INSA Lyon - Ecoles Doctorales – Quinquennal 2016-2020

SIGLE	ECOLE DOCTORALE	NOM ET COORDONNEES DU RESPONSABLE
CHIMIE	**CHIMIE DE LYON** **http://www.edchimie-lyon.fr** Sec. : Renée EL MELHEM Bât. Blaise PASCAL, 3e étage **secretariat@edchimie-lyon.fr** INSA : R. GOURDON	M. Stéphane DANIELE Institut de recherches sur la catalyse et l'environnement de Lyon IRCELYON-UMR 5256 Équipe CDFA 2 Avenue Albert EINSTEIN 69 626 Villeurbanne CEDEX **directeur@edchimie-lyon.fr**
E.E.A.	**ÉLECTRONIQUE, ÉLECTROTECHNIQUE, AUTOMATIQUE** **http://edeea.ec-lyon.fr** Sec. : M.C. HAVGOUDOUKIAN **ecole-doctorale.eea@ec-lyon.fr**	M. Gérard SCORLETTI École Centrale de Lyon 36 Avenue Guy DE COLLONGUE 69 134 Écully Tél : 04.72.18.60.97 Fax 04.78.43.37.17 **gerard.scorletti@ec-lyon.fr**
E2M2	**ÉVOLUTION, ÉCOSYSTÈME, MICROBIOLOGIE, MODÉLISATION** **http://e2m2.universite-lyon.fr** Sec. : Sylvie ROBERJOT Bât. Atrium, UCB Lyon 1 Tél : 04.72.44.83.62 INSA : H. CHARLES **secretariat.e2m2@univ-lyon1.fr**	M. Philippe NORMAND UMR 5557 Lab. d'Ecologie Microbienne Université Claude Bernard Lyon 1 Bâtiment Mendel 43, boulevard du 11 Novembre 1918 69 622 Villeurbanne CEDEX **philippe.normand@univ-lyon1.fr**
EDISS	**INTERDISCIPLINAIRE SCIENCES-SANTÉ** **http://www.ediss-lyon.fr** Sec. : Sylvie ROBERJOT Bât. Atrium, UCB Lyon 1 Tél : 04.72.44.83.62 INSA : M. LAGARDE **secretariat.ediss@univ-lyon1.fr**	Mme Emmanuelle CANET-SOULAS INSERM U1060, CarMeN lab, Univ. Lyon 1 Bâtiment IMBL 11 Avenue Jean CAPELLE INSA de Lyon 69 621 Villeurbanne Tél : 04.72.68.49.09 Fax : 04.72.68.49.16 **emmanuelle.canet@univ-lyon1.fr**
INFOMATHS	**INFORMATIQUE ET MATHÉMATIQUES** **http://edinfomaths.universite-lyon.fr** Sec. : Renée EL MELHEM Bât. Blaise PASCAL, 3e étage Tél : 04.72.43.80.46 **infomaths@univ-lyon1.fr**	M. Hamamache KHEDDOUCI Bât. Nautibus 43, Boulevard du 11 novembre 1918 69 622 Villeurbanne Cedex France Tel : 04.72.44.83.69 **hamamache.kheddouci@univ-lyon1.fr**
Matériaux	**MATÉRIAUX DE LYON** **http://ed34.universite-lyon.fr** Sec. : Stéphanie CAUVIN Tél : 04.72.43.71.70 Bât. Direction **ed.materiaux@insa-lyon.fr**	M. Jean-Yves BUFFIÈRE INSA de Lyon MATEIS - Bât. Saint-Exupéry 7 Avenue Jean CAPELLE 69 621 Villeurbanne CEDEX Tél : 04.72.43.71.70 Fax : 04.72.43.85.28 **jean-yves.buffiere@insa-lyon.fr**
MEGA	**MÉCANIQUE, ÉNERGÉTIQUE, GÉNIE CIVIL, ACOUSTIQUE** **http://edmega.universite-lyon.fr** Sec. : Stéphanie CAUVIN Tél : 04.72.43.71.70 Bât. Direction **mega@insa-lyon.fr**	M. Jocelyn BONJOUR INSA de Lyon Laboratoire CETHIL Bâtiment Sadi-Carnot 9, rue de la Physique 69 621 Villeurbanne CEDEX **jocelyn.bonjour@insa-lyon.fr**
ScSo	ScSo* **http://ed483.univ-lyon2.fr** Sec. : Véronique GUICHARD INSA : J.Y. TOUSSAINT Tél : 04.78.69.72.76 **veronique.cervantes@univ-lyon2.fr**	M. Christian MONTES Université Lyon 2 86 Rue Pasteur 69 365 Lyon CEDEX 07 **christian.montes@univ-lyon2.fr**

*ScSo : Histoire, Géographie, Aménagement, Urbanisme, Archéologie, Science politique, Sociologie, Anthropologie

Abstract

Scattered radiation is a major cause of bias, loss of contrast and artifacts in x-ray computed tomography (CT). Many correction methods have been proposed for conventional CT (using energy-integrating detectors) but it is still an open research topic in the field of spectral CT, a novel imaging technique based on the use of energy-selective photon counting detectors. The main objective of the present thesis was to investigate scatter correction techniques adapted to spectral CT. The chosen solution refines a scatter correction method developed for integration-mode CT which uses a semi-transparent primary modulator mask. The attenuation of the primary modulator mask is first compensated for with a correction matrix which takes advantage of the spectral information. The other contributions are a scatter model based on B-splines allowing an accurate representation of scatter maps with the aid of a very few parameters and a cost function which takes into account the structures of the mask and the object. The accuracy of the correction matrix, the scatter model and the whole proposed scatter correction process were tested on simulated data considering photon counting detectors with various numbers of energy bins and have shown a significant bias reduction, contrast enhancement and artifact removal. In addition, physical experiments were performed using a parallel fan-beam set-up with a commercial energy- resolved detector. The method was successfully validated in the case of two phantoms dedicated to medical image quality measurements, with a remarkable improvement.

Notation

Throughout this manuscript, vectors and matrices are in bold face unlike scalars. In general, vectors are in lower case while matrices in upper case, except for vectors representing intensity images or images in number of photons. In addition, estimated scalars and vectors are represented with a tilde on top of the letters and vectors representing modulated images with a hat.

Symbol	Description
N_E	Number of energy samples (discretization of the energy range)
N_B	Number of energy bins
N_U	Number of pixels of the detector in the u direction
N_V	Number of pixels of the detector in the v direction
N_Θ	Number of projection angles
$e \in [1; N_E]$	Energy index
$b \in [1; N_B]$	Energy bin index
$u \in [1; N_U]$	Pixel index in the u direction
$v \in [1; N_V]$	Pixel index in the v direction
$\theta \in [1; N_\Theta]$	Projection angle index
$\boldsymbol{\lambda}_\theta$	Source position
$\boldsymbol{\zeta}_{u,v,\theta}$	Unit vector from the source onto pixel (u, v)
$\boldsymbol{N}^{0,i}$	Number of incident photons without object
$\boldsymbol{N}^{p,i}$	Number of incident primary photons
$\boldsymbol{N}^{s,i}$	Number of incident scattered photons
$\boldsymbol{N}^{t,i}$	Total number of incident photons
$\boldsymbol{N}^0$	Number of detected photons without object
$\boldsymbol{N}^p$	Number of detected primary photons
$\boldsymbol{N}^s$	Number of detected scattered photons
$\boldsymbol{N}^t$	Total number of detected photons
$\boldsymbol{p}$	Primary transmission
$\boldsymbol{s}$	Scatter transmission
$\boldsymbol{t}$	Total transmission
$\boldsymbol{g}^p$	Primary attenuation
$\boldsymbol{g}^t$	Total attenuation
$\boldsymbol{f}^p$	Reconstructed primary
$\boldsymbol{f}^t$	Reconstructed total

Contents

1

Introduction

Transmission x-ray computed tomography (CT) is widely used in the context of medical imaging. Since the invention of the CT scanner by Godfrey Hounsfield in 1971, significant improvements have been made on both the hardware, e.g., x-ray tubes, collimators, rotation systems and detectors, and the software with the development of numerous reconstruction algorithms and artifacts removal techniques.

Recently, the emergence of photon counting detectors (PCD), a new detection technology based on the use of semi-conductor materials, enables to count photons and to classify them into discrete bins according to their energy. This new detection technology (with 2 to 8 energy bins) equips a few medical prototypes of whole body CT system and is currently evaluated in clinical research facilities. For other industrial applications, some linear PCDs have up to a hundred bins of around 1 keV width. In this work, we assume that the technology is going to evolve and that two dimensional PCDs with a lot of energy bins will be available in the future for medical CT. While the output of conventional integration mode detectors are single images, PCDs provide multi energy images and this additional spectral information opens up new perspectives such as improving the contrast-to-noise ratio (CNR) or reducing dose and artifacts. Moreover, it enables to quantify each material constituting the object independently, by decomposing the images into basis functions (e.g. bone and soft tissues). However, the latter application requires highly accurate images at each energy bin. In particular, scattered radiation impacts image quality as it induces bias, loss of contrast and artifacts, and has to be removed.

The objective of this PhD work is to develop a scatter correction method adapted to spectral CT imaging able to provide accurate images without increasing dose and acquisition time. This manuscript is organized as follows. In chapter 2, we present the basics of x-ray CT. First, we introduce some generalities about x-rays and their generation in a CT scanner. The main interactions between x-rays and matter, and the behaviors of the resulting primary and scattered radiation are then presented along with the conventional and photon counting detectors. Afterwards, we introduce the principle of CT reconstruction and identify the influence of scattered radiation. A review of scatter correction methods is then presented in chapter 3. Chapter 4 is dedicated to the presentation of the scatter correction that we developed which is based on the use of a semi-transparent primary modulator mask and adapted to spectral CT. First, the basic principle is reminded and we introduce the correction matrix, which compensates for the mask attenuation. Then, we present a scatter model based on B-splines and specific weightings according to the mask and the object structures. Finally, we present our cost function and detail the Newton's algorithm we used for its minimization. The method is tested on realistic images simulated with Gate in chapter 5. Then, using two imaging phantoms (RANDO and CIRS), we tested the method on experimental datasets in chapter 6. In chapter 7, we present a study on the correction of ring artifacts, which corrupted our experimental images. Finally, we conclude and discuss on perspectives in chapter 8.

2

Basics of computed tomography

2.1 Introduction

This first chapter aims at introducing the basics of computed tomography (CT) imaging. A tomographic acquisition consists in a set of radiographic acquisitions performed at several projection angles around the inspected object. After being generated (section 2.2), x-rays interact with the object while passing through it (section 2.3) and are then detected (section 2.4) to form the radiographs. The CT images are then generated with a reconstruction algorithm (section 2.5). Finally, the influence of scattered radiation on projection images and reconstructed CT slices is presented in section 2.6.

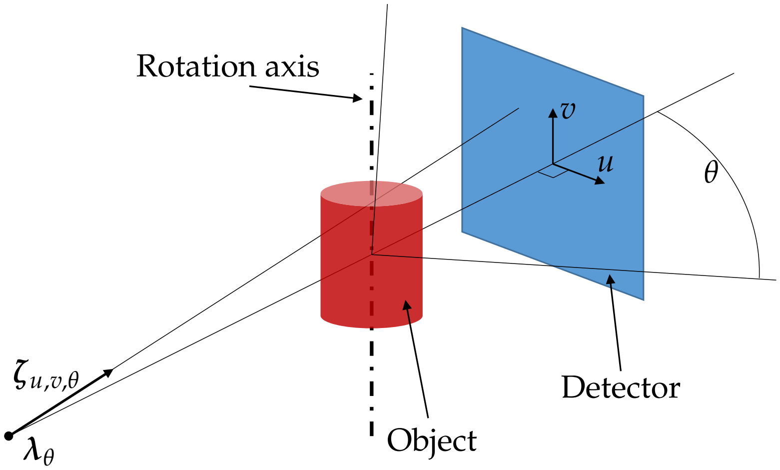

Figure 2.1 – Schematic of a tomographic system.

2.2 X-rays in medical imaging

X-rays were discovered in 1895 by the German physics professor Wilhelm Röntgen. As γ-rays, ultraviolet, visible light, infrared, microwaves or radiowaves, x-rays are a form of electromagnetic radiation (see figure 2.2).

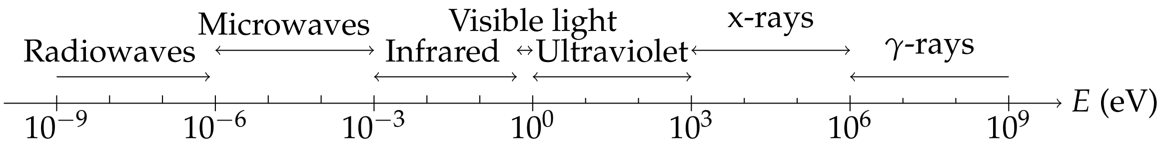

Figure 2.2 – Electromagnetic spectrum

The energy E of an x-ray photon is proportional to the frequency ν and inversely proportional to the wavelength λ of its associated radiation and can be described by the following expression:

$$E = h\nu = \frac{hc}{\lambda}, \tag{2.1}$$

where $h = 6.58 \times 10^{-16}$ eVs is Planck's constant and $c = 3 \times 10^{8}$ ms^{-1} the speed of light in vacuum [1]. The unit of eV represents the kinetic energy of a photon accelerated under 1 V and 1 eV $= 1.60 \times 10^{-19}$ J.

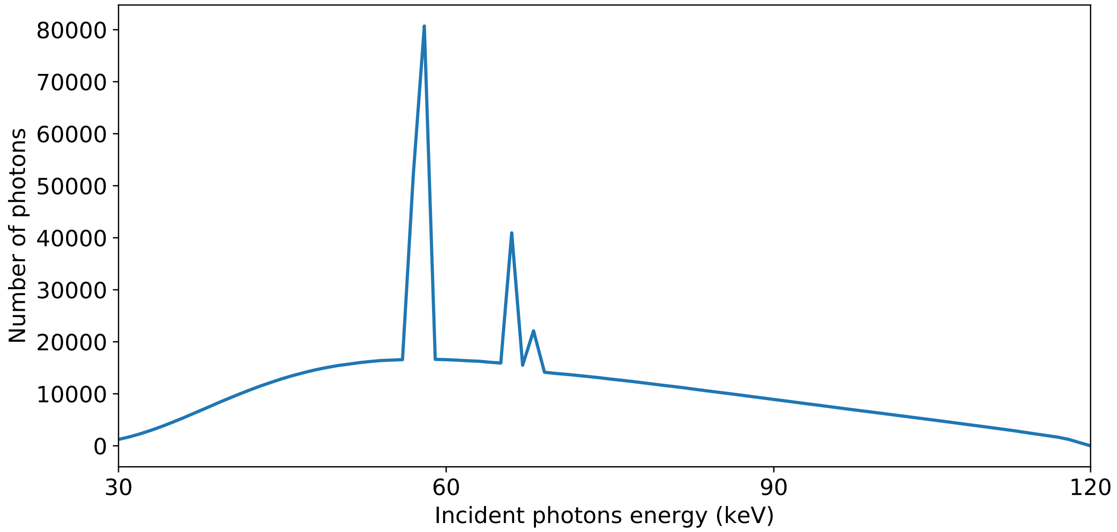

Figure 2.3 – Spectrum of a tungsten source with an acceleration voltage of 120 kV.

In medical CT, the x-rays are generated through a device called x-ray tube, in which electrons are accelerated by a high voltage and bombarded onto a target material, resulting in the conversion of a part of the electrons kinetic energy into x-ray photons. Figure 2.3 shows an example of a filtered source spectrum corresponding to an x-ray tube with a tungsten target supplied with 120 kV. For medical diagnosis applications, the energy of x-ray photons is generally comprised between a few tenths and 150 keV.

2.3 Primary and scattered radiation

When the x-ray beam passes through the object, it interacts by means of physical phenomena described in section 2.3.1. The resulting x-ray beam can be divided into primary and scattered radiations, which have their own characteristics, presented in section 2.3.2.

2.3.1 X-ray/matter interactions

In the energy-range of diagnostic medical imaging, there are three significant physical phenomena in which x-rays interact with matter: the photoelectric effect, Rayleigh scattering and Compton scattering. This section aims at presenting these three effects.

The photoelectric effect

The photoelectric effect is an interaction between a photon and an inner-shell electron of an atom, which binding energy is equal to or lower than the energy of the photon. The electron is ejected from its orbit with a kinetic energy equal to the difference between the energy of the incident photon and the binding energy of the electron and is called a photo-electron. The resulting vacancy may then be filled by an outer-shell electron, which involves the emission of a characteristic x-ray photon with an energy equal to the difference between the binding energies of the two shells. The process is described in figure 2.4. For biological tissues, the energy of the characteristic radiation is very low (less than 10 keV) and the corresponding x-ray photons cannot travel very far before being reabsorbed (less than the dimensions of a typical human cell).

The probability of a photoelectric event τ^{P} highly depends on the x-ray photon energy E and the atomic number Z of a given material. In the energy range of diagnostic medical imaging, this probability is inversely proportional to the cubic of the x-ray photon energy [1]:

$$\tau^{\mathrm{P}} \propto E^{-3}. \tag{2.2}$$

Furthermore, τ^{P} is proportional to the cubic of the atomic number Z [1]:

$$\tau^{\mathrm{P}} \propto Z^{3}. \tag{2.3}$$

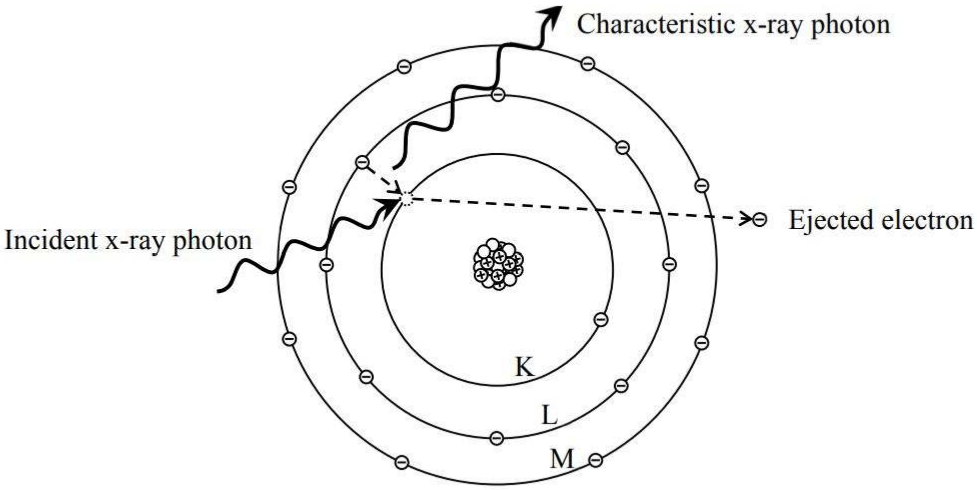

Figure 2.4 – Illustration of a photoelectric interaction (reproduced from [2]).

When a photoelectric event occurs, an electron is ejected from the atom which becomes an ion. This is called ionization which is a significant cause of cancer. This is the reason why the radiation dose deposited in a patient in medical imaging has to be controlled and maximally reduced.

Rayleigh scattering

The Rayleigh scattering is a process in which an x-ray photon changes direction without loosing energy. It is an interaction between a photon and the whole electron cloud of an atom. Each electron is set into momentary vibration by the oscillating electric field of the electromagnetic wave associated with the incident x-ray photon. As a result, the electrons emit a coherent radiation with the same wavelength as the incident x-ray photon and the combination of these radiations constitute the scattered radiation. This is the reason why Rayleigh scattering is also called coherent scattering. An illustration for Rayleigh scattering is presented in figure 2.5.

The angular Rayleigh scattering probability is described by the differential Rayleigh cross-section along with the molecular form factor. Figure 2.6 shows the differential Rayleigh cross-section with the molecular form factor of a water molecule at room-temperature for three incident photon energies. More information and other datasets can be found in [3]. One can observe that the scattering angle decreases when the photon energy increases.

The probability of a coherent scattering event σ^R is obtained by integrating the differential Rayleigh cross-section over all possible directions. The Rayleigh scattering occurs mainly with very low energy x-rays.

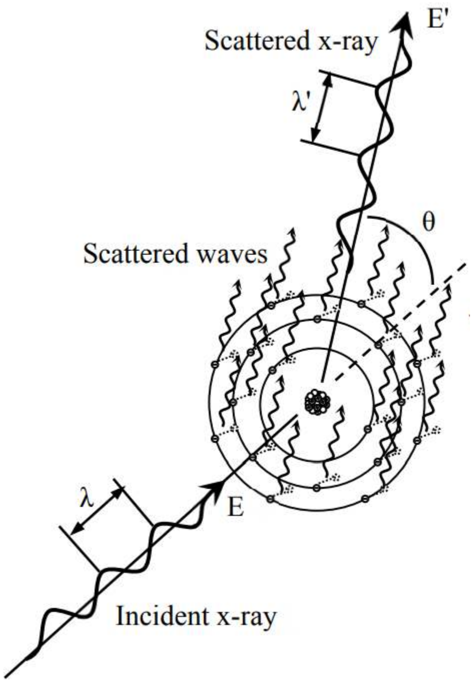

Figure 2.5 – Illustration of a Rayleigh interaction (reproduced from [2]).

As the coherent scattering does not lead to a loss of electron in the atoms, this phenomenon is non ionizing.

Compton scattering

The most significant interaction between x-rays and biological tissues in the energy range of medical diagnosis imaging is the Compton scattering effect. This phenomenon is an interaction between an x-ray photon and an individual electron of an atom and is therefore called incoherent scattering.

In the Compton scattering interaction, an x-ray photon strikes an electron, which binding energy is significantly lower than the photon's, resulting in a loss of energy and a change of direction of the photon and the ejection of the electron (called recoil electron). The incoherent scattering phenomenon is therefore ionizing. The phenomenon is illustrated in figure 2.7.

In the same way as Rayleigh scattering, the angular incoherent scattering probability is given by the differential Compton cross-section. The differential Compton cross-section of a water molecule at room temperature is shown in figure 2.8 for three different incident photon energies (dataset from [4]). The probability distribution appears to be smoother than in the Rayleigh case, and the probability for a photon

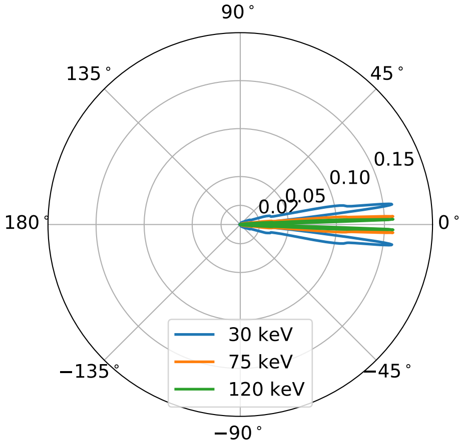

Figure 2.6 – Differential Rayleigh cross-section with molecular form factor of a water molecule at room temperature for three photon energies [3]

.

to be back-scattered is much higher and increases when the incident photon energy decreases. The probability of a Compton scattering event σ^{C} is then given, as for the Rayleigh scattering, by integrating the differential cross-section over all possible directions.

2.3.2 Primary and scattered radiation

Passing through an object, an x-ray beam undergoes the previously described interactions and is therefore attenuated. Photons which have not suffered any interaction with matter are called primary photons while the others are called scattered photons, as shown in figure 2.9. In addition, the primary map and the scatter map refer to the images formed by primary and scattered radiations respectively. This section presents the respective characteristics of primary and scattered radiations in x-ray imaging.

Primary radiation

The strength of attenuation of a material m at energy E is described by its mass attenuation coefficient denoted $\tau_m(E)$ (cm^2/g), which is the sum of the three significant interactions contributions:

$$\tau_m(E) = \tau_m^P(E) + \sigma_m^R(E) + \sigma_m^C(E). \tag{2.4}$$

The mass attenuation coefficient and its contributions for a water molecule at room temperature is presented in figure 2.10 for energies up to 150 keV. The mass attenuation tables can be found in, e.g., [5]. The photoelectric effect and the Rayleigh

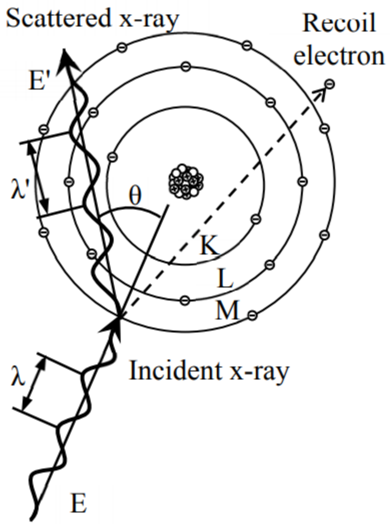

Figure 2.7 – Illustration of a Compton interaction (reproduced from [2]).

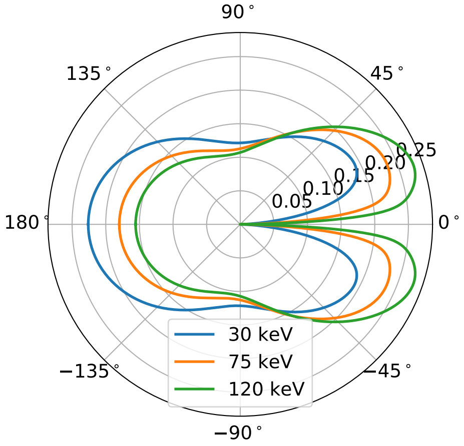

Figure 2.8 – Differential Compton cross-section with molecular form factor of a water molecule at room temperature for three photon energies [4]

.

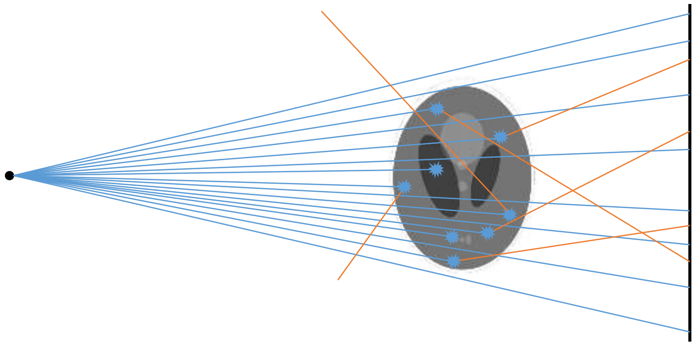

Figure 2.9 – Illustration of photons passing through an object (blue: primary photons, orange: scattered photons).

scattering are predominant at low energy, but from 60 keV, most of the attenuation comes from Compton interactions.

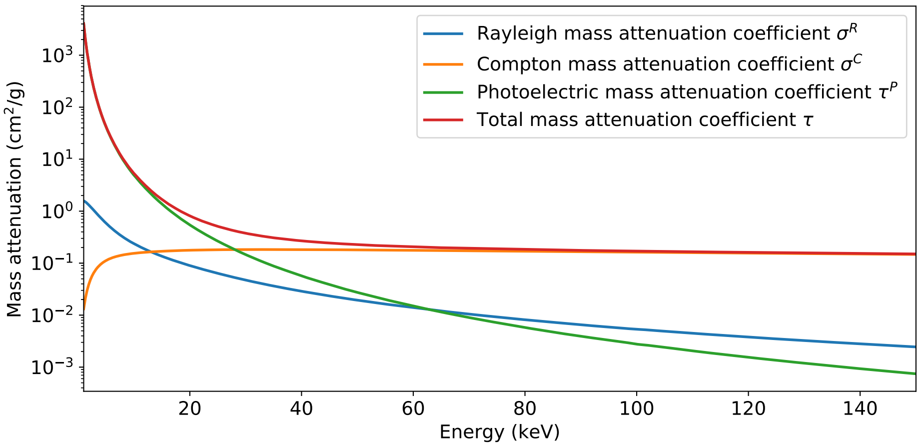

Figure 2.10 – Mass attenuation coefficient of a water molecule at room temperature for the three interactions.[5]

In addition, the linear attenuation coefficient $\mu_m(E)$ (cm^{-1}) is computed by multiplying $\tau_m(E)$ by the volumetric mass density ρ_m (g/cm^3) of material m:

$$\mu_m(E) = \rho_m \tau_m(E). \tag{2.5}$$

The linear attenuation coefficients at room temperature of three materials (water, adipose tissue and cortical bone) are shown in figure 2.11. The attenuation of cortical bone is larger, in particular at low energy, due to its larger mass density and the presence of high-Z materials (such as calcium).

An object may be represented by the discrete three-dimensional (3D) map of the volumetric mass densities $\boldsymbol{\rho}_m$ of its M materials, indexed with m. The corresponding

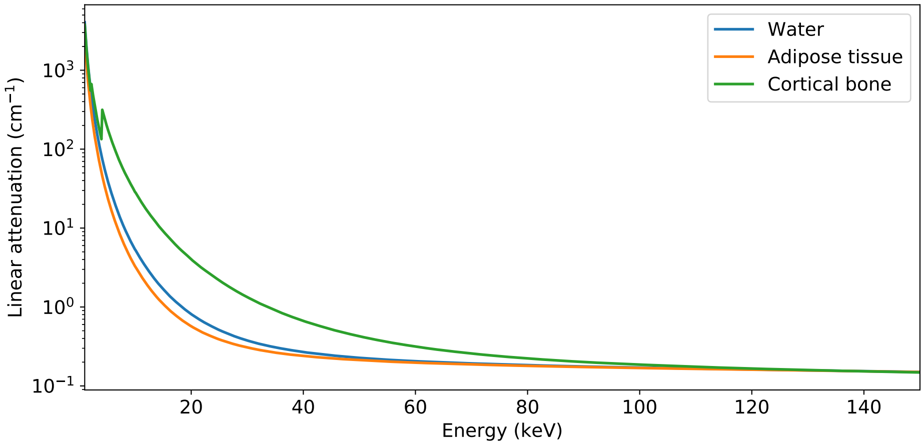

Figure 2.11 – Linear attenuation coefficients of three materials at room temperature.[5]

three-dimensional linear attenuation coefficient map is the sum of each material contribution:

$$\boldsymbol{\mu}(E) = \sum_{m=1}^{M} \boldsymbol{\rho}_m \tau_m(E). \tag{2.6}$$

The number of primary photons $N^{p,i}_{u,v,\theta}(E)$ with energy E incident on the detector at pixel position (u, v) and at projection angle θ is given by the Beer-Lambert law:

$$N^{p,i}_{u,v,\theta}(E) = N^{0,i}_{u,v}(E) \exp\left(-\int_{l\in\mathbb{R}} \mu(\boldsymbol{\lambda}_\theta + l\boldsymbol{\zeta}_{u,v,\theta}, E)\, \mathrm{d}l \right), \tag{2.7}$$

with $N^{0,i}_{u,v}(E)$ the number of photons of energy E emitted by the source towards pixel (u, v) as illustrated in figure 2.1. Note that the source spectrum does not vary with the projection angles.

Scattered radiation

Scattering effects are global phenomena and the scatter images in CT contain mostly low spatial frequencies in the two dimensions of the flat-panel detector and the angular dimension of the projections [6]. In addition, the smoothness and transmission factors of scatter maps depends on the energy of photons, the inspected object and the acquisition geometry.

The probability of scattering interactions presented in 2.3.1 are described by complex probabilistic models, and their expressions are not easily tractable by a simple formula as the Beer-Lambert law for primary radiation. In section 2.3.1, we have seen that the scattering probability for a photon increases with the atomic number, the density and the object thickness.

The acquisition geometry is also predominant in scatter maps behavior. The air-gap refers to the distance between the object and the detector and when it increases, scatter maps become smoother and scatter intensities decrease because the solid angle defined by the location of the interaction and the detector is smaller. In addition, the field of view (FOV) determines the quantity of matter in which first order scattering effects can occur and therefore small FOV (e.g pencil-beam or fan-beam) induce few scattered photons while greater FOV (e.g cone-beam) induce many more.

Considering the case of a typical medical CT system with around 50 cm between the isocenter and the detector, reasonable spatial and angular spacing between samples of the scatter map are 5 cm and 25° respectively [6]. We study the optimal sampling later in this document: in section 5.4 for realistic simulated images and in section 6.4 for experimental images.

Additionally, the differential cross sections of coherent and incoherent scattering according to the photons energy (figures 2.6 and 2.8 respectively) show that the scattering angle decreases when the photons energy increases and, as a consequence, the scatter maps are smoother for low energy photons than for more energetic ones. However, for significant air-gaps (from 30 cm), the shape of scattered radiation spectra are globally preserved along the spatial and angular positions [7].

2.4 Detection of x-rays

Digital x-ray detectors can be classified into two families: energy-integrating and photon-counting detectors. The technologies and their resulting measured data are introduced in 2.4.1 and 2.4.2.

2.4.1 Energy-integrating detectors

Energy-integrating detectors are the most common type of detectors used in medical CT, and correspond to two distinct technologies. First, indirect conversion detectors are composed of a scintillating material, which converts x-rays into visible light, and a set of photodiodes (one per pixel) converting light into electric signals. The second type are direct conversion detectors, in which the x-rays are directly converted to an electrical signal.

With energy-integrating detectors, the detected signal $I_{u,v,\theta}$ at pixel position (u, v)

and projection angle θ can be modelled by the following expression:

$$I_{u,v,\theta} = \int_E d_{u,v}(E)\ N^i_{u,v,\theta}(E)\ \mathrm{d}E, \tag{2.8}$$

where $d_{u,v}$ is the detector response function of pixel (u, v) (which does not depend on the projection angle) and $N^i_{u,v,\theta}(E)$ the number of photons of energy E reaching the detector at position (u, v).

2.4.2 Photon counting detectors

Photon counting detectors (PCD) based on semi-conductor materials (such as Si or CdTe) allow to count each incident photon independently. A PCD may have various energy bins in which the photons are classified according to their deposited energy depending on pre-defined energy thresholds. In this case, we call them energy-resolved photon counting detectors and we denote N_B the number of energy bins. The expected number $N_{b,u,v,\theta}$ of photons detected at pixel position (u, v), projection angle θ and energy bin b is described by:

$$N_{b,u,v,\theta} = \int_E d_{b,u,v}(E) N^i_{u,v,\theta}(E)\ \mathrm{d}E, \tag{2.9}$$

where $d_{b,u,v}$ is the detector response function of energy bin b of pixel (u, v).

By discretizing the energy spectrum in N_E samples, the number of detected photons becomes:

$$N_{b,u,v,\theta} = \sum_{e=1}^{N_E} d_{b,e,u,v} N^i_{e,u,v,\theta} = \boldsymbol{d}^T_{b,u,v} \boldsymbol{N}^i_{u,v,\theta}, \tag{2.10}$$

where $\boldsymbol{d}_{b,u,v} \in \mathbb{R}^{N_E}$ is the discretized response of energy bin b of pixel (u, v), T the transpose operator and $\boldsymbol{N}^i_{u,v,\theta} \in \mathbb{R}^{N_E}$ the vector representing the number of incident photons on the detector at each discretized energy. By concatenating the transposed responses of each energy bin, we obtain the detector response matrix (DRM) $\boldsymbol{D}_{u,v} \in \mathbb{R}^{N_B \times N_E}$ and the detected spectra $\boldsymbol{N}_{u,v,\theta} \in \mathbb{N}^{N_B}$ in pixel of coordinates (u, v) and projection θ, which values represent the number of photons detected in each energy bin, is:

$$\boldsymbol{N}_{u,v,\theta} = \boldsymbol{D}_{u,v} \boldsymbol{N}^i_{u,v,\theta}. \tag{2.11}$$

Most of the existing PCDs have a few energy bins (between 2 and 8 [8]), but some achieve an impressive number of a hundred bins of only 1 keV width [9]. However, the latters are line detectors designed for security applications. At this time, medical CT scanner with PCDs are only at a research stage and still have a few energy bins [10]. In this work, we assume that the technology is going to evolve and that two dimensional PCDs for medical imaging with a lot of energy bins will be available in the future. An example of a simulated detector response matrix is presented in figure

2.12 with 0.4 mm pitch pixels. This DRM mimics the one with 1 keV width bins [11], but is centered on the energy range from 30 to 120 keV, resulting in $N_B = 90$ energy bins. One can observe, on the right subfigure representing the detector response function of the 30th energy bin $\boldsymbol{d}_{30}$ (which corresponds to 70 keV), a large photoelectric peak at 70 keV and a smaller one near 95 keV. It indicates that most photons detected in energy bin 30 undergo a photoelectric effect with no fluorescent escape and have an energy around 70 keV, but a non-negligible part has an higher energy, due mostly to the x-ray fluorescence escape inside the detector. This is because the material of the detector is made of CdTe: the Kα_1 emission line of cadmium is at 23.2keV and Kα_1 emission line of tellurium is at 27.5keV, which is why one observes a line parallel to the photopeak at about 25 keV above the diagonal (it is quite visible in figure 2.12); we should also see a horizontal line at about 25keV if the fluorescence is being absorbed instead of escaping, but this is not visible in the figure due to the choice of energy range.

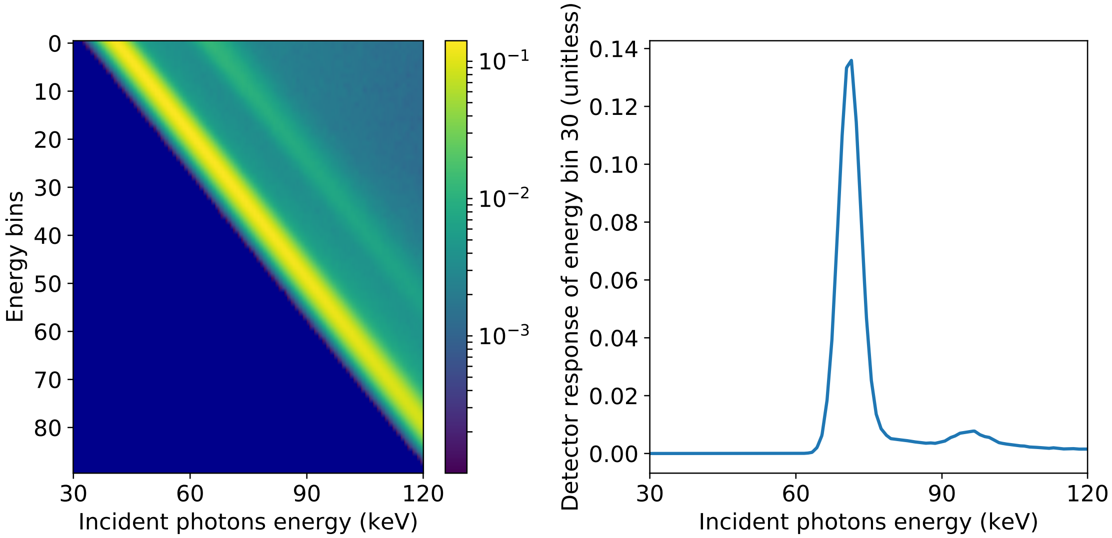

Figure 2.12 – Example of a DRM of a CdTe detector with $N_B = 90$ energy bins of 1 keV width. The first energy bin is centered on 30 keV, resulting in the quasi diagonal shape of the matrix.

When a detector is bombarded by a high flux x-ray beam, several photons may reach the detector at the same time and the detector recognizes only one photon which energy is greater than the detected ones. This problematical effect is known as pile-up and is a cause of artifacts but the simulated DRM does not model this phenomenon. In addition, when a photon strikes the detector at a given pixel, a part of the induced charge may be detected in neighbors pixels. This effect is called charge sharing and is taken into account in the simulation of the DRM.

In the rest of this manuscript, except if specified, energy-resolved photon counting detectors will be used and pile-up effects will be neglected.

2.5 X-ray computed tomography

2.5.1 The x-ray transform

The x-ray transform $\mathcal{R}\boldsymbol{\mu}$ associated with the three-dimensional function $\boldsymbol{\mu}$ is the set of integrals along lines going through the 3D source position $\boldsymbol{\lambda}_\theta$ in direction $\boldsymbol{\zeta}_{u,v,\theta}$ of pixel with coordinate (u, v) on the detector, as shown in figure 2.1.

Mathematically, the x-ray transform is defined as:

$$\mathcal{R}\boldsymbol{\mu}(u, v, \theta) = \int_{l \in \mathbb{R}} \boldsymbol{\mu}(\boldsymbol{\lambda}_\theta + l\boldsymbol{\zeta}_{u,v,\theta})\, \mathrm{d}l. \tag{2.12}$$

This transform performs a projection of the object onto the detector. This is the reason why the angle θ is called projection angle and the image acquired at a given projection angle projection image. In addition, the x-ray transform of a point object follows a sine curve in a v slice if the source follows a circular trajectory and the function $\mathcal{R}\boldsymbol{\mu}$ is also called the sinogram of $\boldsymbol{\mu}$. An example of attenuation projections and sinograms is shown in figure 2.13.

Some particular geometries can be isolated for CT scanners: parallel-beam for line-detectors (2D case) and very large source to detector distances (such that the x-rays are parallel), fan-beam for line-detectors and divergent x-rays, and cone-beam for planar-detectors (3D case) and divergent x-rays. In addition, parallel fan-beam refers to a stack of fan-beam acquisitions.

2.5.2 CT reconstruction

The tomographic reconstruction problem consists in estimating the linear attenuation coefficient map $\boldsymbol{\mu}$ from the sinogram $\mathcal{R}\boldsymbol{\mu}$. This problem has been well studied and mainly two classes of reconstruction methods can be isolated: analytical and discrete methods.

Analytical reconstruction

Analytical reconstruction methods model the images as continuous functions. They are based on the Fourier slice theorem, which links the 1D Fourier transform of the lines of sinogram of a parallel beam to the lines of the 2D Fourier transform of $\boldsymbol{\mu}$ represented in polar coordinates. In practice, the analytical reconstruction of a

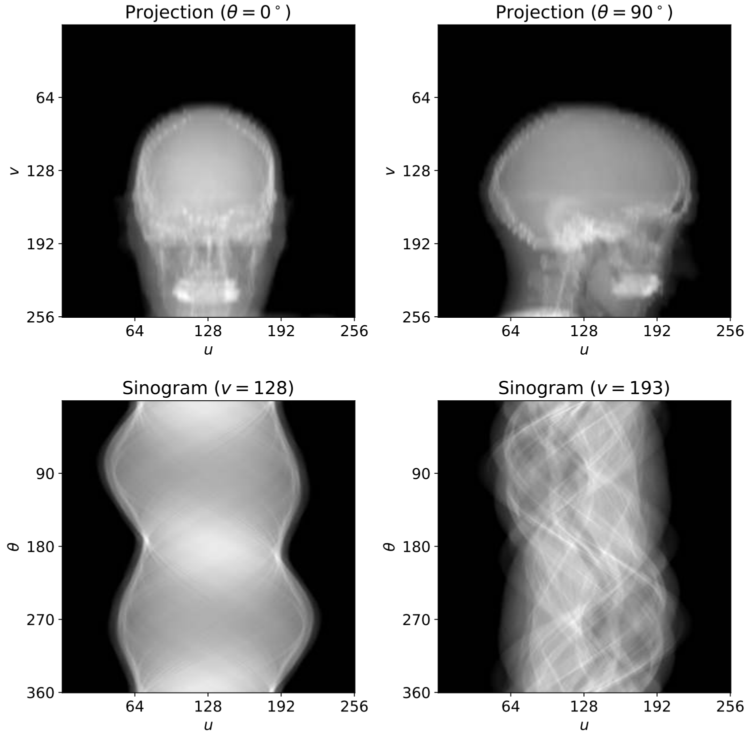

Figure 2.13 – Example of projections and sinograms

parallel sinogram, also called Filtered Back Projection (FBP), is performed by a two step process: filtering and backprojecting. The generalization of FBP to cone-beam CT is known as the FDK algorithm [12].

Analytical reconstruction methods are the reference algorithms in medical diagnosis CT thanks to their simplicity and rapidity. However, these algorithms are sensitive to the number of acquired projections and the statistical noise. In addition, an analytical formula does not exist for any system geometry, and if it does, a perfect knowledge of this geometry is required.

Discrete reconstruction

Unlike analytical methods, discrete reconstruction methods are based on a discrete representation of the images. These methods aim at inverting a discrete formulation of the forward acquisition model presented in equation 2.12. The class of discrete reconstruction methods are historically divided into two groups: algebraic and statistical methods.

The simplest form of algebraic reconstruction is the Algebraic Reconstruction Technique (ART). It is an iterative method which aims at inverting directly the direct problem without any prior information. This algorithm is very slow to converge because at one iteration, the update of a voxel is performed using a single ray. In contrast, the Simultaneous Algebraic Reconstruction Technique (SART) updates voxels using a complete projection of an angle θ. This leads to a speed up of the convergence. Other variations exists such as the Simultaneous Iterative Reconstruction Technique (SIRT), the Multiplicative Algebraic Reconstruction Technique (MART) or methods using ordered subsets. ART-based methods are known to be slower but more robust than analytical methods [13].

Statistical reconstruction methods reuse the idea of inverting the direct model, but taking into account the statistics of the detected photons. Poisson statistics are often used with PCDs because in photon counting x-ray imaging, the measures follow a Poisson distribution. The first reconstruction algorithm using a statistical model is the Maximum Likelihood Expectation-Maximization (ML-EM) in 1984 and many others have been proposed since. The modelling of the noise distribution gives to these methods a great advantage for reconstructing noisy sinograms.

Spectral reconstruction

In conventional CT, the reconstruction problem consists in estimating the attenuation map of the object. In a spectral reconstruction problem, the objective is to decompose the inspected object into some basis functions, for example bones and soft tissues. Various approaches have been proposed. The image-based approach performs a CT reconstruction at each energy bin, and estimate the decomposed object from the set of CT slices [14]. On the contrary, the projection-based one consists in decomposing the projections, and then reconstructing each decomposed sinogram [15]. Finally, joint approaches aim at reconstructing and decomposing at the same time [16]. The spectral reconstruction problem is still an active field of investigations.

In this work

The objective of this work is to provide accurate spectral CT images which can be used, for example, in a spectral reconstruction problem. However, the technique is not yet available for clinical applications, and no reference algorithm has emerged. Furthermore, they are generally quite hard to implement in practice. These are the reasons why we opted for the use of the FDK algorithm [FDK] for comparing CT slices.

2.5.3 In practice

In practice, we do not measure the exact sinogram $\mathcal{R}\boldsymbol{\mu}$, but a raw spectral total sinogram $\boldsymbol{N}^t \in \mathbb{R}^{N_B N_U N_V N_\Theta}$ (in number of photons detected) which is the sum of the primary and scatter contributions ($\boldsymbol{N}^p$ and $\boldsymbol{N}^s$ respectively):

$$\boldsymbol{N}^t = \boldsymbol{N}^p + \boldsymbol{N}^s. \tag{2.13}$$

We call total transmission spectral sinogram $\boldsymbol{t} \in \mathbb{R}^{N_B N_U N_V N_\Theta}$ the image which elements $t_{b,u,v,\theta}$ are the ratio between the number of detected photons in the presence of the object $\boldsymbol{N}^t$ and the one without any object $\boldsymbol{N}^0$:

$$t_{b,u,v} = \frac{N^t_{b,u,v}}{N^0_{b,u,v}}. \tag{2.14}$$

The primary and scatter transmission sinograms $\boldsymbol{p}$ and $\boldsymbol{s}$ are computed in the same way and $\boldsymbol{t} = \boldsymbol{p} + \boldsymbol{s}$.

We also introduce the total and primary attenuation sinograms $\boldsymbol{g}^t \in \mathbb{R}^{N_B N_U N_V N_\Theta}$ and $\boldsymbol{g}^p \in \mathbb{R}^{N_B N_U N_V N_\Theta}$ which are the negative logarithm of the transmission sinograms:

$$\boldsymbol{g}^t = -\ln(\boldsymbol{t}) \tag{2.15}$$

$$\boldsymbol{g}^p = -\ln(\boldsymbol{p}). \tag{2.16}$$

These attenuation sinograms are, at each energy bin, approximations of the x-ray transform defined in equation 2.12 and are the dataset used for the CT reconstruction.

When a polychromatic beam passes through an object, low energy photons are more attenuated than high energy ones, due to the decrease of the attenuation with the photons energy (see figure 2.11). As a result, the mean energy of the polychromatic spectrum increases. We call this phenomenon beam-hardening. Both total and primary attenuation sinograms suffer from beam-hardening, but since the latter is not corrupted by scattered radiation, the approximation of the x-ray transform is better.

The next section shows the influence of scattered radiation on both sinograms and reconstructed slices.

2.6 Influence of scattered radiation

We have shown in section 2.3 that scatter maps in CT are low frequency images. Because of the non-linearity of the logarithm function, the corresponding bias in attenuation sinograms is not smooth anymore and depends on the scatter to primary ratio ($\mathbf{SPR} = \frac{\boldsymbol{s}}{\boldsymbol{p}}$):

$$\begin{aligned} \boldsymbol{g}^t &= -\ln(\boldsymbol{p} + \boldsymbol{s}) && (2.17) \\ &= -\ln(\boldsymbol{p}(\frac{\boldsymbol{s}}{\boldsymbol{p}} + \mathbf{1})) && (2.18) \\ &= \boldsymbol{g}^p - \ln(\frac{\boldsymbol{s}}{\boldsymbol{p}} + 1) && (2.19) \\ &= \boldsymbol{g}^p - \ln(\mathbf{SPR} + \mathbf{1}) && (2.20) \\ &\approx \boldsymbol{g}^p - \mathbf{SPR} && (2.21) \end{aligned}$$

.

In the presence of scatter, the values of transmission images are larger than the ones without scatter and therefore the values of attenuation images and their variation range are lower. As a result, the scatter-corrupted attenuation images have a degraded contrast [17], as observed in figure 2.14.

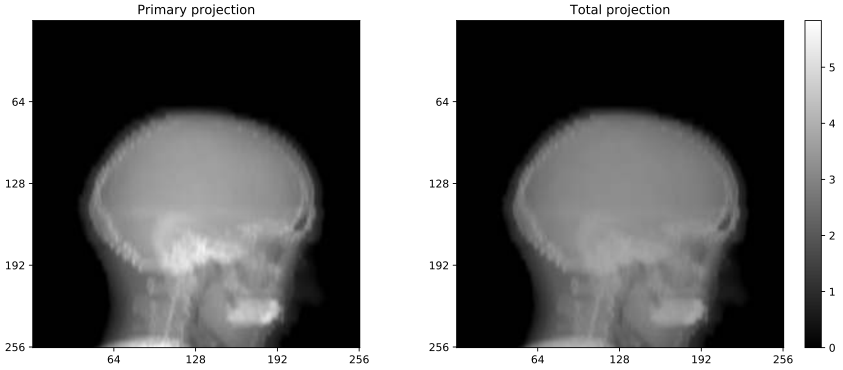

Figure 2.14 – Attenuation projection image without (left) and with (right) scatter.

Figure 2.15 shows profiles of the attenuation projection images, where the bias induced by scatter is greater for high attenuation values.

The influence of scattered radiation in reconstructed CT images is similar to the one in the projection domain: the attenuation values are lower than expected and the contrast is degraded, as shown in figure 2.16.

In addition, a well-known artifacts can appear: the cupping artifact, which is characterized by a cup-like profile instead of a constant for a homogeneous object. An example of such profile is presented in figure 2.17.

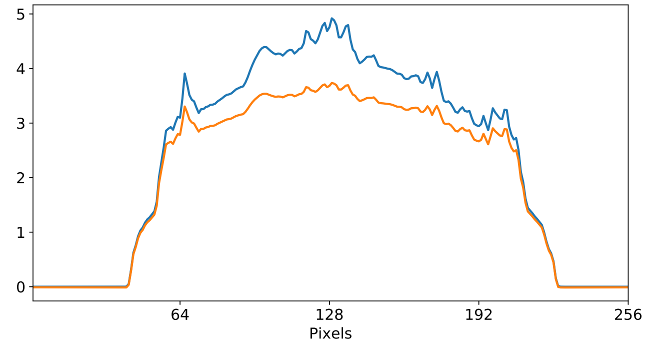

Figure 2.15 – Profiles of the projection presented in figure 2.14

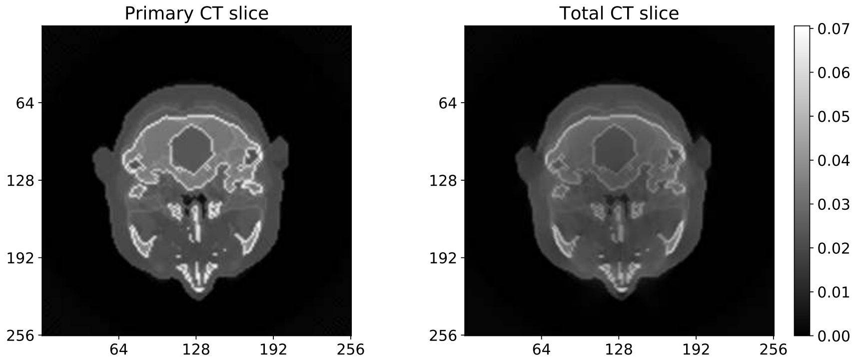

Figure 2.16 – CT slice without (left) and with (right) scatter

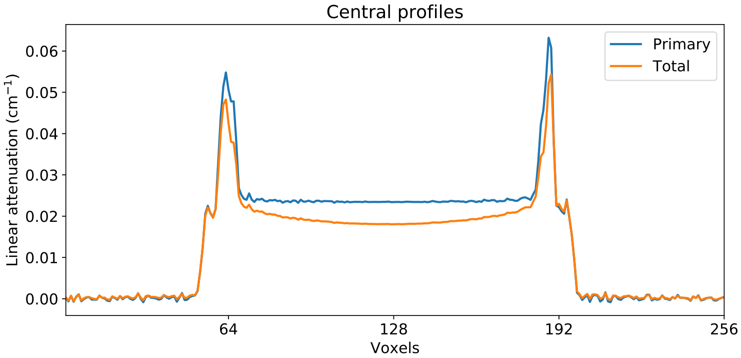

Figure 2.17 – Profiles of a CT slice without (blue) and with scatter (orange)

2.7 Conclusion

In this first chapter, we have presented the basics of CT imaging. After some generalities about x-rays in medical imaging, we presented the main interactions between x-rays and matter, along with the respective behaviors of primary and scattered radiation. Then, we presented the main detection technologies and the specificity of photon counting detectors. Finally, we presented the CT reconstruction strategies and highlighted the influence of scattered radiation on projection images and CT slices.

3

Scattered radiation correction: state of the art

3.1 Introduction

The problem of scattered radiation is known since the early history of x-ray imaging, and gave rise to numerous methods which we classified into two families: hardware-based and software-based methods. A review of scatter correction methods can be found in [18] and [19]. The hereunder chapter gives an up-to-date but non exhaustive personal review.

3.2 Hardware-based methods

The family of hardware-based scatter reduction methods consist in adapting the geometry or using additional devices to reduce the amount of scatter detected.

Anti-scatter grids The most common strategy to limit detected scatter consists in collimating the detector pixels by using anti-scatter grids. These devices absorb photons which trajectories does not follow the lines going from the source onto the pixels. Unfortunately, anti-scatter grids also absorb a part of the primary beam, and let pass a part of the scattered radiation, in particular photons scattered at a very small angle and photons which have been scattered several times and reach the detector following a primary photon like trajectory [20].

Air-gap increase Another technique for limiting the amount of scatter detected is to increase the air-gap between the object and the detector. With a greater air-gap, the scattered photons have fewer probability to reach the detector such as the solid angle covered by the detector is smaller, from the point of view of the object to be imaged [21] [22]. However, increasing the air-gap cannot reject all the scattered photons, and in most applications (e.g medical imaging), the CT scanner geometry cannot be adjusted and the air-gap is not sufficient for neglecting the scatter component.

Field of view collimation The level of scatter is directly related to the quantity of matter which is penetrated by the x-ray beam. Fan-beam geometries are therefore much less subject to scatter contamination than cone-beam ones. If a cone-beam acquisition is required, scatter can still be reduced by limiting the field of view to a given volume of interest [23]. This solution can lead to truncated data which can't be reconstructed with the original filtered back-projection technique [12] but alternatives already exist [24] [25]. The problem of reconstruction with limited field-of-view is still an open research topic.

3.3 Software-based methods

Unlike hardware-based, the group of software-based methods aims at removing totally the scatter component. They can again be divided into several sub-families. The first one we present in this section is the cupping artifact removal methods, which seek to correct the major artifact induced by scatter. In a second part, we present the emerging learning-based methods, based on machine learning strategies. The two last ones consist in estimating the scatter map and use it to recover the primary in a second step. While model-based methods use a physical model to recover the scatter map, measurement-based methods use an additional device with an appropriate algorithm.

3.3.1 Cupping artifact removal methods

A simple way to correct scattered radiation is to remove the cupping artifact it induces [26] [27] [28]. In [26], the cup-shape artifact is modeled as a circularly symmetric additive signal in the reconstructed CT slices. The disadvantage of the later is the low accuracy of the model. It is indeed easier to compensate for scattered radiation in the sinograms than in the CT slices, as noticed in [27], where the scatter model is defined in the projection domain as well as in [28]. In each case, the model is iteratively fitted as the one which gives the flattest object background in the reconstructed CT slices. The cupping evaluation being complex, in particular for non-smooth objects, these methods are not generally very accurate.

3.3.2 Learning-based methods

Recently, a class of scatter correction methods based on machine learning has emerged. [29] [30] [31] [32]. They require a training dataset of couples scatter-corrupted/scatter-free CT images in the same acquisition conditions and with similar objects, the scatter-free images being obtained with Monte-Carlo simulations [29] [32], a reference scatter correction method [30] or fan-beam acquisitions [31]. These techniques reveal a great potential in term of scatter removal accuracy within negligible computation time, but only in particular applications where the imaged object is known to be similar to the training dataset ones.

3.3.3 Model-based methods

Model-based methods refer to as scatter correction techniques in which scatter maps are estimated through a physical model of the acquisition. The most common strategies use scatter-kernels while others use more complex Monte-Carlo simulations.

Scatter kernel superposition

As explained before in section 2.3.2, scatter cannot be depicted by analytical expressions. The concept of scatter kernel superposition is to give a simplified deterministic relation between primary and scatter maps in the projection domain. Scatter kernels are basis functions which relate the primary signal at a pixel with the scatter distribution on the detector induced by the pencil-beam running from the source onto the pixel through convolution. The total scatter image is then computed as the contributions of all the pixels and the primary image is recovered by deconvolution.

The simplest solution is the use of stationary scatter kernels, where the same basis function is used for each pixel of the detector [33] [34]. The accuracy of the method may be improved by modeling the scatter kernel as the product of a shape term (similar to stationary scatter kernels) and a scatter intensity one based on empirical models [35] or an estimate of the object thickness [36]. Scatter kernels can be modeled using double Gaussian functions [36] and are determined through Monte Carlo simulations [36] or physical experiments [35].

[37] proposed to compute a set of primary CT slices estimates obtained with several scatter kernel parameters. The author assumes a linear combination of these estimates is the desired scatter-free CT slice and the optimal combination is estimated as the one which minimizes the total variation of the CT slice. It showed good results for metal-artifact reduction.

Recently, some authors proposed to improve the accuracy of scatter kernel superposition by using data consistency conditions (DCC). Data consistency conditions refers to as necessary conditions derived from the x-ray transform which have to be satisfied. In [38], the scatter kernels parameters are optimized on-line in order to satisfy the consistency condition. The approach presented in [39] consists in estimating a set of scatter maps obtained with different scatter kernel parameters, and the final scatter map is estimated as the linear combination of the different scatter images which satisfies the best the consistency condition (with the same assumption as [37]).

The concept of scatter kernel may also be incorporated directly in a discrete reconstruction method [40].

Scatter kernel superposition methods are known to provide good computation speeds, in particular for the simplest case of stationary scatter kernels. The dependency of these methods on the object and the acquisition geometry is a major drawback which can lead to incorrect scatter correction.

Monte-Carlo simulations

Monte-Carlo simulations are known to provide the most accurate scatter images because of its ability to simulate complex stochastic processes. Monte-Carlo based methods consist in modeling the imaged object in a preliminary reconstruction, estimating the scatter sinograms by using Monte-Carlo simulations and subtract it from the measured sinogram. The modeled object being reconstructed by scatter corrupted images, the estimated scatter may be biased and the later three steps process has to be iterated in order to minimize the error [41] [42]. Unfortunately, Monte-Carlo simulations are extremely time consuming. For example, a CT scan simulation took 430 h on a single core desktop PC in [43]. This computation time can be considerably lowered by using variance reduction techniques [42][44]: even with several iterations of the process, [42] achieved a 2 min computation time. Another solution proposed in [45] consists in simulating a very few number of photons, the scatter map being fitted from the sparse simulated scatter image. They were able to estimate the scatter map within 2 min, but with a single iteration of the process and a 16 cores computer [42]. As for scatter kernel based methods, Monte-Carlo simulations require a good knowledge of the object and the system geometry.

3.3.4 Measurement-based methods

Some scatter correction methods, measurement-based methods, use a physical device to modify the x-ray beam in a way which allow to deduce the scatter map from the measurements. The hereunder section present the beam-stop method along with its complementary, the beam-hole method. Two strategies using a primary modulator mask are then presented: Fourier filtering and spatial gradient minimization methods.

Beam-stop/beam-hole

The beam-stop methods use a fully-attenuating mask (typically made with lead) placed between the source and the object, such that no primary photon can reach the detector in pixels under the mask penumbra. Thus, the signal measured in those regions contains only scattered radiation and the whole scatter map can be estimated by interpolation.

This technique generally requires a second acquisition, without the beam-stop mask, in order to obtain a total acquisition from which one can subtract the estimated scatter map to recover the primary images [46][47][48]. It is worth noting that errors may be induced by a difference between the scatter maps of the two acquisitions. The additional acquisition induces an increase of dose and acquisition time which are undesirable issues in medical imaging. Various strategies have been proposed to limit the increase of dose and acquisition time in CT. A simple solution is to perform beam-stopped acquisitions on a limited number of projections and interpolate the scatter map between those [46][47]. Another way consists in placing the beam-blockers at the borders of the images and to simply interpolate the scatter map between those [49][50]. Another possibility is to use a moving beam-blocker array instead of a static one. The penumbra regions locations thus move from one projection to another and the pixels in those regions are interpolated in order to obtain the total acquisition [51] [52] [53][54] [55] [56][57]. A single acquisition can also be sufficient by using a half beam-blocker, which gives an estimation of the scatter map on only the half of the image, which is subtracted from the opposite projection image. The reconstruction is then performed using a modified version of the FDK algorithm [58]. These single scan beam-stop methods have the advantage to eliminate the problem of scatter map variations between two acquisitions.

The beam-hole method is very similar. In place of a mask made with discrete attenuating elements, the beam-hole mask is a slab drilled with discrete holes. The signal measured in these holes can be considered as scatter-free, and the scatter signal in these regions can be estimated by subtracting these scatter-free signals from the total images [59][60]. The advantages of beam-hole compared to beam-stop are a significant reduction of dose increase when two acquisitions are required and better performances in some cases [61].

Every method cited previously were developed for energy integrating detectors, but they can be applied on images acquired with photon counting detectors equally, each energy bin being treated independently. A dual acquisition method using a semi-transparent mask uses the spectral information to estimate the scatter map in a more complex procedure than the original beam-stop [62] and has shown similar results on experimental data [63]. It benefits from the mask transparency to limit the difference of scatter maps between the two acquisitions.

Fourier-based primary modulation

Another class of measurement-based methods use a semi-transparent mask with a uniform high-frequency pattern which is called primary modulator mask. Placed between the x-ray source and the object, the mask modulates the primary image such that its frequency spectrum is shifted in the high frequencies while the scatter component is not affected and still contains mostly low frequencies. An high-pass filter can then be applied on the acquired images, resulting in the scatter-free modulated primary images. Finally, the primary images are recovered by demodulation [64] [65] [66].

However, this technique is hard to implement in practice. It is indeed difficult to manufacture a mask with a perfectly uniform pattern, moreover when the pattern frequency is high. Furthermore, whatever the mask material, its attenuation varies according to the energy, inducing artifacts with the shape of the modulator pattern in the projections and ring artifacts in CT. This issue can be limited by the use of a material with a K-edge near the mean energy of the source spectrum [67] or by beam-hardening modeling [68].

Gradient-based primary modulation

This part focuses on a class of scatter correction methods based on primary modulation in which scatter maps are estimated by solving an optimization problem. These methods are presented in detail because they are the basis of the proposed scatter correction method which will be presented in chapter 4. The concept has been introduced in [69] and reused in [70] and [71] for integration-mode radiography. In CT, each projection is treated as an independent radiograph and the projection indices are therefore omitted in this section. We describe the basic principle, then various formulations of the optimization problem and minimization strategies are presented.

Principle The imaging system is illustrated in figure 3.1

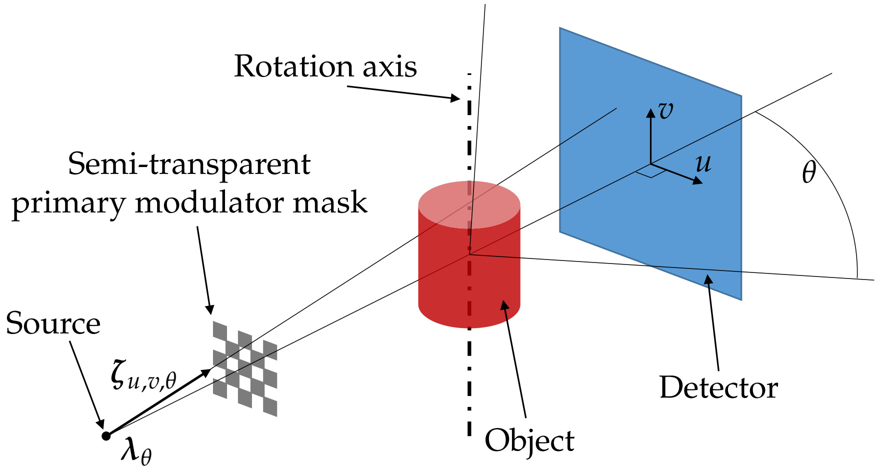

Figure 3.1 – X-ray imaging system with a primary modulator mask

In the presence of a primary modulator mask between the source and the object, the measured intensity signal $I^{\hat{t}}_{u,v}$ can be described by the following expression:

$$I^{\hat{t}}_{u,v} = I^{\hat{p}}_{u,v} + I^{s}_{u,v}, \tag{3.1}$$

where $I^{s}_{u,v}$ is the scatter signal (lower than the one expected without the presence of a mask) and $I^{\hat{p}}_{u,v}$ the modulated primary intensity depicted by:

$$I^{\hat{p}}_{u,v,\theta} = \int_E d_{u,v}(E) N^{0,i}_{u,v}(E) \exp\Big(- \int_{l\in\mathbb{R}} \mu(\boldsymbol{\lambda}_\theta + l\boldsymbol{\zeta}_{u,v,\theta}, E)\,\mathrm{d}l - \mu^m(E) l^m_{u,v}\Big)\,\mathrm{d}E, \tag{3.2}$$

with $\boldsymbol{\mu}^m$ being the energy-dependent LAC of material m constituting the primary modulator and $l^m_{u,v}$ the length of material m crossed by the ray going from the source onto pixel (u, v).

Aiming at an expression of the modulated primary $I^{\hat{p}}_{u,v}$ as a function of the unmodulated one $I^{p}_{u,v}$, beam-hardening is neglected and the following approximation is done:

$$I^{\hat{p}}_{u,v} \approx a^m_{u,v} I^p_{u,v}, \tag{3.3}$$

where $a^m_{u,v}$ is the transmission of the inserted modulator computed using the signal $I^{\hat{p}^0}_{u,v}$ (assumed to be scatter-free) measured in the presence of the mask but without any object:

$$a^m_{u,v} = \frac{I^{\hat{p}^0}_{u,v}}{I^0_{u,v}}. \tag{3.4}$$

Note that some rays do not intersect the mask since it has holes and $a^m_{u,v} = 1$ for those rays.

Using 3.3, one can derive the expression of the measured intensity image $\boldsymbol{I}^{\hat{t}} \in \mathbb{R}^{N_U N_V}$:

$$\boldsymbol{I}^{\hat{t}} = \mathrm{diag}(\boldsymbol{a}^m)\boldsymbol{I}^p + \boldsymbol{I}^s, \tag{3.5}$$

and then recover the unmodulated primary intensity from $\boldsymbol{I}^{\hat{t}}$ and $\boldsymbol{I}^s$ with the aid of the correction matrix $\boldsymbol{C} = \mathrm{diag}(\boldsymbol{a}^m)^{-1} \in \mathbb{R}^{N_U N_V \times N_U N_V}$:

$$\boldsymbol{I}^p = \mathrm{diag}(\boldsymbol{a}^m)^{-1}(\boldsymbol{I}^{\hat{t}} - \boldsymbol{I}^s) \tag{3.6}$$

$$= \boldsymbol{C}(\boldsymbol{I}^{\hat{t}} - \boldsymbol{I}^s). \tag{3.7}$$

The problem of compensating for the effect of the mask was solved in (3.7), assuming we knew the scatter intensity image $\boldsymbol{I}^s$ perfectly. We now consider an estimation of the scatter image $\tilde{\boldsymbol{I}}^s$ with an error $\boldsymbol{\varepsilon}$ given by $\boldsymbol{\varepsilon} = \boldsymbol{I}^s - \tilde{\boldsymbol{I}}^s$. By developing equation (3.7), we obtain the estimated primary intensity image $\tilde{\boldsymbol{I}}^p$:

$$\tilde{\boldsymbol{I}}^p = \boldsymbol{C}(\boldsymbol{I}^{\hat{t}} - \tilde{\boldsymbol{I}}^s) = \boldsymbol{C}(\boldsymbol{I}^{\hat{t}} - \boldsymbol{I}^s + \boldsymbol{\varepsilon}) = \boldsymbol{I}^p + \boldsymbol{C}\boldsymbol{\varepsilon}. \tag{3.8}$$

One can observe that an error $\boldsymbol{\varepsilon}$ on the estimated scatter image induces an error by $\boldsymbol{C}\boldsymbol{\varepsilon}$ on the estimated primary image. Assuming that both the scatter map and its estimate are smooth, the error $\boldsymbol{\varepsilon}$ is also smooth and therefore the error $\boldsymbol{C}\boldsymbol{\varepsilon}$ on the estimated primary map contains the same discontinuities as the correction matrix $\boldsymbol{C}$. In other words, the modulation pattern of the mask remains visible in the estimated primary image as long as $\boldsymbol{\varepsilon}$ is non-null. Considering a primary modulator with sharp edges, one can say that the presence of the modulation pattern increases the spatial gradient of the estimated primary. In addition, if the primary is locally smooth (i.e the object has weak structures), the scatter map may be estimated by minimizing the weighted gradient of the estimated primary:

$$\tilde{\boldsymbol{I}}^s \in \underset{\substack{\boldsymbol{I}^s \in \mathbb{R}^{N_U N_V} \\ \boldsymbol{I}^s \text{smooth}}}{\arg\min} \left\| \boldsymbol{W} \boldsymbol{\nabla} \boldsymbol{C} (\boldsymbol{I}^{\hat{t}} - \boldsymbol{I}^s) \right\|, \tag{3.9}$$

where $\| \bullet \|$ is a norm (typically ℓ^1 or ℓ^2), $\boldsymbol{W} \in \mathbb{R}^{2N_U N_V \times 2N_U N_V}$ is a diagonal weighting matrix and $\boldsymbol{\nabla} \in \mathbb{R}^{2N_U N_V \times N_U N_V}$ is the numerical spatial gradient of the image along the two dimensions u and v of the detector.

Formulations of the optimization problem and minimization strategies

Scatter model In order to simplify the optimization problem, [69] proposed to decompose images into N_K patches and to consider the scatter map as a piece-wise constant function with one single value of scatter of each one of the N_K patches. If we denote $\boldsymbol{x} \in \mathbb{R}^{N_K}$ the vector containing the scatter values of each patch and $\boldsymbol{B} \in \mathbb{R}^{N_U N_V \times N_K}$ an upsampling matrix, the scatter intensity image $\boldsymbol{I}^s$ can be described by:

$$\boldsymbol{I}^s = \boldsymbol{B}\boldsymbol{x}. \tag{3.10}$$

The idea of modeling scatter images as piece-wise constant functions was also used in [70] and [71].

Weights As explained previously, scatter can be estimated by minimizing the primary gradient, under the assumption that the object structures are locally smooth. If the assumption is correct, all the discontinuities present in the estimated primary come from the scatter estimation error and each component of the primary gradient can be treated as equal. This is the choice made in [69], where $\boldsymbol{W}$ is the identity matrix. However, in practice, the object structures cannot be neglected, in particular in the neighborhood of the edges of the object. [70] proposed to solve this issue by using the following weighting matrix:

$$\boldsymbol{W} = \operatorname{diag}\Big(\exp(-|\boldsymbol{\nabla} \tilde{\boldsymbol{I}}^p|) \Big), \tag{3.11}$$

where $\boldsymbol{\nabla} \tilde{\boldsymbol{I}}^p \in \mathbb{R}^{2N_U N_V}$ is an estimate of the primary gradient obtained by running the method a first time with an identity weighting matrix.

Problem formulation and optimization strategies In [69], the scatter values x_k are estimated independently for each patch by minimizing the ℓ_1 norm of the primary gradient:

$$\tilde{x}_k \in \underset{x_k \in \mathbb{R}}{\arg\min} \left\| \boldsymbol{\nabla} \boldsymbol{C}(\boldsymbol{I}^{\hat{t}} - \boldsymbol{B}\boldsymbol{x}) \right\|_1 . \tag{3.12}$$

This local-based formulation highly simplifies the minimization strategy as it is a simple mono-variable optimization problem. They chose to solve it by means of a line-search algorithm (golden cut section search). The scatter values are then assigned to the center pixels of the patches and the scatter image is filled by linear interpolation. The final scatter image is generated by applying a low-pass filter to the interpolated one.

Unlike the latter, [70] proposed a global formulation of the problem, where the scatter values are estimated all together by solving the following least square problem:

$$\tilde{\boldsymbol{x}} \in \underset{\boldsymbol{x} \in \mathbb{R}^{N_K}}{\arg\min} \left\| \boldsymbol{W} \boldsymbol{\nabla} \boldsymbol{C}(\boldsymbol{I}^{\hat{t}} - \boldsymbol{B}\boldsymbol{x}) \right\|_2^2 + \gamma \| \boldsymbol{\nabla} \boldsymbol{B}\boldsymbol{x} \|_2^2. \tag{3.13}$$

The second term in 3.13 commands a low variation of the scatter values in neighbor patches. Note that the differential operator in [70] is not exactly the gradient operator. The use of the ℓ_2 norm simplifies the minimization compared to the ℓ_1 one because of its differentiability and allows the use of methods such as conjugate gradient or Gauss-Seidel. In the study, the latter is used.

3.4 Conclusion and motivation of the thesis

We have shown in this chapter that numerous scatter correction techniques are available in the literature for x-ray CT. Hardware-based methods does not require any processing, but no strategy is able to reject totally the scatter component. As the quantification of the scatter induced cupping artifact is a complex problem, methods based on this artifact assessment are not very accurate. Strategies based on machine learning highly depend on the object and the geometry and require learning data sets based on images very similar to the ones to be processed. Scatter-kernel superposition methods are generally fast but also suffer from object and geometry dependency, even though solutions have been proposed to tackle this issue. Scatter correction through Monte-Carlo simulations have demonstrated a very good accuracy but the huge computation time is a major drawback. Beam-stop methods provide good results but with a substantial dose and acquisition time increase (two acquisitions) or with a truncation of data (single acquisition). Fourier-based primary modulation is not relevant due to the difficulty to manufacture a perfectly uniform mask and to beam-hardening. Finally, even if the latter issue remains problematic, gradient-based primary modulation methods are very promising due to their theoretically low object dependency. The global minimization of the cost function is much less time consuming than the local one if it is easy to minimize, like the one based on the ℓ^2 norm. However, the ℓ^1 norm cost function is less sensitive to the object structures and gives better results.

The context of this thesis is spectral CT, using photon counting detectors. Most of the previously described methods were developed for conventional CT, with energy-integrating detectors. If the majority of them can be applied separately in each energy bin of a spectral CT acquisition, the additional spectral information may also improve the performances of some of them. In particular, it may open possibilities for limiting the beam-hardening induced by the primary modulator mask in gradient-based methods, which is the major drawback of these strategies. Additionally, we aim at benefiting from both the low object dependency of the ℓ^1 norm and the minimization easiness of the ℓ^2 one. Finally, we would like a smooth three dimensional scatter model allowing to apply the cost function directly on the final scatter map without the need of a posterior smoothing step, and able to treat the projection images all together in order to benefit from the redundancy of the information between adjacent projections.

In the next chapter, a gradient-based method using a primary modulator mask and adapted to multi-energy imaging, which is the product of this PhD work, is presented.

4

Scatter correction for spectral CT using a primary modulator mask

4.1 Introduction

We have presented a review of scatter correction methods in chapter 3, and highlighted the family of gradient-based primary modulation methods. This chapter reminds the principle of the latter family of methods while introducing our notations in section 4.2 and then presents the main methodological contributions of this PhD thesis: a scatter correction method adapted to spectral CT using a primary modulator mask. First, we introduce in section 4.3 the correction matrix which compensates for the mask attenuation by using the spectral information. A three dimensional scatter model based on B-splines is then introduced in section 4.4, which reduces the dimensionality of the scatter estimation problem. In section 4.5, specific weighting matrices are introduced to relax the assumption of locally smooth primary maps (see section 3.3.4). The complete cost function with a regularization term is then introduced in section 4.6 along with the optimization strategy we opted for in section 4.8.

4.2 Gradient-based primary modulation with a photon counting detector

The objective of this section is to remind the basic principle of a gradient-based primary modulation scatter correction method (presented in section 3.3.4), and to introduce the notations we used in the rest of this document.

The imaging system is the one presented in figure 3.1. We denote $\hat{\boldsymbol{p}} \in \mathbb{R}^{N_B N_U N_V N_\Theta}$ the modulated primary transmission spectral sinogram in the presence of a primary modulator mask between the source and the object and we assume that there exists a matrix $\boldsymbol{C} \in \mathbb{R}^{N_B N_U N_V N_\Theta \times N_B N_U N_V N_\Theta}$ which compensates for the mask attenuation. The unmodulated primary image $\boldsymbol{p} \in \mathbb{R}^{N_B N_U N_V N_\Theta}$ can then be retrieved with the following expression:

$$\boldsymbol{p} = \boldsymbol{C}\hat{\boldsymbol{p}}. \tag{4.1}$$

In the presence of scattered radiation, we measure the modulated total image $\hat{\boldsymbol{t}} \in \mathbb{R}^{N_B N_U N_V N_\Theta}$ which can be depicted as the sum of the modulated primary and the scatter component $\boldsymbol{s} \in \mathbb{R}^{N_B N_U N_V N_\Theta}$:

$$\hat{\boldsymbol{t}} = \hat{\boldsymbol{p}} + \boldsymbol{s}. \tag{4.2}$$

Note that, in this case, the measured scatter is expected to be lower than the one we would have measured without any modulator mask, due to its attenuation.

Given an estimate of the scatter map $\tilde{\boldsymbol{s}}$ and by combining equations 4.1 and 4.2, an estimate of the primary image $\tilde{\boldsymbol{p}}$ can be obtained with the following expression:

$$\tilde{\boldsymbol{p}} = \boldsymbol{C}(\hat{\boldsymbol{t}} - \tilde{\boldsymbol{s}}). \tag{4.3}$$

As explained in section 3.3.4, the modulation pattern remains visible into the estimated primary as long as the estimated scatter $\tilde{\boldsymbol{s}}$ is wrong. If the modulator mask has sharp edges, and assuming the scatter map is smooth and the primary image is locally smooth, the scatter image is the one which minimizes the weighted gradient of the estimated primary:

$$\tilde{\boldsymbol{s}} \in \underset{\substack{\boldsymbol{s} \in \mathbb{R}^{N_B N_U N_V N_\Theta} \\ s \text{ smooth}}}{\arg\min} \|\boldsymbol{W}\boldsymbol{\nabla}\boldsymbol{C}(\hat{\boldsymbol{t}} - \boldsymbol{s})\|, \tag{4.4}$$

where $\| \bullet \|$ is a norm (ℓ^1 would be optimal), $\boldsymbol{W} \in \mathbb{R}^{2N_B N_U N_V N_\Theta \times 2N_B N_U N_V N_\Theta}$ a diagonal weighting matrix and $\boldsymbol{\nabla} \in \mathbb{R}^{2N_B N_U N_V N_\Theta \times N_B N_U N_V N_\Theta}$ the numerical spatial gradient of the image along the two dimensions u and v of the detector.

In the next section, we present the correction matrix $\boldsymbol{C}$, which compensates for the mask attenuation by taking into account the spectral information provided by the photon counting detector.

4.3 Compensation for the mask attenuation

4.3.1 Theory

According to chapter 2, the primary transmission factor at pixel position (u, v) and energy bin b without the presence of a primary modulator mask is:

$$p_{b,u,v} = \frac{N^p_{b,u,v}}{N^0_{b,u,v}} \tag{4.5}$$

$$= \frac{\boldsymbol{d}^T_{b,u,v}\boldsymbol{N}^{p,i}_{u,v}}{\boldsymbol{d}^T_{b,u,v}\boldsymbol{N}^{0,i}_{u,v}}, \tag{4.6}$$

where $N^p_{b,u,v}$ and $N^0_{b,u,v}$ are the numbers of detected primary photons with and without an object respectively, $\boldsymbol{d}_{b,u,v} \in \mathbb{R}^{N_E}$ is the discretized response of the energy bin b of the detector and $\boldsymbol{N}^{p,i}_{u,v}$ the discretized spectrum of primary radiation incident on the detector at pixel position (u, v) (in number of photons). According to equation 2.7, the element of this spectrum at discretized energy e can be modeled as:

$$N^{p,i}_{e,u,v} = N^{0,i}_{e,u,v} \exp\left(- \int_{l \in \mathbb{R}} \boldsymbol{\mu}_e(\boldsymbol{\lambda}_\theta + l\boldsymbol{\zeta}_{u,v,\theta})dl \right). \tag{4.7}$$

In the presence of a primary modulator mask, the latter becomes:

$$N^{\hat{p},i}_{e,u,v} = N^{0,i}_{e,u,v} \exp\left(- \int_{l \in \mathbb{R}} \boldsymbol{\mu}_e(\boldsymbol{\lambda}_\theta + l\boldsymbol{\zeta}_{u,v,\theta})dl - \mu^m_e l^m_{u,v} \right), \tag{4.8}$$

where $\boldsymbol{\mu}^m \in \mathbb{R}^{N_E}$ and $l^m_{u,v} \in \mathbb{R}$ are the linear attenuation of material m constituting the primary modulator mask and the length of material m crossed by the ray going from the source onto pixel (u, v), respectively.

The primary transmission factor $\boldsymbol{p} \in \mathbb{R}^{N_B N_U N_V}$ can then be expressed in a vectorial form:

$$\boldsymbol{p}_{u,v} = \text{diag}(\boldsymbol{N}^0_{u,v})^{-1}\boldsymbol{N}^p_{u,v} \tag{4.9}$$

$$= \text{diag}(\boldsymbol{N}^0_{u,v})^{-1}\boldsymbol{D}_{u,v}\left(\boldsymbol{N}^{0,i}_{u,v} \odot \exp\Big(- \int_{l \in \mathbb{R}} \boldsymbol{\mu}(\boldsymbol{\lambda}_\theta + l\boldsymbol{\zeta}_{u,v,\theta})dl \Big) \right), \tag{4.10}$$

$\odot$ representing the Hadamard product and $\boldsymbol{D}_{u,v}$ the detector response matrix of pixel (u, v). In the same way, the vectorial expression of the modulated transmission factor

$\hat{\boldsymbol{p}} \in \mathbb{R}^{N_B N_U N_V}$ is:

$$\hat{\boldsymbol{p}}_{u,v} = \mathrm{diag}(\boldsymbol{N}^0_{u,v})^{-1}\boldsymbol{D}_{u,v}\left(\boldsymbol{N}^{0,i}_{u,v} \odot \exp\Big(-\int_{l\in\mathbb{R}} \boldsymbol{\mu}(\boldsymbol{\lambda}_\theta + l\boldsymbol{\zeta}_{u,v,\theta})dl - \boldsymbol{\mu}^m l^m_{u,v}\Big)\right) \tag{4.11}$$

$$= \mathrm{diag}(\boldsymbol{N}^0_{u,v})^{-1}\boldsymbol{D}_{u,v}\mathrm{diag}\Big(\exp(-\boldsymbol{\mu}^m l^m_{u,v})\Big)\left(\boldsymbol{N}^{0,i}_{u,v} \odot \exp\Big(-\int_{l\in\mathbb{R}} \boldsymbol{\mu}(\boldsymbol{\lambda}_\theta + l\boldsymbol{\zeta}_{u,v,\theta})dl\Big)\right). \tag{4.12}$$

From equations 4.10 and 4.12, and assuming that the DRM is square ($N_B = N_E$) and invertible, one can retrieve the unmodulated primary $\boldsymbol{p}_{u,v}$ from the modulated one $\hat{\boldsymbol{p}}_{u,v}$:

$$\boldsymbol{p}_{u,v} = \mathrm{diag}(\boldsymbol{N}^0_{u,v})^{-1}\boldsymbol{D}_{u,v}\mathrm{diag}\Big(\exp(\boldsymbol{\mu}^m l^m_{u,v})\Big)\boldsymbol{D}^{-1}_{u,v}\mathrm{diag}(\boldsymbol{N}^0_{u,v})\hat{\boldsymbol{p}}_{u,v} \tag{4.13}$$

$$= \boldsymbol{C}_{u,v}\hat{\boldsymbol{p}}_{u,v}, \tag{4.14}$$

$\boldsymbol{C}_{u,v}$ being the correction matrix associated with pixel (u, v) which is depicted by the following expression:

$$\boldsymbol{C}_{u,v} = \mathrm{diag}(\boldsymbol{N}^0_{u,v})^{-1}\boldsymbol{D}_{u,v}\mathrm{diag}\Big(\exp(\boldsymbol{\mu}^m l^m_{u,v})\Big)\boldsymbol{D}^{-1}_{u,v}\mathrm{diag}(\boldsymbol{N}^0_{u,v}). \tag{4.15}$$

This matrix can be seen as a change of basis from the physical attenuation of the mask to the measure domain.

In order to analyse the shape of this correction matrix, we reuse the simulated detector response matrix presented in section 2.4 and we bin its lines, as shown in figure 4.1, where the left part represents the original version of a detector response matrix with $N_B = 8$ energy bins and $N_E >> N_B$, and the right one its re-binned version with $N_E = B_B = 8$ which is non singular.

Using the square version of the DRM, it is possible to compute a correction matrix with its analytical expression 4.15. An analytical correction matrix corresponding to a pixel attenuated by 5 mm of a graphite primary modulator mask is presented in figure 4.2 along with the profiles of its three first rows.

Unfortunately, the pixel dependent detector response matrices of a real detector are not known in practice which prevents the use of this analytical solution. In order to overcome this difficulty, we propose a model for the lines of the correction matrix. The next section presents this solution.

4.3.2 Model-based estimation

By observing analytical correction matrices computed according to 4.15, we reuse the following parametric model (introduced in [72] and inspired by [62]) for the rows

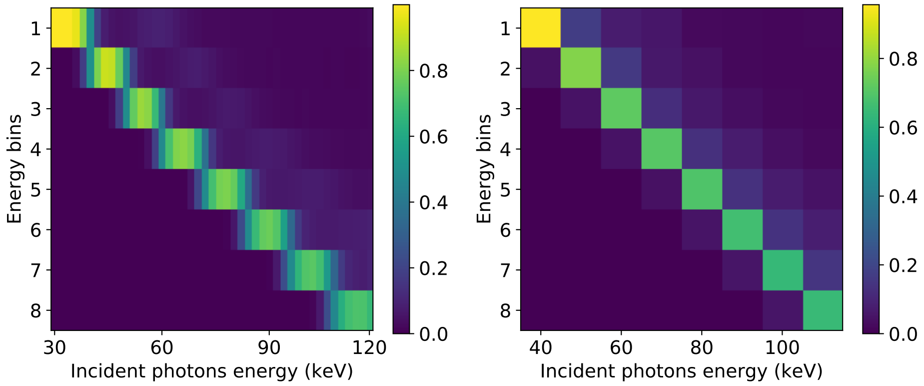

Figure 4.1 – Detector response matrix with $N_B = 8$ (left) and its rebinned version with $N_E = N_B$ (right)

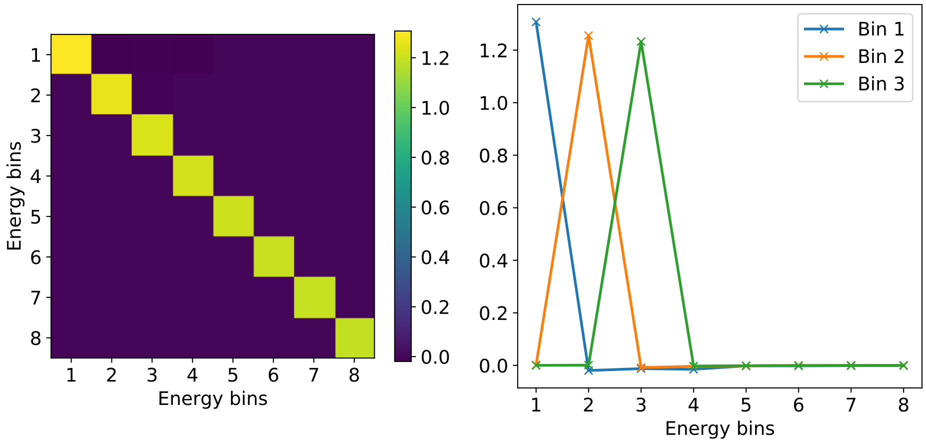

Figure 4.2 – Analytical correction matrix of a pixel attenuated by the primary modulator mask (left) and some of its horizontal profiles (right)

of the correction matrices:

$$c_{b,u,v}(b') = h(b'-b)\left(c^0_{b,u,v}\delta(b'-b) + c^1_{b,u,v}\exp(-c^2_{b,u,v}(b'-b))\right), \tag{4.16}$$

with $\boldsymbol{c}_{b,u,v} \in \mathbb{R}^{N_B}$ the row of $\boldsymbol{C}_{u,v}$ corresponding to energy bin b, $[c^0_{b,u,v}, c^1_{b,u,v}, c^2_{b,u,v}]$ a triplet of scalar parameters and h and δ the Heaviside and Dirac functions.

The model parameters for each pixel and energy bin may be estimated through an off-line calibration procedure using a scatter-free dataset of N^{cal} pairs of spectral transmission images with various attenuation levels: with and without primary modulator mask ($\hat{\boldsymbol{p}}_k$ and $\boldsymbol{p}_k$ respectively):

$$[\tilde{c}^0_{b,u,v}, \tilde{c}^1_{b,u,v}, \tilde{c}^2_{b,u,v}] \in \underset{[c^0_{b,u,v}, c^1_{b,u,v}, c^2_{b,u,v}] \in \mathbb{R}^3}{\arg\min} \sum_{k=1}^{N^{\text{cal}}} (p_{k,b,u,v} - \boldsymbol{c}^T_{b,u,v} \hat{\boldsymbol{p}}_{k,u,v})^2. \tag{4.17}$$

In our work, the minimization was performed with the Nelder-Mead's downhill simplex algorithm [73].

4.4 Scatter model

We have seen in 2.3.2 that scatter maps in CT are smooth in the two spatial directions of the flat-panel detector and in the angular direction of the projections. As well as in [69] and [70], we seek for a scatter model able to provide a representation of scatter with just a few parameters (in order to lower the dimensionality of the problem), the difference being that we want a better accuracy than a piece-wise constant function.

In this work, we opted for a scatter model using three dimensional cubic B-spline basis functions, which are commonly used for modelling smooth maps [74], and we recover the scatter map knowing the N_K parameters $x_{b,k}$ for each energy bin with the following expression:

$$s_{b,u,v,\theta} = \sum_{k=1}^{N_K} \beta_k(u, v, \theta) x_{b,k}, \tag{4.18}$$

with $\beta_k(u, v, \theta)$ the k-th B-spline basis function evaluated at pixel (u, v) and projection θ.

The definition of the B-spline basis function is

$$\beta_k(u, v, \theta) = \beta^2 \left(\frac{u - u_k}{\delta_u} \right) \beta^2 \left(\frac{v - v_k}{\delta_v} \right) \beta^2 \left(\frac{\theta - \theta_k}{\delta_\theta} \right), \tag{4.19}$$

where (u_k, v_k, θ_k) and $(\delta_u, \delta_v, \delta_\theta)$ are the B-splines knots positions and spacings respectively, and $\beta^2(x)$ the cubic B-spline basis function

As one can see on figure 4.3, representing the B-spline bases of order 0 to 4, the B-spline bases of order higher than one are defined from the 0-th order one:

$$\beta^n = \beta^0 * \beta^{n-1} \tag{4.20}$$

In particular, the cubic B-spline basis function $\beta^2(x)$ centered on zero is given by

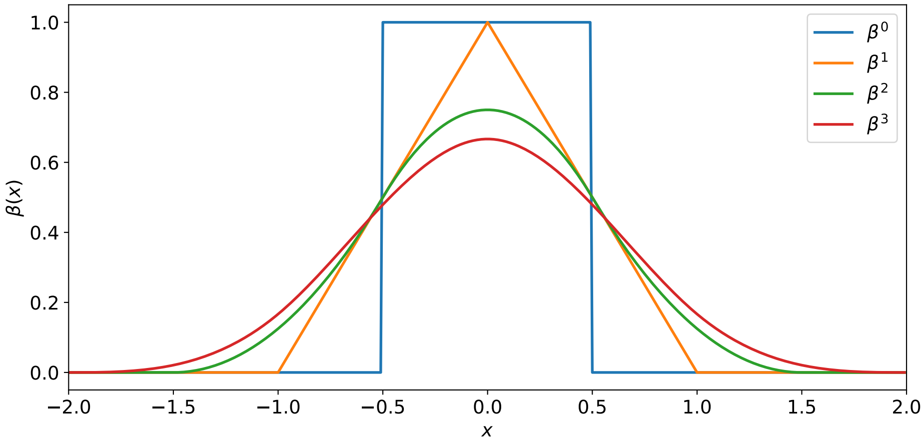

Figure 4.3 – B-spline basis functions of order 0, 1, 2 and 3

the following expression:

$$\beta^2(x) = (\beta^0 * \beta^0 * \beta^0)(x) = \begin{cases} \frac{1}{2}(x^2 + 3x + \frac{9}{4}), & \forall x \in [-\frac{3}{2}, -\frac{1}{2}[, \\ \frac{3}{4} - x^2, & \forall x \in [-\frac{1}{2}, \frac{1}{2}[, \\ \frac{1}{2}(x^2 - 3x + \frac{9}{4}), & \forall x \in [\frac{1}{2}, \frac{3}{2}[, \\ 0, & \forall x \in]-\infty, -\frac{3}{2}[\cup [\frac{3}{2}, +\infty[. \end{cases} \tag{4.21}$$

From order 2, the basis function associated with a given knot is non-null at an adjacent knot position. This implies the necessity to define B-spline knots outside the image. This situation is illustrated on figure 4.4, where the red dots represent the B-spline knots. However, this illustration is not correct in the angular dimension. Indeed, the continuity of the data between the first and the last projection requires also a continuity of the estimated scatter map and the angular knots are therefore placed in a circle.

The number of parameters N_K required to represent the scatter map in one energy bin corresponds to the number of B-spline knots chosen, and depends on the spacing between two knots in each of the three dimensions. The choice of the optimal spacing in each direction is discussed in section 5.4. In our study, the number of parameters N_K will be varied between 126 and 600.

We denote $\boldsymbol{B} \in \mathbb{R}^{N_B N_U N_V N_\Theta \times N_B N_K}$ the matrix containing the B-spline basis functions and $\boldsymbol{x}$ the vector of the model parameters $x_{b,k}$. The scatter map is then obtained from $\boldsymbol{x}$ with:

$$\boldsymbol{s} = \boldsymbol{B}\boldsymbol{x}. \tag{4.22}$$

One can notice that the particular case of 0-th order B-spline basis functions provide

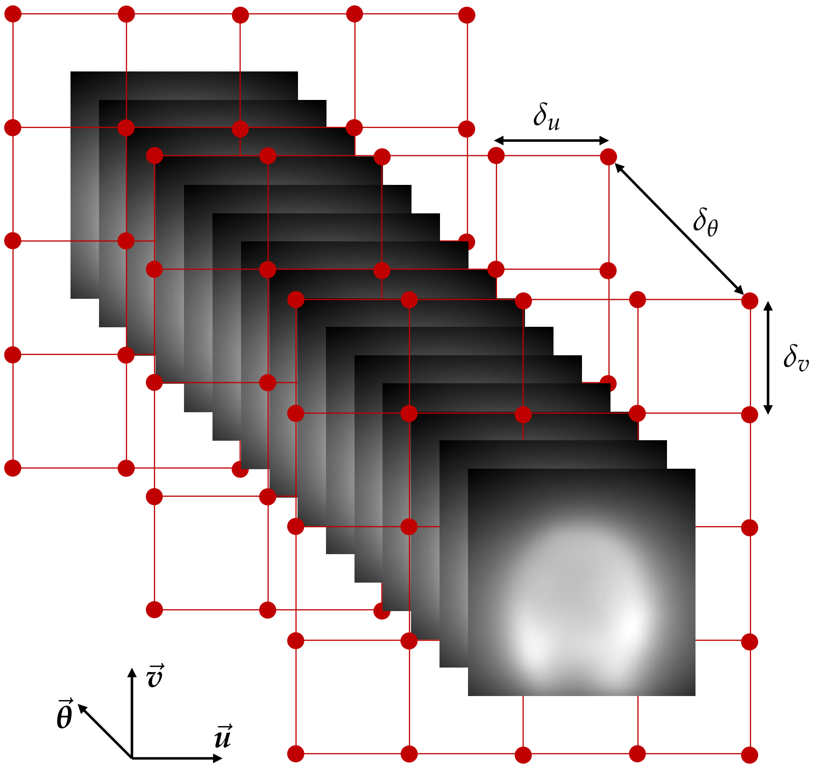

Figure 4.4 – Illustration of the B-spline knots distribution in a regular lattice.

piece-wise constant scatter maps and is therefore equivalent to the scatter model used in [69], [70] and [71].

4.5 Weighting according to mask and object structures

As explained in 3.3.4, the object structures cannot be neglected, in particular in the neighbourhood of the edges of the object. The use of two specific weighting matrices in the cost function tackles this issue.

The primary gradient evaluated in pixels out of the modulator mask edges (either in the holes or in regions with constant thickness) contains only information about the object structures, and nothing about the persistence of the mask footprint in the primary map. As a consequence, we only need to evaluate the spatial gradient of the primary map on the mask edges. This can be done by weighting the spatial gradient of the primary map by the spatial gradient of the mask image, which can be achieved using the following weighting matrix:

$$\boldsymbol{W}_1 = \operatorname{diag}(\boldsymbol{\nabla}\hat{\boldsymbol{p}}^0), \tag{4.23}$$

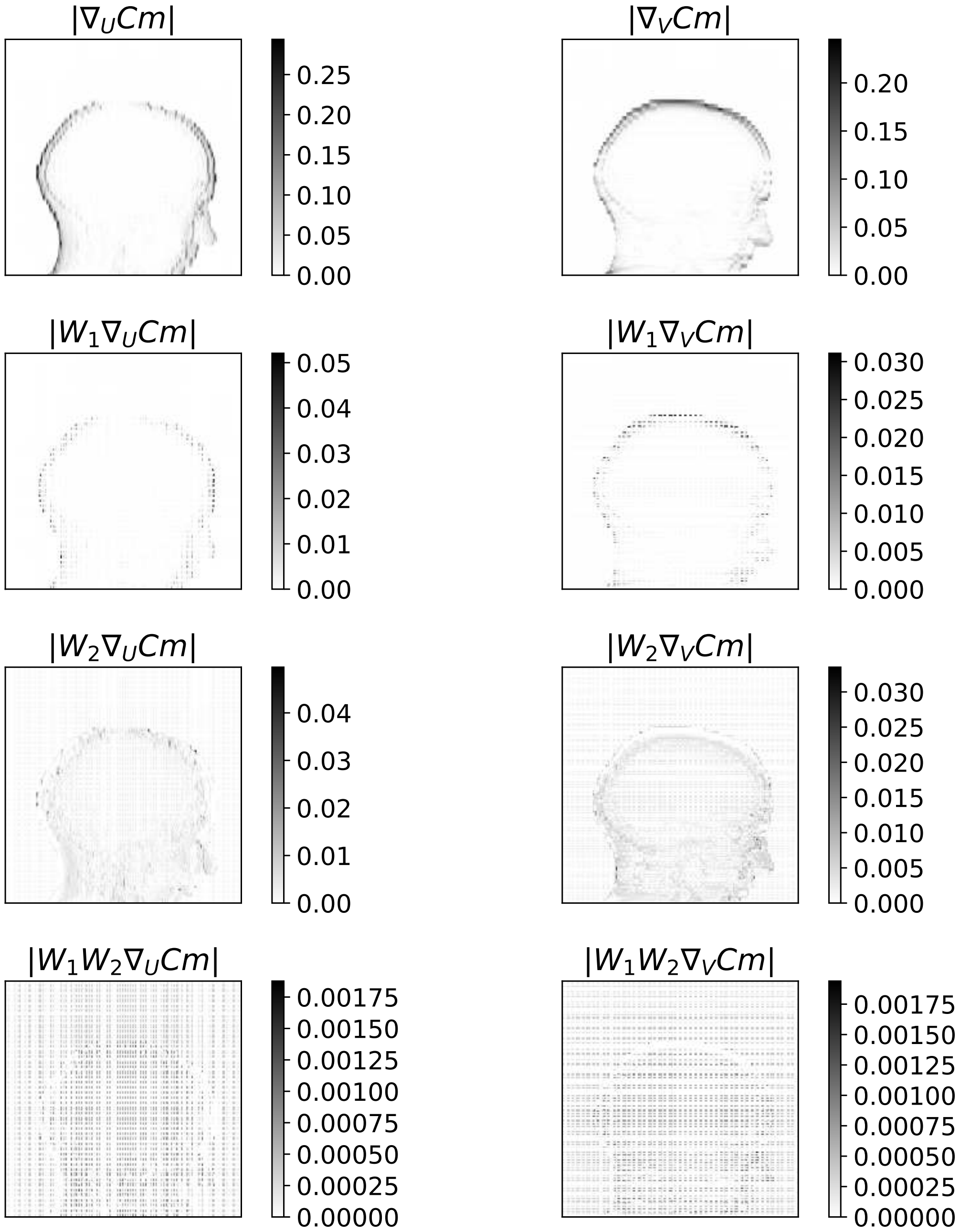

Figure 4.5 – Illustration of the effects of weighting matrices: left and right columns represent respectively the gradient in the u and v directions. First row is without weighting, second with $\boldsymbol{W}_1$, third with $\boldsymbol{W}_2$ and the fourth with both $\boldsymbol{W}_1$ and $\boldsymbol{W}_2$.

where $\hat{\boldsymbol{p}}^0$ is the image with the mask but without any object. Figure 4.5 illustrates the effect of $\boldsymbol{W}_1$ on the gradient of the scatter-corrupted measured image after the application of the correction matrix: left column represents the gradient image in the u-direction and the right one the gradient in the v-direction, while the first and second rows represent the gradient without and with the multiplication by $\boldsymbol{W}_1$, respectively. The weighting matrix isolates the pixels of interest but the object structures, which should not be accounted for in the cost function, remain predominant in particular at the edges of the object.

This implies the necessity to introduce an additional weighting matrix which lowers the impact of the object structures. In this work, we reuse the penalty weighting introduced in [70]:

$$\boldsymbol{W}_2 = \operatorname{diag}\left(\exp(-\eta|\boldsymbol{\nabla}\tilde{\boldsymbol{p}}|)\right), \tag{4.24}$$

with η a positive scalar parameter and $\boldsymbol{\nabla}\tilde{\boldsymbol{p}} \in \mathbb{R}^{2N_B N_U N_V N_\Theta}$ an estimation of the primary gradient map from the measured sinogram $\hat{\boldsymbol{t}}$.

In [70], the unknown object gradient $\boldsymbol{\nabla}\tilde{\boldsymbol{p}}$ was estimated as the gradient of a first estimation of the primary image, obtained by neglecting the object structures (with $\boldsymbol{W}_2 = \boldsymbol{I}$). Unfortunately, this initial estimation of the primary map will contain the mask footprint since scatter is imperfectly estimated and it will be considered as object structure. In this case, the effect of $\boldsymbol{W}_2$ would be counterproductive. In our work, the primary gradient is directly estimated from the gradient of the measure corrected for the modulator mask, $\boldsymbol{\nabla}\boldsymbol{C}\hat{\boldsymbol{t}}$. Indeed, the primary gradient is directly related to the gradient of the corrected measured image:

$$\boldsymbol{\nabla}\boldsymbol{p} = \boldsymbol{\nabla}\boldsymbol{C}\hat{\boldsymbol{t}} - \boldsymbol{\nabla}\boldsymbol{C}\boldsymbol{s}. \tag{4.25}$$

Neglecting the spatial gradient of the scatter map, the primary gradient is equal to the gradient of the corrected measured image in pixels where there is no mask structure (i.e. where $\|\boldsymbol{\nabla}\hat{\boldsymbol{p}}^0_{u,v}\| = 0$). The primary gradient in pixels containing mask structure is then linearly interpolated. Third row of figure 4.5 shows the effect of the use of $\boldsymbol{W}_2$: the weighted gradient in regions where the object is spatially structured is smaller than in regions where the object is less structured, e.g in the brain.

The full benefit of the weighting matrices is more evident on the last row of figure 4.5, where almost the totality of the weighted gradient comes from the scatter induced bias.

4.6 Cost function

Following the B-spline model detailed in section 4.4, the scatter estimation comes down to the estimation of the B-spline coefficients at each energy bin. In order to improve the conditioning of this estimation problem, we choose to add a regularization term to the cost function which gives the following estimation of the scatter map parameters:

$$\tilde{\boldsymbol{x}} \in \operatorname*{arg\,min}_{\boldsymbol{x}\in\mathbb{R}^{N_B N_K}} \mathcal{F}(\boldsymbol{x}) + \mathcal{R}(\boldsymbol{x}), \tag{4.26}$$

with

- $\mathcal{F}(\boldsymbol{x}) = \left\|\boldsymbol{W}_1\boldsymbol{W}_2\boldsymbol{\nabla}\boldsymbol{C}(\hat{\boldsymbol{t}} - \boldsymbol{B}\boldsymbol{x})\right\|_{1,\sigma}$,
  where $\boldsymbol{W}_1$ and $\boldsymbol{W}_2$ are the weighting matrices described above and $\|\cdot\|_{1,\sigma}$ is a smooth approximation of the ℓ^1 norm for this data-fidelity term [75] defined as

  $$\|\boldsymbol{y}\|_{1,\sigma} = \sum_n \sqrt{y_n^2 + \sigma^2} - \sigma, \tag{4.27}$$

  with σ a strictly positive smoothing scalar parameter. More information about this approximation of the ℓ_1 norm can be found in appendix A.
- $\mathcal{R}(\boldsymbol{x}) = \|\boldsymbol{T}\boldsymbol{x}\|_2^2$,
  where $\boldsymbol{T}$ is the diagonal matrix which energy-dependent elements τ_b control the strength of Tikhonov's regularization in each energy bin.

From the estimate of the scatter map parameters $\tilde{\boldsymbol{x}}$, the primary map is finally deduced by incorporating 4.22 into 4.3:

$$\tilde{\boldsymbol{p}} = \boldsymbol{C}(\hat{\boldsymbol{t}} - \boldsymbol{B}\tilde{\boldsymbol{x}}). \tag{4.28}$$

4.7 Scalar parameters to be tuned

We have presented the whole cost function that we designed to solve the problem. This cost function is based on positive scalar parameters which have to be tuned. We present hereunder an exhaustive list of these parameters along with their description:

- η: parameter controlling the strength of the weighting according to the object structures.
- σ: smoothing parameter of the ℓ^1 norm approximation.
- τ_b: energy dependent Tikhonov regularization parameters.
- δ_u: B-spline spacing in the u direction.
- δ_v: B-spline spacing in the v direction.
- δ_θ: B-spline spacing in the θ direction.

4.8 Optimization

We propose to solve 4.26 using Newton's method, starting with an initial guess $\boldsymbol{x}^{(0)} = 0$ and building new estimates with the following update rule:

$$\boldsymbol{x}^{(n+1)} = \boldsymbol{x}^{(n)} + \delta\boldsymbol{x}^{(n)}, \tag{4.29}$$

where $\delta \boldsymbol{x}^{(n)} \in \mathbb{R}^{N_B N_K}$ denotes Newton's step at iteration (n). Newton's step is obtained solving

$$\left(\boldsymbol{H}[\mathcal{F}](\boldsymbol{x}^{(n)}) + \boldsymbol{T}^T \boldsymbol{T} \right) \delta \boldsymbol{x}^{(n)} = -\boldsymbol{\nabla}[\mathcal{F}](\boldsymbol{x}^{(n)}) - \boldsymbol{T}^T \boldsymbol{T} \boldsymbol{x}^{(n)}, \tag{4.30}$$

with $\boldsymbol{\nabla}[\mathcal{F}](\boldsymbol{x}^{(n)})$ and $\boldsymbol{H}[\mathcal{F}](\boldsymbol{x}^{(n)})$ the gradient and the Hessian of the data-fidelity term $\mathcal{F}$ at iteration (n), respectively. Their expressions are given by:

$$\begin{cases} \boldsymbol{\nabla}[\mathcal{F}](\boldsymbol{x}^{(n)}) & = \boldsymbol{A}^T \boldsymbol{M}^{(n)} (\boldsymbol{b} - \boldsymbol{A}\boldsymbol{x}^{(n)}) \\ \boldsymbol{H}[\mathcal{F}](\boldsymbol{x}^{(n)}) & = \boldsymbol{A}^T (\boldsymbol{M}^{(n)} - \boldsymbol{N}^{(n)}) \boldsymbol{A} \end{cases} \tag{4.31}$$

where

$$\begin{cases} \boldsymbol{b} & = \boldsymbol{W}_1 \boldsymbol{W}_2 \boldsymbol{\nabla} \boldsymbol{C} \boldsymbol{m} \\ \boldsymbol{A} & = \boldsymbol{W}_1 \boldsymbol{W}_2 \boldsymbol{\nabla} \boldsymbol{C} \boldsymbol{B} \\ \boldsymbol{M}^{(n)} & = \operatorname{diag} \left(\left((\boldsymbol{b} - \boldsymbol{A}\boldsymbol{x}^{(n)})^2 + \sigma^2 \right)^{-\frac{1}{2}} \right) \\ \boldsymbol{N}^{(n)} & = \operatorname{diag} \left((\boldsymbol{b} - \boldsymbol{A}\boldsymbol{x}^{(n)})^2 \left((\boldsymbol{b} - \boldsymbol{A}\boldsymbol{x}^{(n)})^2 + \sigma^2 \right)^{-\frac{3}{2}} \right). \end{cases} \tag{4.32}$$

In practice, a very few iterations of equation 4.29 were sufficient to recover the scatter map in our experiments which indicates that the cost function is nearly quadratic.

4.9 Conclusion

In this chapter, we presented a scatter correction method using a semi-transparent primary modulator mask adapted to multi-energy computed tomography imaging. We have first reminded the principle of a gradient-based primary modulation scatter correction method according to the literature, but applied to images acquired with a photon counting detector. We have then presented the correction matrix, which compensates for the mask attenuation with limited beam-hardening and a three dimensional scatter model based on B-splines lowering the dimensionality of the problem. Specific weightings according to the mask and the object structures were then depicted. They relax the assumption of locally smooths primary images. We also presented a regularized cost function to minimize, with a data fidelity term based on a smooth approximation of the ℓ^1 norm. Finally, after having listed the scalar parameters which have to be tuned prior to the application of the method, we presented the optimization algorithm that we used for minimizing the cost function: Newton's method. This method is tested on realistic simulated images in the next chapter.

5

Evaluation of the method on simulated data

5.1 Introduction

We presented in chapter 4 a scatter correction method based on the use of a semi-transparent primary modulator mask and adapted to spectral computed tomography imaging. The hereunder chapter is dedicated to the evaluation of this method on realistic simulated data. First, the simulation set-up is presented in section 5.2. The correction matrix is then evaluated according to various mask materials and number of energy bins in section 5.3. Section 5.4 aims at evaluating the B-splines based scatter model according to several spacings and orders. Finally, the results obtained with the full method are presented in section 5.5 and discussed in section 5.6.

5.2 Simulation set-up

A medical cone-beam CT scanner was simulated with the geometry described in figure 5.1. The simulated spectrum corresponds to a tungsten x-ray tube with an anode angle of 30° operating at 120 kV and 0.2 mAs.

An energy-resolved photon counting detector (PCD) with 1024×1024 pixels with a pitch of 400 μm and a 3 mm thick CdTe sensor has been simulated using an internal software, mimicking an existing energy-resolved detector [11]. The pixels were binned such that one pixel regroups 16 detector pixels (4×4) and $N_U = N_V = 256$. The same simulated DRM was used for all pixels, which is also binned in the energy domain according to table 5.1.

Pile-up effects were not simulated. Poisson noise was simulated from the images of the expected number of photons, except the images without object which were assumed to be noise free. Images without object are the white image, the mask image and the calibration images used for the estimation of the correction matrix. We simu-

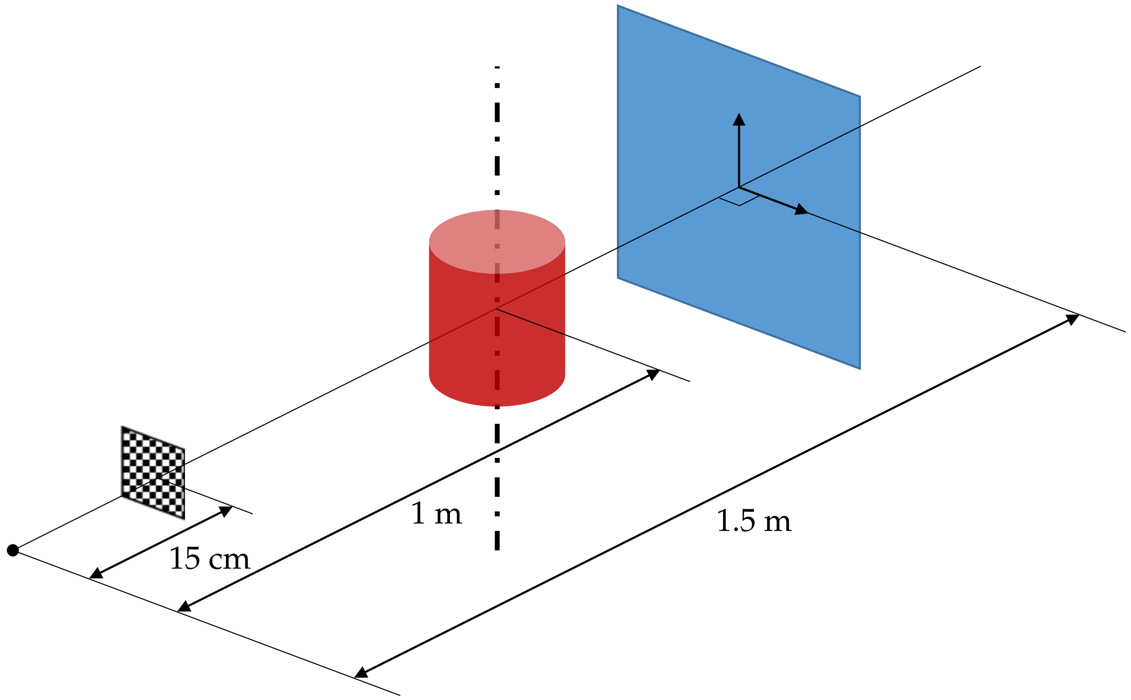

Figure 5.1 – Simulation set-up

lated a CT scan of the head of the ICRP realistic anthropomorphic phantom [76] with 360 deterministic primary projections and 36 scatter projections using fixed-forced detection with one million particles per projection, both with Gate (version 8.0, Livermore physics list) [77]. The scatter maps were then interpolated with quadratic B-splines in order to obtain the 360 projections corresponding to the simulated primary maps.

The primary modulator mask is a slab made with a given material and with a thickness from 0.1 mm to 5 mm (the design of the mask is discussed in section 5.3), drilled by 3 mm wide square holes every 5 mm. The transmission image $\hat{\boldsymbol{p}}^0$ of a 5 mm graphite mask at energy bin 2 is shown in figure 5.2.

5.3 Correction matrix evaluation

The objective of this section is to evaluate the correction matrix presented in 4.3, according to three different low-Z materials for the primary modulator mask : graphite (carbon, $Z = 6$), aluminum ($Z = 13$) and copper ($Z = 29$), and to several energy bin numbers N_B.

b	Energy range
1	30 keV to 40 keV
2	40 keV to 50 keV
3	50 keV to 60 keV
4	60 keV to 72 keV
5	72 keV to 84 keV
6	84 keV to 96 keV
7	96 keV to 108 keV
8	108 keV to 120 keV

Table 5.1 – Relation between bin index and energy range for $N_B = 8$

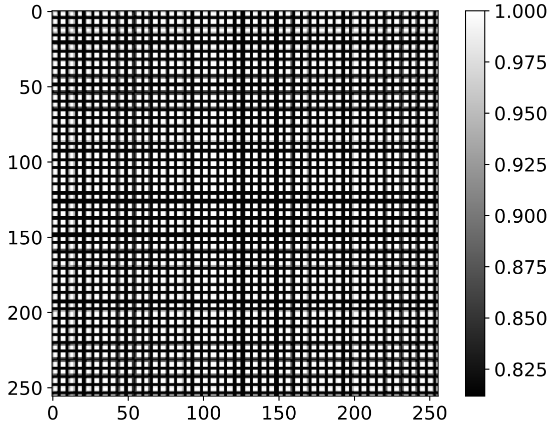

Figure 5.2 – Transmission image of the mask at energy bin 2

Calibration datasets The estimation of the correction matrix requires a calibration dataset. In this work, we opted for a set of acquisitions with thickness combinations of polymethyl-methacrylate (PMMA) and aluminum slabs. The thicknesses are presented in table 5.2, resulting in a dataset of $N^{\text{cal}} = 20$ calibration couples of images for each case.

The analysis of the influence of the mask material was made with $N_B = 8$ energy bins while the influence of the energy bins number was studied using a mask made with graphite. For the latter, we tested eight cases ($N_B = 1, 2, 4, 6, 8, 12, 16, 24$) and the relations between the bin indices and the corresponding energy range are given in appendix B.

Results The quantitative evaluation of the correction matrix performance according to the mask material was made with the mean relative error per energy bin (MRE_b)

l^{PMMA}	l^{Al}
0 cm	0 mm
2 cm	1 mm
4 cm	
6 cm	
8 cm	
10 cm	
12 cm	
14 cm	
16 cm	
18 cm	

Table 5.2 – Thicknesses of PMMA and aluminum for the calibration dataset

on the noise-free and scatter-free calibration database itself:

$$MRE_b = 100 \times \frac{1}{N^{\mathrm{cal}} N_U N_V} \sum_{k=1}^{N^{\mathrm{cal}}} \sum_{u=1}^{N_U} \sum_{v=1}^{N_V} \frac{|p_{k,b,u,v} - \boldsymbol{c}_{b,u,v}^T \hat{\boldsymbol{p}}_{k,u,v}|}{p_{k,b,u,v}}, \tag{5.1}$$

where $\boldsymbol{p}_k$ and $\hat{\boldsymbol{p}}_k$ are the images of the k-st calibration acquisition, without any mask and with the mask respectively, and $\boldsymbol{c}_{b,u,v}$ the row of the correction matrix of pixel (u, v) corresponding to energy bin b.

For the study of the influence of the number of energy bins N_B, we used the mean relative error defined as:

$$MRE = 100 \times \frac{1}{N^{\mathrm{cal}} N_B N_U N_V} \sum_{k=1}^{N^{\mathrm{cal}}} \sum_{u=1}^{N_U} \sum_{b=1}^{N_B} \sum_{v=1}^{N_V} \frac{|p_{k,b,u,v} - \boldsymbol{c}_{b,u,v}^T \hat{\boldsymbol{p}}_{k,u,v}|}{p_{k,b,u,v}}. \tag{5.2}$$

Figure 5.3 shows the mean relative errors induced by the correction matrix on the calibration dataset as a function of the mask material, while figure 5.4 presents the error as a function of the energy bins number N_B.

Discussion The inaccuracy of the compensation for the mask attenuation comes from the inaccuracy of the model itself (which may be improved) and the beam-hardening effect induced by the variations of the linear attenuation coefficient of the mask material along the energy range of the source spectrum. In order to minimize the latter, materials with slowly-variant attenuation in the diagnostic energy range (i.e. low-Z materials such that carbon, aluminum or copper) have to be favored and materials with K-edge have to be avoided.

The thickness of the primary modulator must be chosen according to several issues. First, the parallax effect increases with the mask thickness, and tends to lower

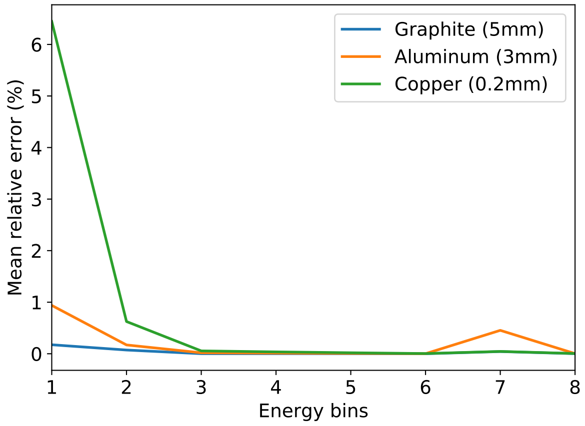

Figure 5.3 – Mean relative error per energy bins N_B according to the mask material

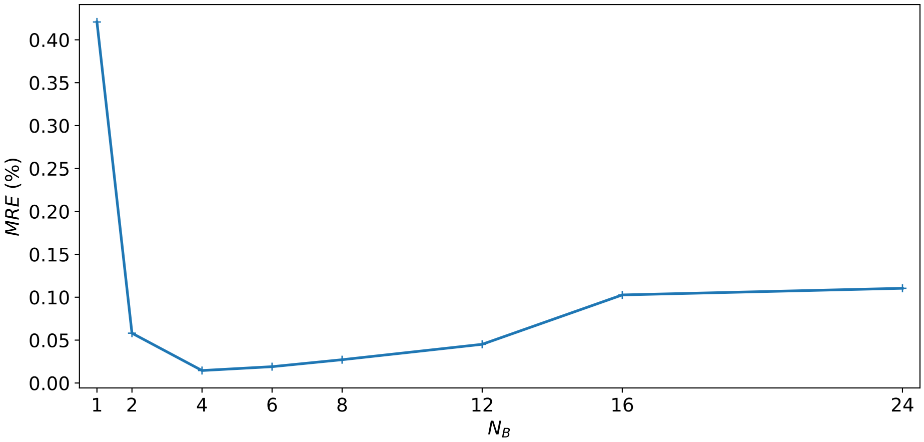

Figure 5.4 – Mean relative error according to the number of energy bins N_B

the sharpness of the mask edges seen in the images. Then, the intensity of the mask pattern visible in the estimated primary when the estimation of the scatter map is not correct increases with the mask thickness (see equation 3.8). It means that the sensitivity of the scatter estimation is bad when the mask attenuation is too low (i.e. the mask is too thin). Another issue concerns the variations of the noise level in the images. The statistical noise in pixels attenuated by the mask is greater than in unattenuated ones (for equivalent magnitudes of object attenuation). A great spatial variability of statistical noise may be a problem and the mask thickness has therefore to be limited. Finally, even using a mask material with a slowly variant LAC, the beam-hardening effect will degrade the accuracy of the mask attenuation compensation. Considering all these issues, a trade-off must be found and we proposed to design the mask thickness such that it stops around $10 - 20$ % of photons emitted by the source in each energy bin.

The thickness chosen for the mask is 5 mm for a graphite primary modulator mask, 3 mm for a aluminum one and 0.2 mm for a copper one. The resulting transmission factors presented in figure 5.5 show that the transmission factor of graphite is almost constant over the energy range, unlike the one of aluminum and, a fortiori, copper. This will lead to great variations of the correction matrix induced error along the energy for aluminum and copper, as confirmed in figure 5.3, where the error at low energy is significantly larger for aluminum and copper.

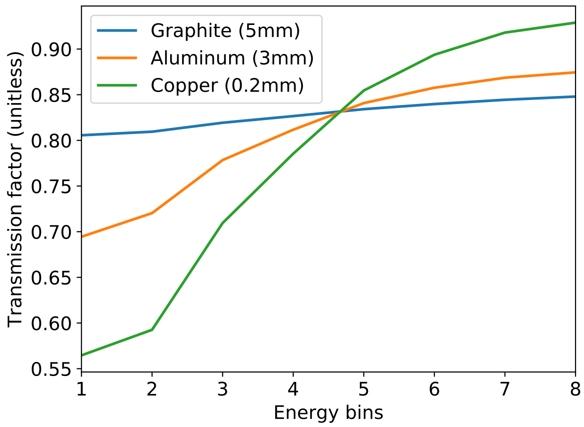

Figure 5.5 – Transmission factors of the mask made with graphite (blue), aluminum (orange) and copper (green)

The correction matrix, computed according to the Dirac-negative-exponential model, gives satisfying results in terms of compensation for the graphite primary modulator mask attenuation. However, the compensation accuracy highly depends on the mask material, in particular at low energy. This leads to the conclusion that the best solution for the mask material is graphite.

To conclude on the design of the primary modulator mask, one can say that the mask must have as many edges as possible in order to have enough pixels with mask edges. As a consequence, the mask pattern should be as small as possible, considering the mechanical properties of the mask material and its thickness. Unfortunately, graphite has far worse mechanical properties than aluminum and copper and the pattern cannot be as small as it would be with aluminum or copper.

The inaccuracy of the correction matrix also depends on the number of energy bins, as one can see on figure 5.4 where the minimal error is between two and twelve energy bins. The error increase for low number of energy bins is mostly caused by the beam-hardening effect in the modulator mask while the increase for high numbers of energy bins is mainly due to the degradation of the model accuracy. In addition, it is worth noting that this study was performed using noise-free data. At fixed noise acquisition conditions, the noise in a given energy bin will be greater in thinner energy bins resulting in greater errors caused by statistical noise. Considering these issues, we opted for the case $N_B = 8$ energy bins for the rest of this thesis, which is an acceptable trade-off between beam-hardening, correction matrix model inaccuracy, noise levels in each energy bin and the will to demonstrate the ability of the method to provide accurate spectral images.

5.4 Scatter model evaluation

The objective of the following section is to evaluate the B-spline based scatter model introduced in 4.4 according to the B-splines order and the spacings between two knots. In this study, we have used noise-free images.

Estimation of the model parameters In order to compare the simulated scatter images with their representation using B-spline basis functions, we need an estimation procedure for the optimal B-spline coefficients at a given energy bin b. We chose to estimate them as follows:

$$\tilde{\boldsymbol{x}} \in \underset{\boldsymbol{x} \in \mathbb{R}^{N_B N_K}}{\arg\min} \|\boldsymbol{s} - \boldsymbol{B}\boldsymbol{x}\|_2^2. \tag{5.3}$$

Results The evaluation of the scatter model requires an error function able to quantify its inaccuracy. We opted for a criterion based on the estimated primary: the mean relative primary error (MRE) which is computed with the following expression:

$$MRE = 100 \times \frac{1}{N_B N_U N_V N_\Theta} \sum_{b=1}^{N_B} \sum_{u=1}^{N_U} \sum_{v=1}^{N_V} \sum_{\theta=1}^{N_\Theta} \frac{|p_{b,u,v,\theta} - \tilde{p}_{b,u,v,\theta}|}{p_{b,u,v,\theta}}, \tag{5.4}$$

where the estimated primary $\tilde{\boldsymbol{p}}$ is given by:

$$\tilde{\boldsymbol{p}} = \boldsymbol{t} - \boldsymbol{B}\tilde{\boldsymbol{x}}. \tag{5.5}$$

In addition, we quantify the error dispersion using the mean deviation (MD) computed as:

$$MD = \frac{1}{N_B N_U N_V N_\Theta} \sum_{b=1}^{N_B} \sum_{u=1}^{N_U} \sum_{v=1}^{N_V} \sum_{\theta=1}^{N_\Theta} |MRE - 100 \times \frac{|p_{b,u,v,\theta} - \tilde{p}_{b,u,v,\theta}|}{p_{b,u,v,\theta}}|. \tag{5.6}$$

The mean relative errors along with the mean deviations according to the B-splines order are given in table 5.3 at fixed detector and angular spacings: $\delta_u = \delta_v = 128$ pixels and $\delta_\theta = 15°$.

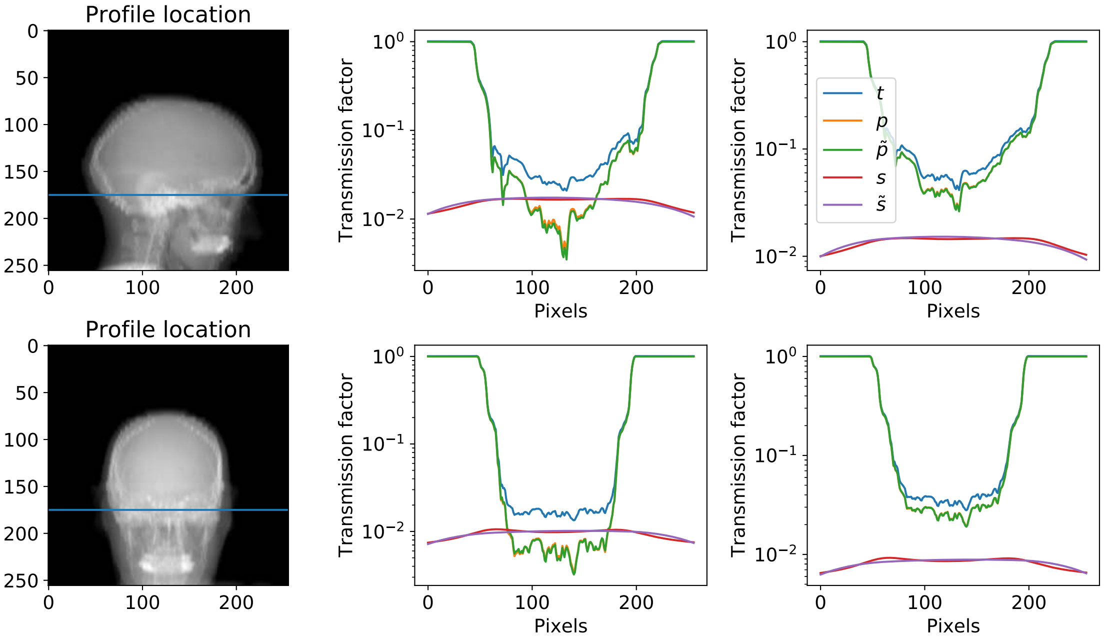

Figure 5.6 – Profiles of two projections at energy bins 2 (center) and 6 (right). Reference and estimated scatter are in red and purple respectively, total is in blue and reference and estimated primary are in orange and green respectively.

B-spline order	MRE (%)	MD (%)
0	0.74	0.93
1	0.69	0.93
2	0.50	0.67
3	0.49	0.66

Table 5.3 – Mean relative errors and mean deviations according to the B-spline order

Table 5.4 presents the relative errors and mean deviations using 2-nd order B-splines for several angular spacings from 5° to 25° at fixed detector spacings ($\delta_u = \delta_v = 128$ pixels). In addition, table 5.5 shows the relative errors and mean deviations, still using 2-nd order B-splines, for several detector spacings from 16 to 256 pixels at fixed angular spacing $\delta_\theta = 15°$.

Figure 5.6 shows profiles of the transmission factors for two projections where the estimated scatter and primary are computed according to 5.3 and 5.5 with the second order B-splines, $\delta_u = \delta_v = 128$ pixels and $\delta_\theta = 15°$. The central column corresponds to energy bin 2 and the right one to bin 6.

δ_θ	*MRE* (%)	*MD* (%)
5°	0.48	0.65
10°	0.48	0.65
15°	0.50	0.67
20°	0.53	0.71
25°	1.08	1.56

Table 5.4 – Mean relative errors and mean deviations according to the angular B-spline spacings δ_θ at fixed detector spacings $\delta_u = \delta_v = 128$ pixels.

δ_u,δ_v	*MRE* (%)	*MD* (%)
16 pixels	0.42	0.57
32 pixels	0.42	0.57
64 pixels	0.42	0.57
128 pixels	0.50	0.67
256 pixels	0.58	0.78

Table 5.5 – Mean relative errors and mean deviations according to the detector B-spline spacings δ_u and δ_v at fixed angular spacing $\delta_\theta = 15°$.

Discussion The larger errors and deviations obtained for orders 0 and 1 (table 5.3) were expected as they do not allow a smooth representation of scatter maps. There is however almost no improvement with order 3 B-splines compared to order 2 ones. Since the B-spline matrix $\boldsymbol{B}$ is sparser for lower order, order 2 B-spline basis functions are the best choice for the scatter model. The relative error according to the angular spacing (table 5.4) is almost stable up to 20° and is significantly larger for $\delta_\theta = 25°$, as well as for the mean deviation. In addition, the influence of the detector spacing up to 64 pixels is negligible and the error obtained for $\delta_u = \delta_v = 128$ pixels remains low, as its mean deviation.

The objective of the model being to represent accurate scatter images with as few parameters as possible, a trade-off must be found according to an acceptable error magnitude. In this work, we arbitrary consider as satisfactory enough the B-spline orders and spacings which associated mean error and mean deviation are not greater than 0.5 % and 0.7 % respectively. According to the latter, we consider order 2 B-splines with $\delta_u = \delta_v = 128$ pixels and $\delta_\theta = 15°$ as a good choice for the scatter model.

Observing the reference and estimated scatter on figure 5.6, it seems that the spacings are too large to fit perfectly with the small variations of scatter. However, the final objective is not to recover the scatter map but the primary one. In figure 5.6, reference and estimated primary profiles fit very well even in regions where the reference and estimated scatter does not fit (e.g near pixels 30 and 200 of the first projection or near pixels 60 and 230 of the second one). A sensitive (but very small) bias can only be seen near pixel 120 of the first projection and at low energy, even if the bias on scatter is low.

Finally, the accuracy of a B-spline based model for representing scatter maps highly depends on their order and the spacings between two knots. We have also seen that, even if accurate scatter maps require a lot of knots, the recovery of an accurate primary map is possible with the use of a very few knots. This was the case on the simulated head data. However, in case of lower air-gap or greater object attenuation, the high frequencies of scatter will increase and more B-spline knots may be necessary. In this work, the B-spline knots are regularly distributed but their position may be optimized in order to improve the model accuracy without increasing the number of B-spline knots.

5.5 Results

The proposed scatter correction method has been tested on the simulated dataset presented in 5.2 using a 5 mm thick primary modulator mask. The scatter model is the one chosen previously, with $\delta_u = \delta_v = 128$ pixels and $\delta_\theta = 15°$. The scalar parameters η (defined in equation 4.24) and σ (defined in equation 4.27) were tuned with a grid search and the regularization parameters τ_b (defined in the diagonal matrix $\boldsymbol{T}$ in equation 4.26) manually. The tuning of these parameters is discussed later in section 5.6. Their values are given in table 5.6.

Parameter	Value
η	2×10^{0}
σ	3×10^{-3}
τ_1	5×10^{0}
τ_2	2×10^{-1}
τ_3	1×10^{-1}
τ_4	8×10^{-2}
τ_5	5×10^{-2}
τ_6	2×10^{-2}
τ_7	1×10^{-2}
τ_8	1×10^{-2}
δ_u	128 pixels
δ_v	128 pixels
δ_θ	15°

Table 5.6 – Scalar parameters for the simulation case

We performed fourteen iterations of equation 4.29, starting with a null initial guess $\boldsymbol{x}^{(0)} = \boldsymbol{0}$. Figure 5.7 shows the evolution of the cost function as a function of the iterations. The following results are taken at iteration $n = 14$.

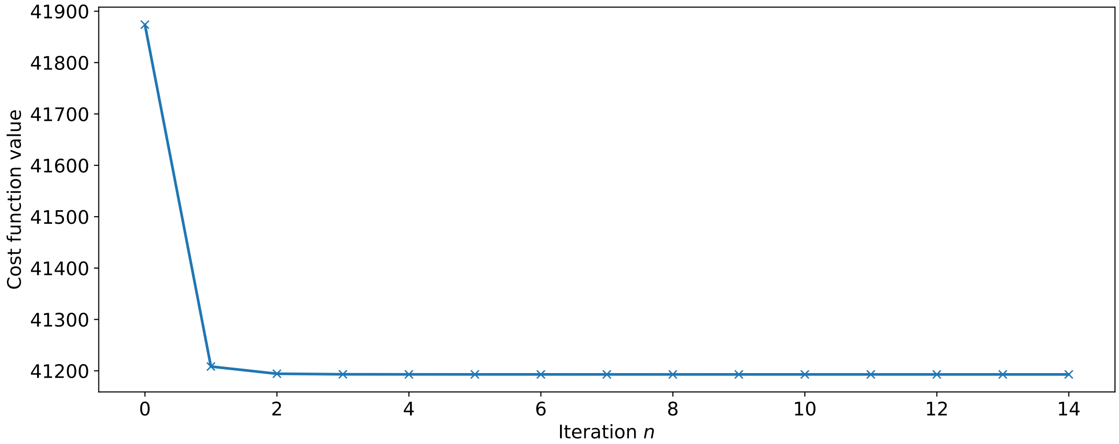

Figure 5.7 – Evolution of the cost function according to the iterations

Total, reference primary and estimated primary attenuation images at two projection angles are presented in figure 5.8. The left and right parts of images represent respectively low and high energy bins (2 and 6). Profiles of these projections are shown as transmission factors in figure 5.9 at low (center) and high energy (right). The measured, corrected and total transmission factors are the blue, orange and green curves, respectively. Reference and estimated primary signals are plotted in red and purple, while reference and estimated scatter are in brown and pink, respectively.

Three pixels of interest (POI) corresponding to various levels of attenuation have been isolated. Their associated attenuation spectra are plotted on figure 5.10, where the blue curves represent total attenuation while the orange and green ones represent the reference and estimated primary, respectively.

For the quantitative evaluation of the method, we used the mean relative error (MRE) on the transmission sinograms. For example, the mean relative error associated with the estimated primary is given by the following expression:

$$MRE^{\tilde{p}} = 100 \times \frac{1}{N_B N_U N_V N_\Theta} \sum_{b=1}^{N_B} \sum_{u=1}^{N_U} \sum_{v=1}^{N_V} \sum_{\theta=1}^{N_\Theta} \frac{|\bar{p}_{b,u,v,\theta} - \tilde{p}_{b,u,v,\theta}|}{\bar{p}_{b,u,v,\theta}}, \tag{5.7}$$

where $\bar{p}$ is the noise-free primary transmission sinogram. Again, we use the mean deviation (MD) for quantifying the error dispersion. For the estimation primary, its expression is:

$$MD^{\tilde{p}} = \frac{1}{N_B N_U N_V N_\Theta} \sum_{b=1}^{N_B} \sum_{u=1}^{N_U} \sum_{v=1}^{N_V} \sum_{\theta=1}^{N_\Theta} |MRE^{\tilde{p}} - 100 \times \frac{|\bar{p}_{b,u,v,\theta} - \tilde{p}_{b,u,v,\theta}|}{\bar{p}_{b,u,v,\theta}}|. \tag{5.8}$$

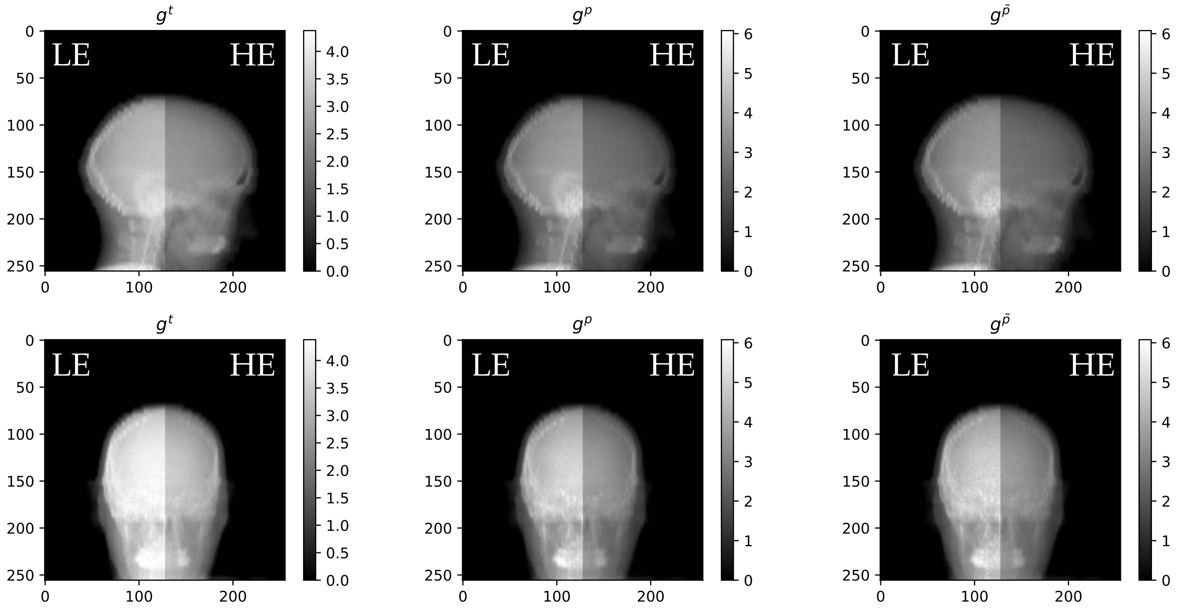

Figure 5.8 – Two projections of total (left), primary (center) and estimated primary (right) attenuation at low energy (LE, bin 2) and high energy (HE, bin 6)

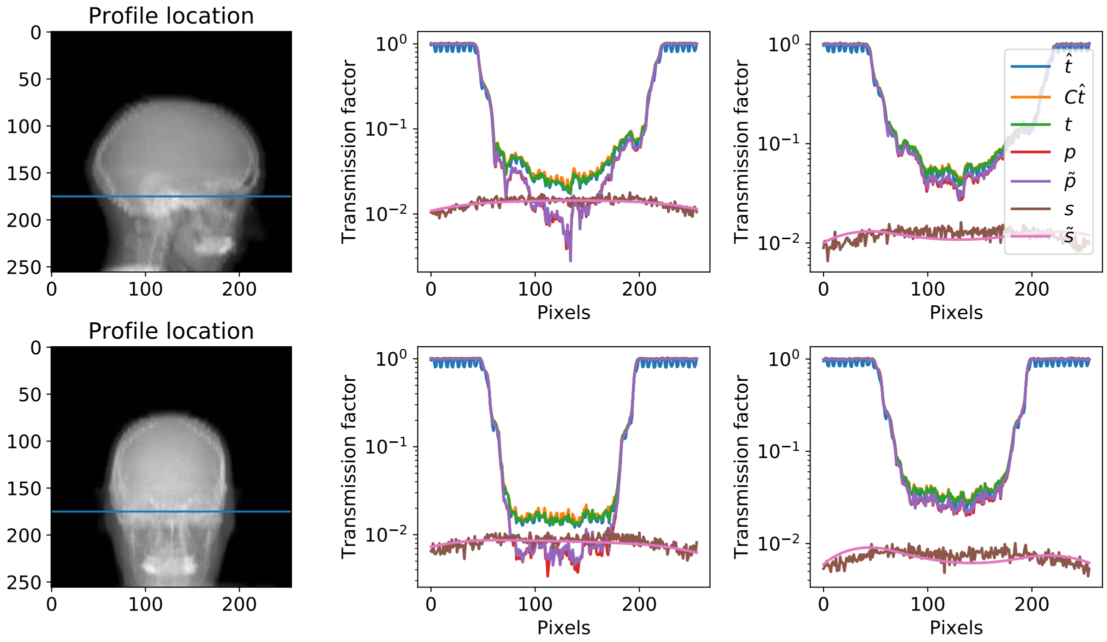

Figure 5.9 – Profiles of two projections at energy bins 2 (center) and 6 (right).

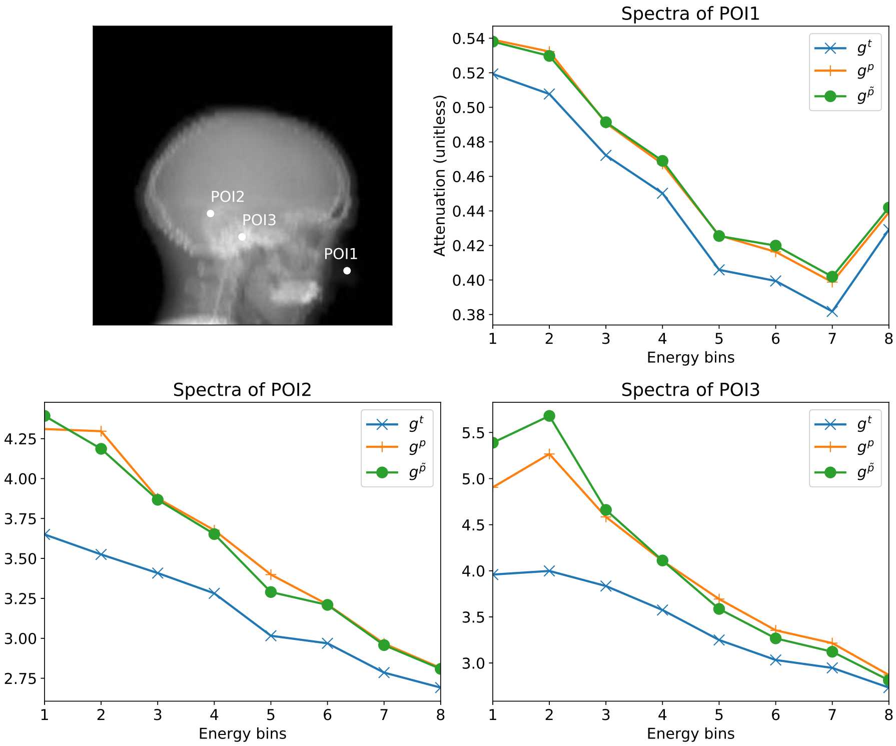

Figure 5.10 – Attenuation spectra of three pixels of interest (POI)

MRE for total, reference primary and estimated primary are given in table 5.7 along with the corresponding mean error deviations MD. The evolution of the MRE as a function of the iterations is presented in figure 5.11 (blue curve). For comparison, we also plotted the error associated with the reference primary MRE^p and the one corresponding to the ℓ^2 norm instead of the Charbonnier function in the data-fidelity term of the cost function.

	MRE (%)	MD (%)
Total	10.7	13.2
Reference primary	1.96	1.74
Estimated primary	2.88	2.84

Table 5.7 – Mean relative errors and mean error deviations of total, reference primary and estimated primary transmission sinograms

We also use the mean relative error per energy bin MRE_b and the mean relative

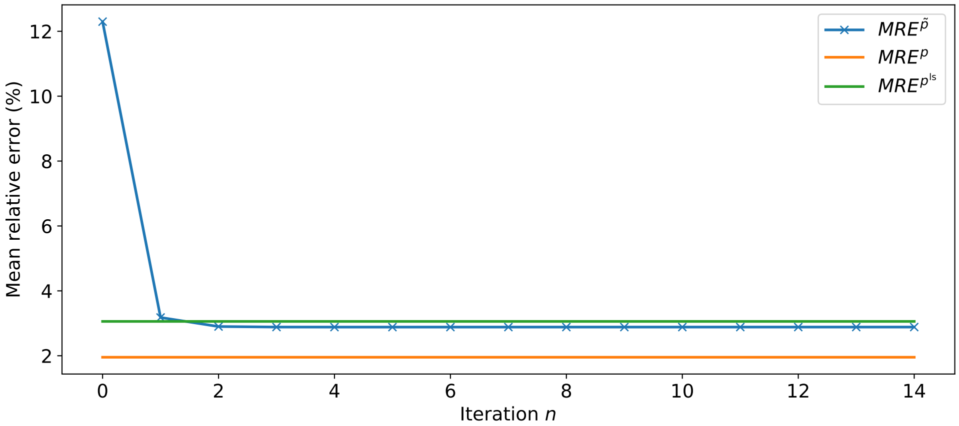

Figure 5.11 – Evolution of the mean relative error associated with the estimated primary according to the iterations (blue) and errors associated with the reference primary (orange) and with the estimated primary using ℓ^2 norm instead of our ℓ^1 norm approximation (green).

error per projection angle MRE_θ given by:

$$MRE_b^{\tilde{p}} = \frac{1}{N_U N_V N_\Theta} \sum_{u=1}^{N_U} \sum_{v=1}^{N_V} \sum_{\theta=1}^{N_\Theta} \frac{|\bar{p}_{b,u,v,\theta} - \tilde{p}_{b,u,v,\theta}|}{\bar{p}_{b,u,v,\theta}}, \tag{5.9}$$

and

$$MRE_\theta^{\tilde{p}} = \frac{1}{N_B N_U N_V} \sum_{b=1}^{N_B} \sum_{u=1}^{N_U} \sum_{v=1}^{N_V} \frac{|\bar{p}_{b,u,v,\theta} - \tilde{p}_{b,u,v,\theta}|}{\bar{p}_{b,u,v,\theta}}, \tag{5.10}$$

respectively. In addition, we use the mean error deviation per energy bin MD_b and the mean error deviation per projection angle MD_θ in order to evaluate the error dispersion. They are computed according to the following expressions:

$$MD_b^{\tilde{p}} = \frac{1}{N_U N_V N_\Theta} \sum_{u=1}^{N_U} \sum_{v=1}^{N_V} \sum_{\theta=1}^{N_\Theta} |MRE_b^{\tilde{p}} - 100 \times \frac{|\bar{p}_{b,u,v,\theta} - \tilde{p}_{b,u,v,\theta}|}{\bar{p}_{b,u,v,\theta}}|, \tag{5.11}$$

and

$$MD_\theta^{\tilde{p}} = \frac{1}{N_B N_U N_V} \sum_{b=1}^{N_B} \sum_{u=1}^{N_U} \sum_{v=1}^{N_V} |MRE_\theta^{\tilde{p}} - 100 \times \frac{|\bar{p}_{b,u,v,\theta} - \tilde{p}_{b,u,v,\theta}|}{\bar{p}_{b,u,v,\theta}}|. \tag{5.12}$$

The latter errors and deviations are presented in figure 5.12, where the left subfigures represent the errors and deviations per energy bin and the right one the errors and deviations per projection angle, and the top ones represent the errors while the bottom ones represent the deviations.

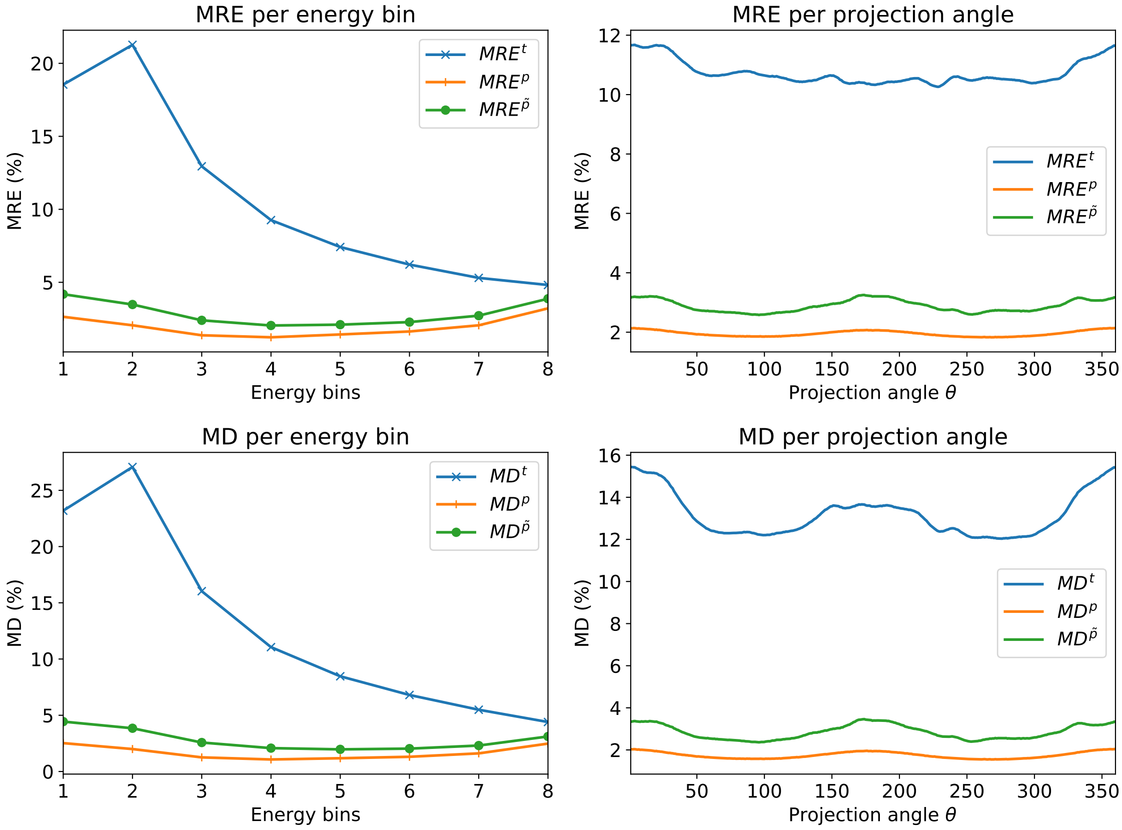

Figure 5.12 – Mean relative error per energy bin (top-left) and per projection angle (top-right) ; Mean deviation per energy bin (bottom-left) and per projection angle (bottom-right)

The attenuation sinograms at each energy bin were then reconstructed with the Reconstruction Toolkit (RTK) [78] using Feldkamp's filtered backprojection algorithm [12]. A CT slice of the reconstructed volumes $\boldsymbol{f}^t$, $\boldsymbol{f}^p$ and $\boldsymbol{f}^{\tilde{p}}$ (obtained with the total, reference primary and estimated one, respectively) is shown on figure 5.13. As in 5.8, the left part of images corresponds to a low energy (bin 2) and the right one to a high energy (bin 6). Profiles of these CT slices are shown in figure 5.14. First row corresponds to the horizontal central profiles and second one to vertical central profiles. Left column is at low energy (bin 2) and right one at high energy (bin 6). In each subfigure, total image is in blue while reference and estimated primary are respectively in orange and green. Finally, two regions of interest (ROI) with a uniform attenuation were selected corresponding to particular biological tissues: the brain (ROI1) and the cranium spongiosa (ROI2) and both their mean values and mean deviations were evaluated. For example, the mean spectra $f_b^{\tilde{p},\mathrm{ROI1}}$ associated with the estimated primary and ROI1 is computed according to the following expression:

$$f_b^{\tilde{p},\mathrm{ROI1}} = \frac{1}{\mathrm{card}(\Omega^1)} \sum_{i \in \Omega^1} f_{b,i}^{\tilde{p}}, \tag{5.13}$$

where Ω^1 represent the set of voxels i corresponding to ROI1. In addition, its corresponding mean deviation $MD^{\tilde{p},\mathrm{ROI1}}$ is computed as:

$$MD_b^{\tilde{p},\mathrm{ROI1}} = \frac{1}{\mathrm{card}(\Omega^1)} \sum_{i \in \Omega^1} |f_b^{\tilde{p},\mathrm{ROI1}} - f_{b,i}^{\tilde{p}}|. \tag{5.14}$$

Figure 5.15 shows the mean spectra of both ROI (top) and the corresponding deviations (bottom).

5.6 Discussion

The scatter correction method proposed in this work has shown impressive performances on the data set simulated with the ICRP realistic anthropomorphic phantom. When comparing the total attenuation projections to the reference and estimated primary ones on figure 5.8, the contrast improvement is remarkable and similar to the one obtained on the reference primary projection images. This is particularly the case at low energy due to the higher SPR in lower energy-bins. The noise increase in estimated primary compared to the reference is significant, in particular at low energy. Regarding the transmission profiles of figure 5.9, one can observe a remarkable fit between reference and estimated primary, even in highly attenuated regions. The primary modulator pattern is clearly visible on the measured transmission curve (blue), unlike the total curve (green). The orange curve, representing the corrected measured transmission also contains the modulator pattern where the attenuation is high but it is not the case anymore in the estimated primary. This illustrates well the basic principle of the method.

The data-fidelity term of our cost function is not based on the scatter map itself, but on the resulting estimated primary. This is the reason why the scatter bias near pixel 130 of the first projection at low energy is lower than the one obtained in 5.4, where the data-fidelity term targeted the reference scatter map. The result is a better fit of the primary curves in this highly attenuated region. At high energy, the scatter bias is significant but the reference and the estimate fit well and the modulator pattern is not clearly visible in the latter. This is due to the combination of two facts. First, at high energy, the mask attenuation is lower that at low energy and the method sensitivity is reduced. Second, the object attenuation is low and a given bias on scatter induces a relatively weaker mask pattern footprint in the estimated primary.

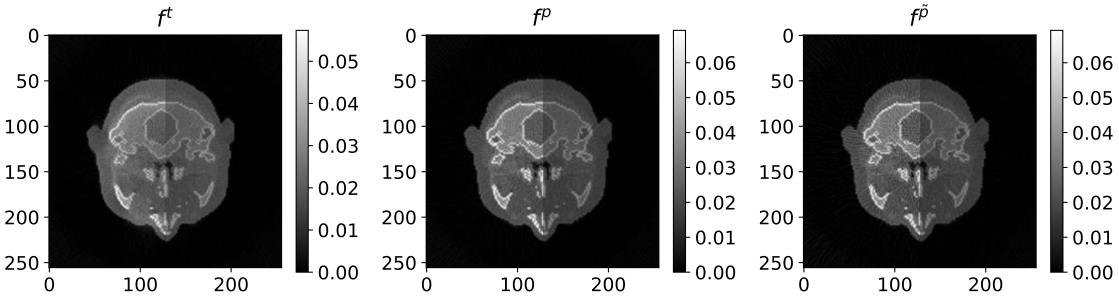

Figure 5.13 – CT slice of total (left), primary (center) and estimated primary (right) attenuation at low energy (LE, bin 2) and high energy (HE, bin 6)

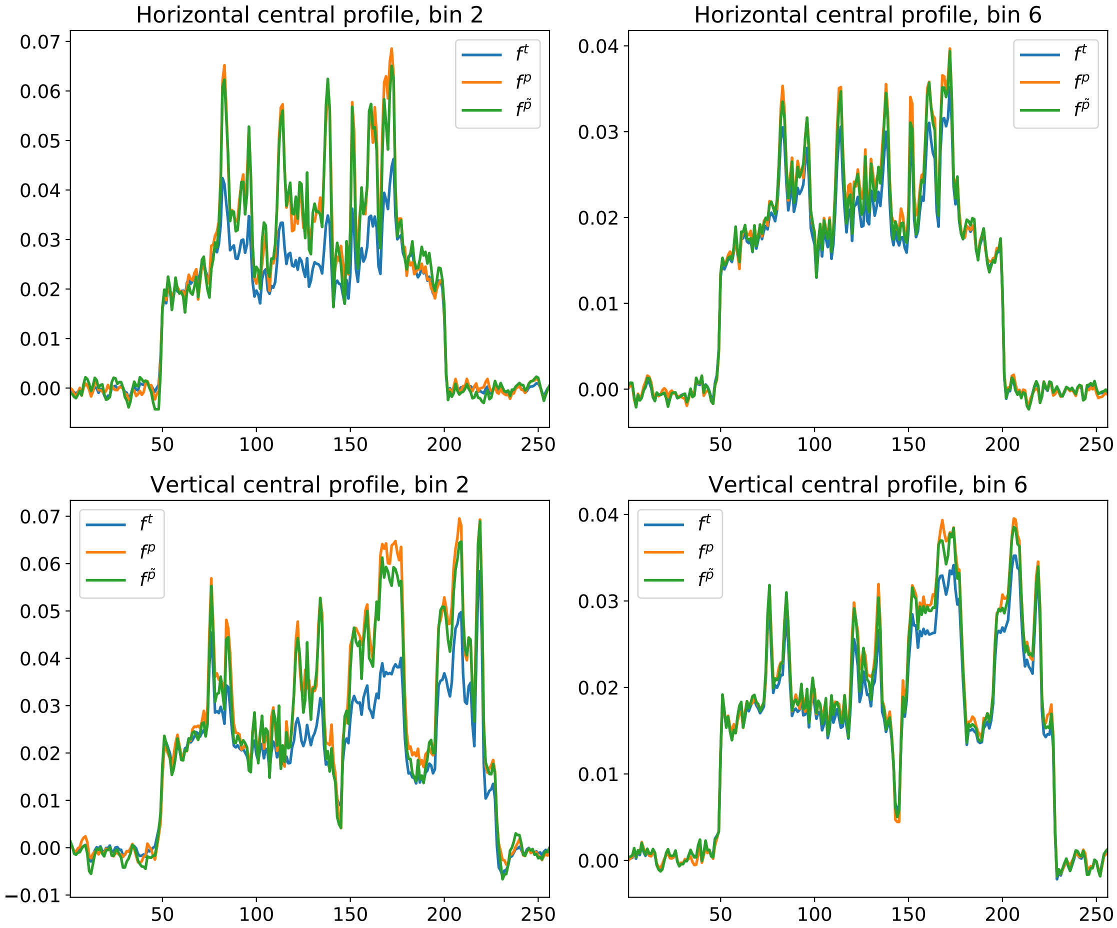

Figure 5.14 – Profiles of the CT slice

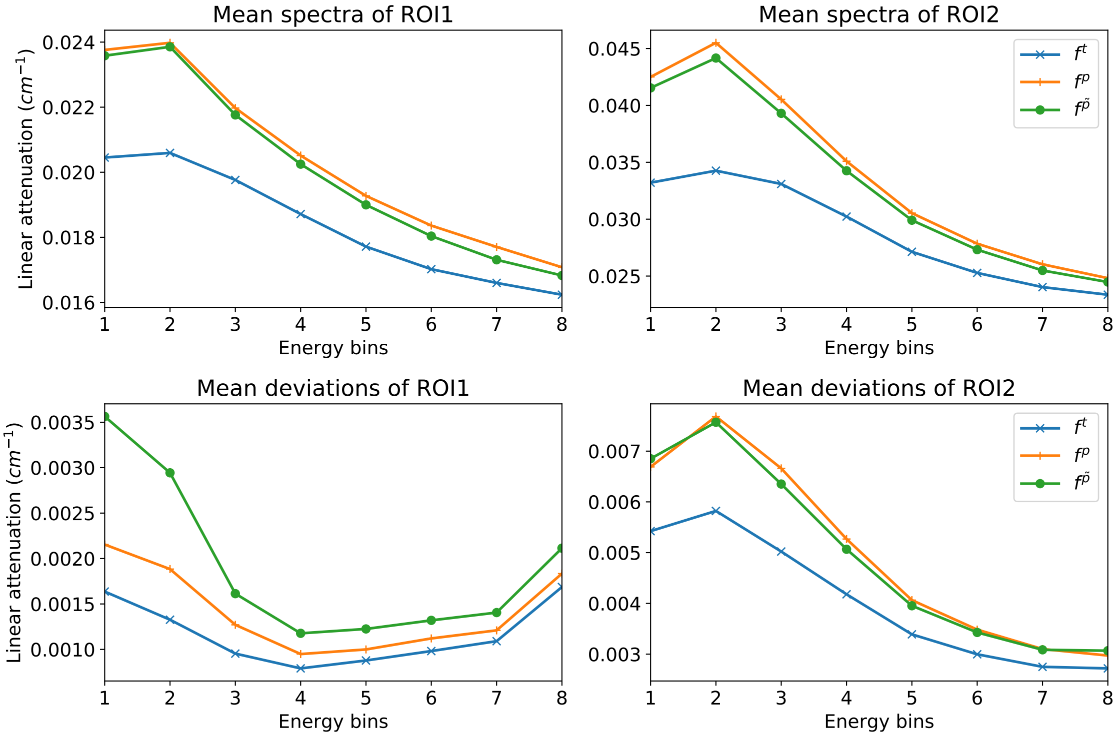

Figure 5.15 – Top: mean spectra of brain (ROI1) and cranium spongiosa (ROI2) ; Bottom: mean deviations of ROI1 and ROI2

Regarding the spectra of pixels of interest of figure 5.10, one can see an impressive fit between reference and estimated primary, even if a weak bias can be seen in the lower energy bins. This is confirmed by the plot of the energy dependent mean relative error (left part of figure 5.12). Indeed, the green curve of estimated primary error is just above the reference primary one (orange curve) representing the statistical noise (which is, as expected, greater at low and high energy because of the fewer detected photons). The right plot, showing the error according to the projection angle, shows that the error is regularly distributed along the θ direction.

The observation of the CT slices of figure 5.13 give the same conclusions as for the projections in terms of contrast improvement and noise degradation. In addition, one can note that the scatter correction method has efficiently removed the cupping artifact without inducing other visible artifacts. The correction of the cupping artifact is more visible in the profiles plotted in figure 5.14. However, these profiles indicate a slight underestimation of the linear attenuation in highly attenuated regions at each energy bin, but also in less attenuated regions at high energy. This is confirmed by the plots of the mean spectra of ROI1 and ROI2 (figure 5.15), the brain (moderately attenuating) having a small bias at high energy and the cranium (more attenuating) a small bias in the whole energy range.

A qualitative analysis of the evolution of the estimated primary shows there is no clearly visible difference between the images from the first iteration. In the same way, this qualitative analysis does not reveal any improvement by using the Charbonnier approximation of ℓ^1 norm compared to the ℓ^2 ones. However, the evolution of the cost function according to the iterations (figure 5.7) shows that the algorithm does not reach convergence at iteration one yet. Indeed, the evolution stops to be perceptible on the cost function only from $n = 2$ iterations. The quantitative analysis of the algorithm convergence is confirmed by the evolution of the mean relative error associated with the estimated primary (blue curve of figure 5.11) which is also almost constant from the second iteration. In addition, the mean relative error associated with the primary estimated using the ℓ^2 norm (green) curve is greater than the one obtained with the Charbonnier approximation of ℓ^1 norm, which highlights the advantage of the use of such functions. Moreover, the high similarity between the blue curves of figures 5.7 and 5.11 indicates that the cost function we designed (equation 4.26) is a good indicator of the presence of scatter in the images.

The method requires to tune some scalar parameters. We already discussed about the tuning of the B-spline spacings (section 5.4). The strengths of the structure weighting and the ℓ^1 norm smoothing are controlled by η and σ respectively. In order to determine their optimal values, we opted for a grid-search and the optimal values were the ones which minimized the difference between the estimated primary maps and the simulated reference ones. As the structure weighting used in this work is exponential (see equation 4.24), small variations of the parameter η induce great variations of dynamics in the weighting matrix $\boldsymbol{W}_2$ and its value has therefore to be tuned quite precisely. On the contrary, the influence of the smoothing parameter σ is not very sensitive and small variations of its value does not clearly affect the results provided by the method.

The tuning of the energy-dependent Tikhonov regularization parameters may also be done with a grid-search. Unfortunately, the non-diagonal behavior of the correction matrix make them interdependent, and a grid-search for these eight parameters would be too time consuming. In order to tackle this issue, we opted for a manual tuning, with again the objective of minimizing the difference between the estimated primary maps and the simulated reference ones. The sensitivity of the method according to these parameters depends on the conditioning of the method which is related to the statistical noise, the mask attenuation, and the ratio between the number of pixels at mask edges and the number of knots in the B-spline scatter model. Indeed, as explained in section 3.3.4, an error $\boldsymbol{\varepsilon} = \boldsymbol{s} - \tilde{\boldsymbol{s}}$ induces an error of $\boldsymbol{C}\boldsymbol{\varepsilon}$ on the estimated primary. It means that the bias $\boldsymbol{\varepsilon}$ can be detected if the bias gradient $\boldsymbol{\nabla}\boldsymbol{C}\boldsymbol{\varepsilon}$ is larger than the gradient of the statistical noise and the weight associated with a given B-spline knot can be estimated precisely if the mask attenuation and the number of edge pixels in the area of this knot are large enough. In the simulation case presented in this chapter, the choice of the Tikhonov parameters had a significant impact on the results, such as the primary images were biased with wrongly chosen parameters. This regularization can be seen as a prior information on the imaged object, and it increases considerably the object dependency of the method.

5.7 Conclusion

In this chapter, we have evaluated the proposed method on realistic simulated data. The correction matrix was able to correctly compensate for the mask attenuation, in particular with a number of energy bins comprised between two and twelve and with a primary modulator mask made of graphite. The mean relative error induced by a 5 mm thick graphite mask in the case of a photon counting detector with 8 energy bins was only around 0.03%. We have shown that a scatter model based on B-splines functions enables an acceptable representation of scatter with a very few parameters and the corresponding primary maps are very accurate. For the evaluation of the full chain method, we used second order B-splines and spacings of 128 pixels in the two directions of the detector and 15° in the angular direction of the projections. This particular model induced a mean relative error of 0.5% on the estimated primary. Finally, the evaluation of the proposed method has shown very good results both in the projection and the object domains in terms of scatter correction. The contrast has been well improved and the scatter induced cupping artifact has been removed, without inducing new visible artifacts. The spectra of three pixels and two regions of interest have shown that the results are correct even in the energy domain. From an initial mean error of 10.7%, we were able to lower it to 2.88%, which is close to the error caused by statistical noise. However, we pointed out the difficulty to tune the energy-dependent regularization parameters. The next chapter will be dedicated to the evaluation of the method on experimental images.

6

Evaluation of the method on experimental data

6.1 Introduction

The scatter correction method presented in chapter 4 has been successfully validated on a simulated data set in chapter 5. The objective of the following chapter is to test the proposed method on experimental images of two distinct phantoms acquired with a commercial spectral photon counting detector. We present the experimental setup in section 6.2. The correction matrix is then tested in section 6.3 and the optimal B-spline spacings are evaluated in section 6.4. Finally, the results obtained with the method are registered in section 6.5 and discussed in section 6.6.

6.2 Experimental set-up

The physical experiments were performed using a parallel fan-beam set-up, shown in figure 6.1. The system is made of a tungsten x-ray source, powered with 120 kV. The imaged object is placed on a vertical translation table (allowing us to acquire several slices).

The detector is a line-detector composed of 5 commercial detectors ME100 (Detection Technology) for a total of 640 pixels with a pitch of 0.8 mm. The ME100 has 64 energy-bins of about 2 keV width, which are binned into $N_B = 8$ energy-bins. The energy range of each energy bin of the detector is presented in table 6.1. The five ME100s are arranged side by side with a gap of around 1.6 mm between each other. We have therefore two missing pixels between two ME100 which are linearly interpolated resulting in a detector with $N_U = 640 + 2 \times 4 = 648$ pixels. In addition, some pixels failed during the acquisitions, and are also linearly interpolated.

The primary modulator mask is a 5 mm thick graphite slab drilled with 3 mm diameter holes each 5 mm. The support of the mask is attached to the translation

Figure 6.1 – Picture of the parallel-beam experimental set-up

Bin index	Energy range (keV)
1	30.8 – 41.8
2	41.8 – 52.8
3	52.8 – 63.8
4	63.8 – 74.8
5	74.8 – 85.8
6	85.8 – 96.8
7	96.8 – 107.8
8	107.8 – 121

Table 6.1 – Relation between energy-bin and photon energy in physical experiments

table in order to mimic a cone-beam case. The pattern was designed with the support of the manufacturer, with the objective of having as many holes as possible, and the holes being as small as possible. Pictures of the mask can be found in figure 6.2: a general view on the left and a zoom on the geometry details on the right.

We imaged two phantoms. The first one is the CIRS phantom model 062M, a 33×27 cm^2 water-equivalent ellipsoid with tissue-equivalent plastic inserts of 3 cm diameter. A picture of this phantom is presented in figure 6.3.

The second phantom is a realistic human head phantom: the RANDO phantom. It is made with a real human skull (from a dead body), resin and air. Figure 6.4 shows a picture of this phantom.

The image without object $\boldsymbol{p}^0$ and the mask image $\hat{\boldsymbol{p}}^0$ were acquired with 20 mAs while the 180 projections of the tomographic acquisitions of the phantoms (with $N_V = 16$) were acquired with 2 mAs. For each phantom, three CT-scans were ac-

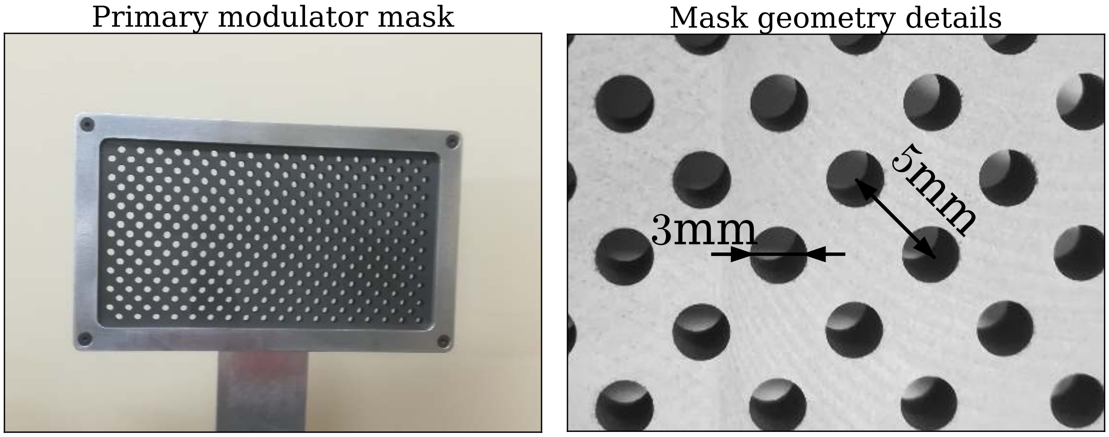

Figure 6.2 – Pictures of the primary modulator mask: general view (left) and details (right)

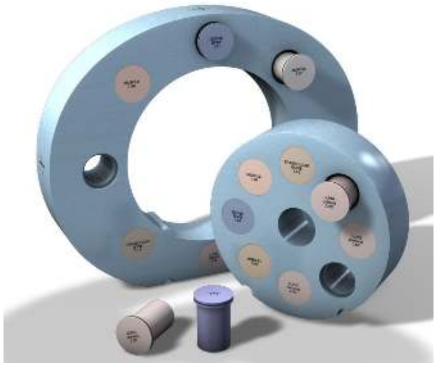

Figure 6.3 – Picture of the CIRS phantom

Figure 6.4 – Picture of the RANDO phantom

quired: two with only the collimation of the detector (with and without the primary modulator mask, giving respectively $\hat{\boldsymbol{t}}$ and $\boldsymbol{t}$) and a third without mask and with two additive collimators (one placed at the level of the source and another just before the object). The latter acquisition is considered as a scatter-free reference acquisition $\boldsymbol{p}$ for the rest of the study.

Figure 6.5 shows a white image (without object nor mask) before interpolation between the ME100s (top) and the mean relative difference $\boldsymbol{MRD}$ between two white images $\boldsymbol{p}^{0,1}$ and $\boldsymbol{p}^{0,2}$ acquired in the same conditions but with an interval of about one minute (bottom). The latter is computed as follows:

$$MRD_u = 100 \times \frac{1}{N_B} \sum_{b=1}^{N_B} \frac{|p_{b,u}^{0,1} - p_{b,u}^{0,2}|}{p_{b,u}^{0,1}}. \tag{6.1}$$

6.3 Correction matrix evaluation

Calibration dataset In addition, calibration images with 20 mAs were acquired to estimate $\boldsymbol{C}$, using slabs of polypropylene (PP) and aluminum (Al) with varying thicknesses. The various combinations of PP and Al in the $N^{\text{cal}} = 10$ calibration acquisitions are registered in table 6.2.

Acquisition index	l^{PP} (mm)	l^{Al} (mm)
1	0	0
2	50	0
3	100	0
4	150	0
5	50	6
6	100	6
7	150	6
8	50	10
9	100	10
10	150	10

Table 6.2 – Combinations of polypropylene (PP) and aluminum (Al) slabs thicknesses used for the calibration acquisition

Results The correction matrix was estimated using the previously described dataset. In order to evaluate its ability to compensate for the mask attenuation, we have tested it on the calibration database. For a quantitative evaluation of the correction matrix

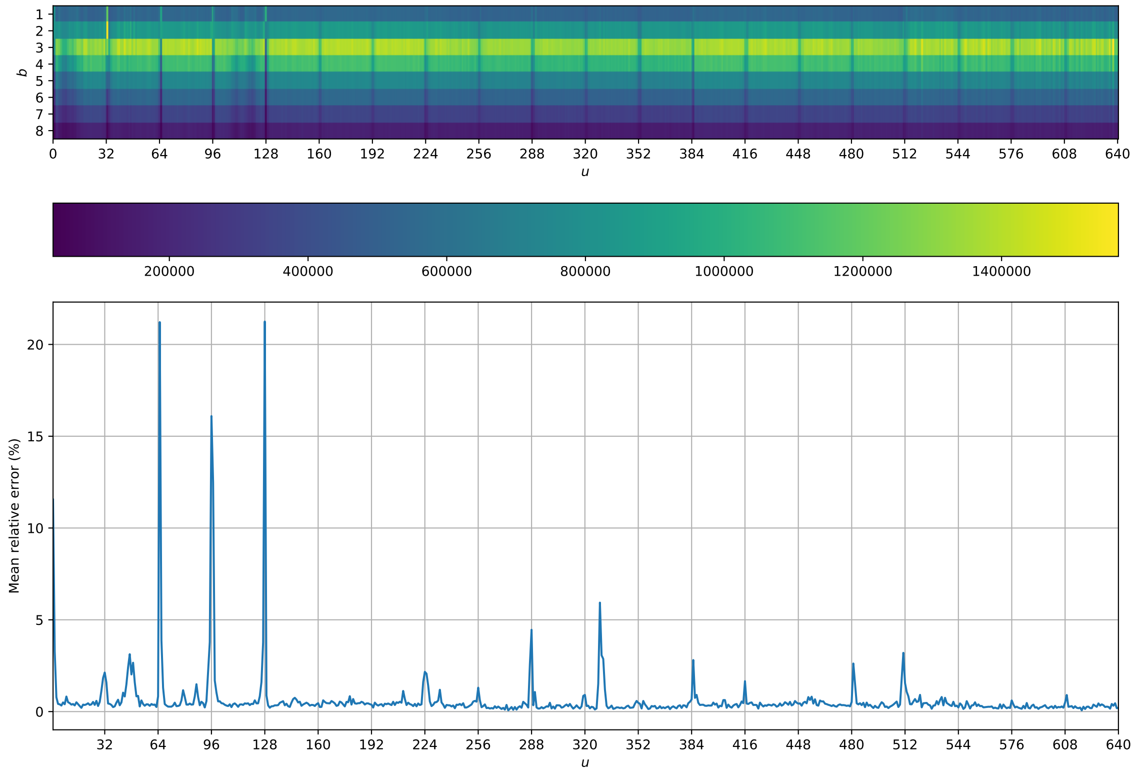

Figure 6.5 – White image before interpolation (top) and mean relative difference between two white images acquired one minute apart (bottom).

performance, we opted for the mean relative error per energy bin MRE_b and mean relative error per calibration acquisition MRE_k. Their expressions are given by:

$$MRE_b = 100 \times \frac{1}{N_U N_V N^{\text{cal}}} \sum_{u=1}^{N_U} \sum_{v=1}^{N_V} \sum_{k=1}^{N^{\text{cal}}} \frac{|p_{k,b,u,v} - \boldsymbol{c}_{b,u,v}^T \hat{\boldsymbol{p}}_{k,u,v}|}{p_{k,b,u,v}}, \tag{6.2}$$

and:

$$MRE_k = 100 \times \frac{1}{N_B N_U N_V} \sum_{b=1}^{N_B} \sum_{u=1}^{N_U} \sum_{v=1}^{N_V} \frac{|p_{k,b,u,v} - \boldsymbol{c}_{b,u,v}^T \hat{\boldsymbol{p}}_{k,u,v}|}{p_{k,b,u,v}}. \tag{6.3}$$

Again, we use the mean error deviations to evaluate the error dispersion. They are computed as follows:

$$MD_b = \frac{1}{N_U N_V N^{\text{cal}}} \sum_{u=1}^{N_U} \sum_{v=1}^{N_V} \sum_{k=1}^{N^{\text{cal}}} |MRE_b - 100 \times \frac{|p_{k,b,u,v} - \boldsymbol{c}_{b,u,v}^T \hat{\boldsymbol{p}}_{k,u,v}|}{p_{k,b,u,v}}|, \tag{6.4}$$

and:

$$MD_k = \frac{1}{N_B N_U N_V} \sum_{b=1}^{N_B} \sum_{u=1}^{N_U} \sum_{v=1}^{N_V} |MRE_k - 100 \times \frac{|p_{k,b,u,v} - \boldsymbol{c}_{b,u,v}^T \hat{\boldsymbol{p}}_{k,u,v}|}{p_{k,b,u,v}}|. \tag{6.5}$$

Table 6.3 presents the errors and deviations associated with the eight energy bins and table 6.4 presents the ones associated with the ten calibration acquisitions.

Bin index	MRE_b (%)	MD_b (%)
1	0.84	0.54
2	1.4	0.87
3	0.79	0.48
4	0.63	0.40
5	0.60	0.38
6	0.60	0.38
7	0.68	0.42
8	0.91	0.57

Table 6.3 – Mean relative error of the correction matrix per energy bin and the corresponding mean deviation

Acquisition index	MRE_k (%)	MD_k (%)
1	0.67	0.40
2	0.48	0.29
3	0.46	0.29
4	0.73	0.47
5	0.93	0.55
6	0.67	0.39
7	0.92	0.59
8	1.01	0.61
9	1.05	0.64
10	1.12	0.75

Table 6.4 – Mean relative error of the correction matrix per calibration acquisition and the corresponding mean deviation

Discussion The correction matrix accuracy was successfully demonstrated through its evaluation on the calibration database. The associated mean relative error remains below 1.5 % at each energy bin (table 6.3), like the simulation case. Regarding the error associated with the calibration acquisition (table 6.4), one can say that the compensation for the mask attenuation is effective in the whole attenuation range.

However, an exposure of 20 mAs was not sufficient for sufficiently reducing the statistical noise in attenuated acquisitions, in particular in low and high energy bins in which fewer photons are detected compared to the medium ones. Moreover, even with collimation, residual scatter may be detected (mostly at low energy). These issues may explain the larger error observed in the experimental case than in the simulation one. In particular, the error increase at high energy can be linked with the statistical noise as well as the error increase at high attenuation, while the error increase at low energy may be caused by the combination of greater statistical noise, greater SPR and greater beam-hardening (which was the only cause of error in the simulation case).

6.4 B-spline spacings selection

Estimation of the model parameters Before running the method, it is necessary to choose the B-spline spacings. As we made only $N_V = 16$ fan-beam acquisitions, scatter is almost constant in this direction, which is confirmed by the fact that at fixed energy bin and projection angle, no variation can be seen on the total images along the v-direction. We chose therefore to force the estimated scatter to be constant in this direction. The angular spacings were set to $\delta_\theta = 10^\circ$ for implementation convenience which is reasonable according to the simulated results and the literature about scatter behavior (see 2.3). Unlike the v-direction, the B-spline spacing in the u-direction impacts the method. In order to select the B-spline spacings δ_u adapted to the experimental cases, we performed a first estimation $\tilde{\boldsymbol{s}}$ of the scatter maps by using the total sinogram $\boldsymbol{t}$ and the reference primary one $\boldsymbol{p}$, and to compare the resulting estimated primary $\tilde{\boldsymbol{p}}$ with the measured one $\boldsymbol{p}$. The scatter map is first estimated as follows:

$$\tilde{\boldsymbol{x}} = \underset{\boldsymbol{x} \in \mathbb{R}^{N_B N_K}}{\arg\min} \|\boldsymbol{p} - (\boldsymbol{t} - \boldsymbol{B}\boldsymbol{x})\|_2^2, \tag{6.6}$$

and the estimated primary is recovered with $\tilde{\boldsymbol{p}} = \boldsymbol{t} - \boldsymbol{B}\tilde{\boldsymbol{x}}$.

Results In this study, we present the cases $\delta_u = 128$ and $\delta_u = 256$ pixels for the RANDO and $\delta_u = 64$ and $\delta_u = 128$ for the CIRS. Attenuation profiles of a projection are shown in figure 6.6, where the blue curves represent the total attenuation, the orange ones the reference primary acquisition and the green and red ones the estimated primary obtained with the two distinct spacings.

Discussion Regarding the attenuation profiles of figure 6.6, it is clear that the B-spline spacing in the u-direction has an influence on the ability to recover an acceptable primary map. Indeed, for the RANDO case, a spacing of $\delta_u = 256$ induces an overestimation of the primary at the edges of the object, and an underestimation near

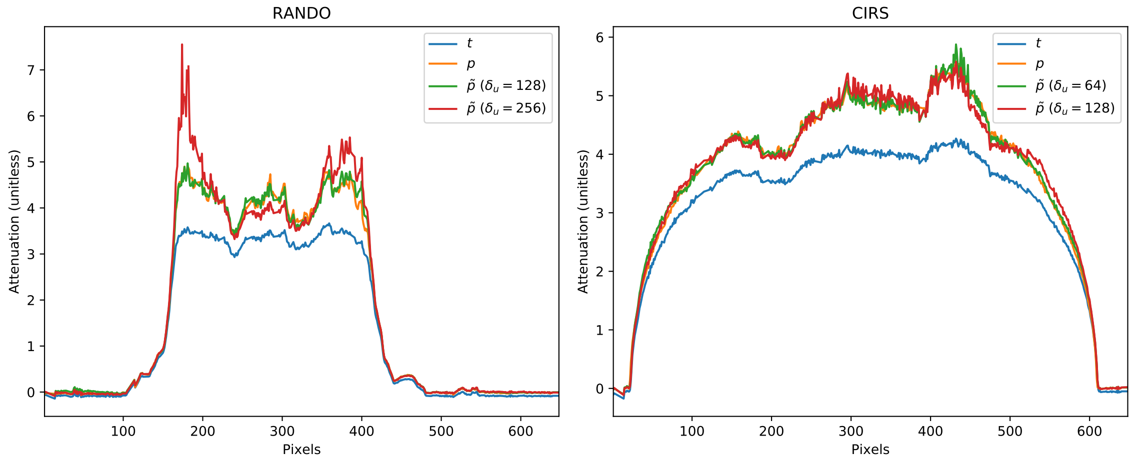

Figure 6.6 – Attenuation profiles of total, reference primary and estimated primary with various spacings (left: RANDO, right: CIRS)

its center. However, the curve corresponding to $\delta_u = 128$ pixels fits well with the reference primary. The CIRS case requires a smaller spacing as the primary curve fits, on the right part, only with the estimated primary obtained with $\delta_u = 64$ pixels. The necessity to set more knots in the CIRS case is consistent with our knowledge about scatter behavior, which displays more spatial variations with the object attenuation. It is indeed on the most attenuated part of the CIRS profile that the curve of estimated primary with $\delta_u = 128$ does not fit with the reference primary one.

6.5 Results

The method has been tested on the experimental datasets, with the parameters registered in table 6.5.

After scatter correction, some values of the estimated primary are negative (in the most attenuated regions), which has no physical meaning. We replace those values by the median value of the neighbors pixels. In addition, a median filter is applied on each projection at each energy bin.

An attenuation projection of the RANDO scan is shown in figure 6.7, where the left part represents energy bin 2 and the right one energy bin 6. The top, center and bottom images refer to the total attenuation, the reference primary and the estimated primary, respectively. The corresponding central profiles are plotted in figure 6.8, the blue curves representing the total attenuation, the orange ones the reference primary and the green ones the estimated primary. An attenuation sinogram is also shown in figure 6.9. Total, reference and estimated primary are respectively on the left, in the

Parameter	CIRS	RANDO
η	1×10^{1}	1×10^{1}
σ	1×10^{-4}	1×10^{-4}
τ_1	1×10^{-6}	1×10^{-6}
τ_2	1×10^{-5}	6×10^{-7}
τ_3	4×10^{-5}	4×10^{-7}
τ_4	7×10^{-5}	2×10^{-7}
τ_5	8×10^{-5}	8×10^{-8}
τ_6	2×10^{-4}	6×10^{-8}
τ_7	5×10^{-4}	2×10^{-8}
τ_8	5×10^{-4}	1×10^{-8}
δ_u	64 pixels	128 pixels
δ_v	64 pixels	128 pixels
δ_θ	10°	10°

Table 6.5 – Scalar parameters for the CIRS and RANDO test cases

center and on the right. Again, the left parts represent energy bin 2 and the right ones energy bin 6.

As for the RANDO case, a projection of the CIRS acquisition is shown in figure 6.10 and the corresponding central profiles in figure 6.11. Sinograms are presented in figure 6.12.

Three pixels of interest (POI) have been isolated in each of the cases and their spectra are shown in figures 6.13 (RANDO) and 6.14 (CIRS). For both cases, the selected pixels have growing attenuation to cover almost the whole attenuation range of the datasets. The blue curves represent the total spectra, the orange ones the reference primary and the green ones the estimated primary.

The attenuation sinograms at each energy bin were then reconstructed with the Reconstruction Toolkit (RTK) [78] using the fan-beam filtered backprojection algorithm.

A CT slice of the RANDO head is shown in figure 6.15, corresponding to total (left), reference (center) and estimated primary (right). The corresponding profiles are presented in figure 6.16, where the blue, orange and green curves represent respectively the total, reference and estimated primary reconstructed volumes. The left column represents energy bin 2 and he right one energy bin 6. The vertical profiles (top) correspond to voxel index 163 and the horizontal ones (bottom) to voxel index 127.

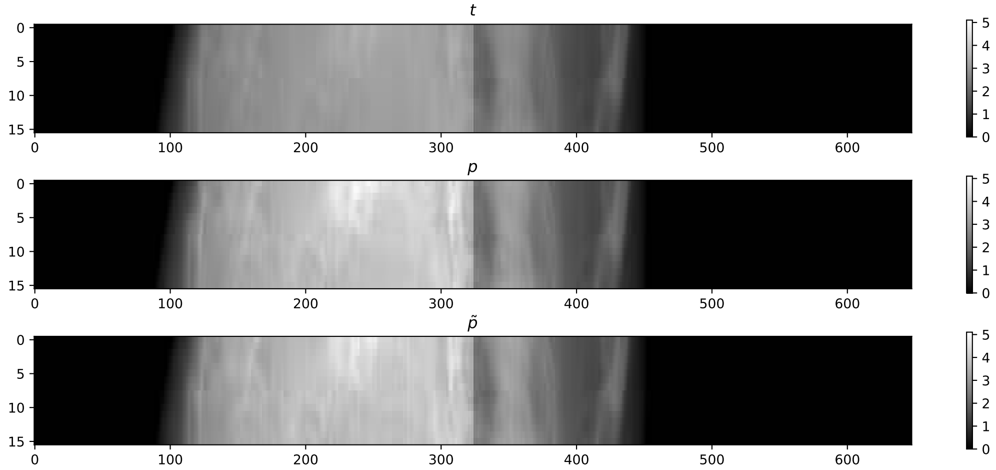

Figure 6.7 – Attenuation projection of the RANDO case: total (top), reference primary (center) and estimated primary (bottom) at two energy bins (left: bin 2, right: bin 6)

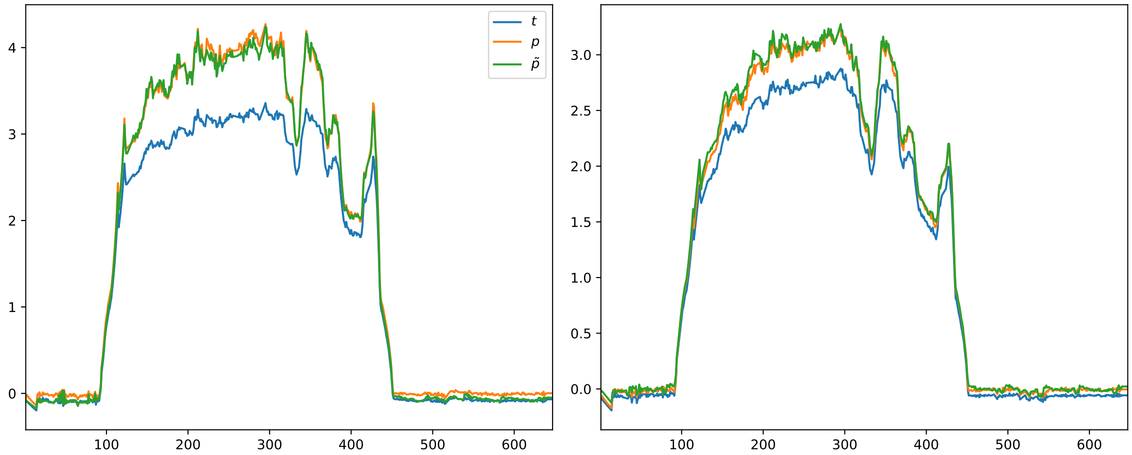

Figure 6.8 – Attenuation profiles of the RANDO case: total, reference primary and estimated primary at energy bins 2 (left) and 6 (right)

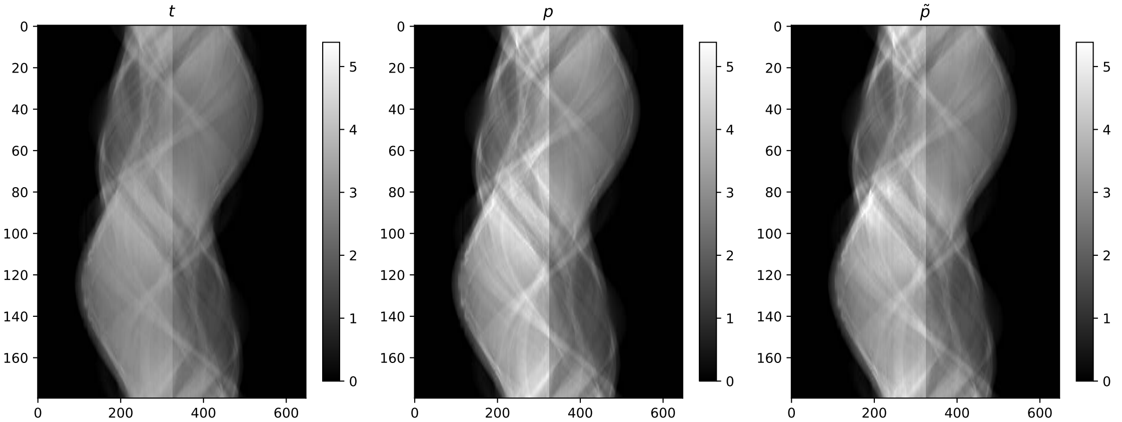

Figure 6.9 – Attenuation sinograms of the RANDO case: total (left), reference primary (center) and estimated primary (right) at two energy bins (left: bin 2, right: bin 6)

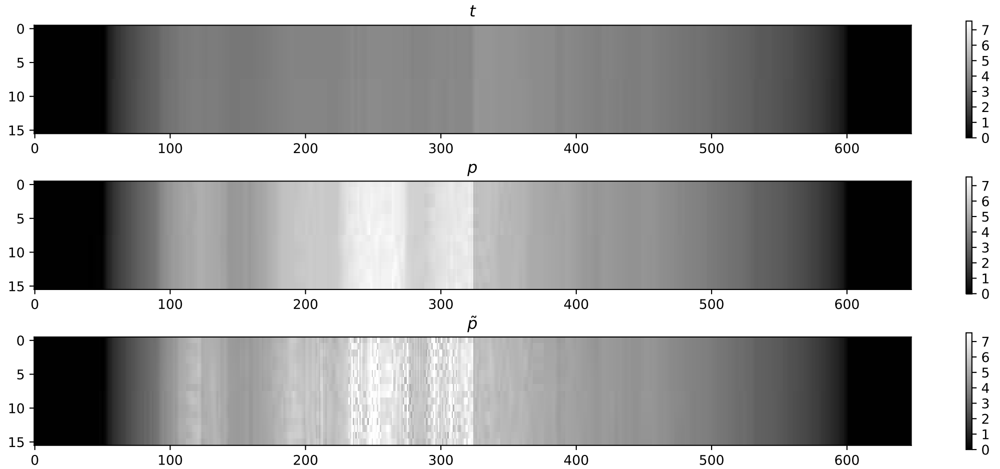

Figure 6.10 – Attenuation projection of the CIRS case: total (top), reference primary (center) and estimated primary (bottom) at two energy bins (left: bin 3, right: bin 5)

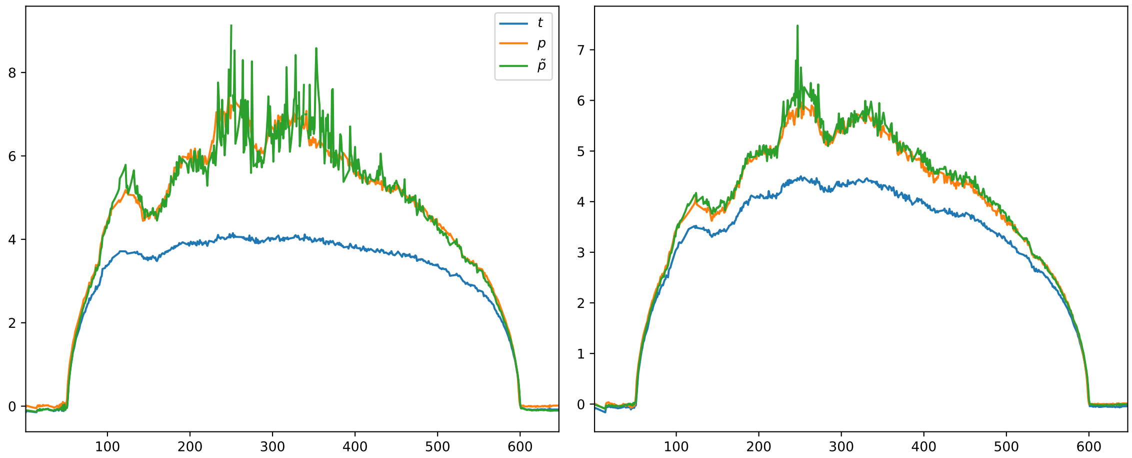

Figure 6.11 – Attenuation profiles of the CIRS case: total, reference primary and estimated primary at energy bins 2 (left) and 6 (right)

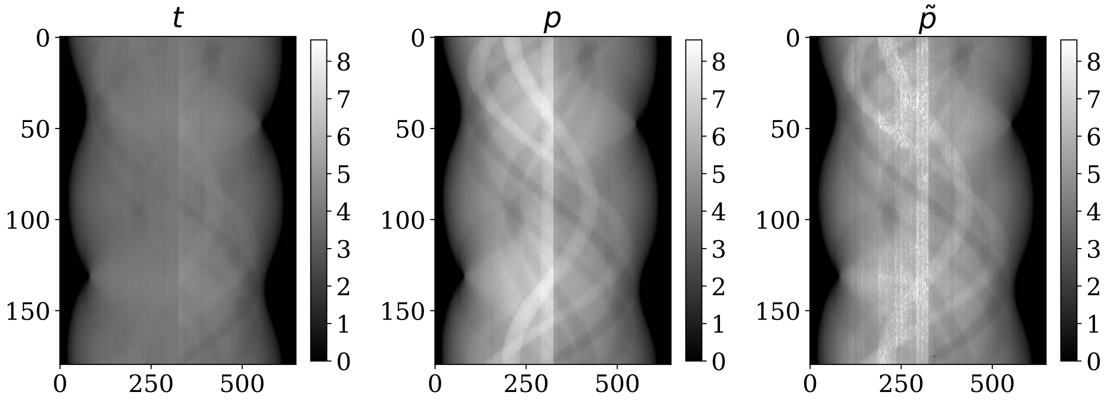

Figure 6.12 – Attenuation sinograms of the CIRS case: total (left), reference primary (center) and estimated primary (right) at two energy bins (left: bin 2, right: bin 6)

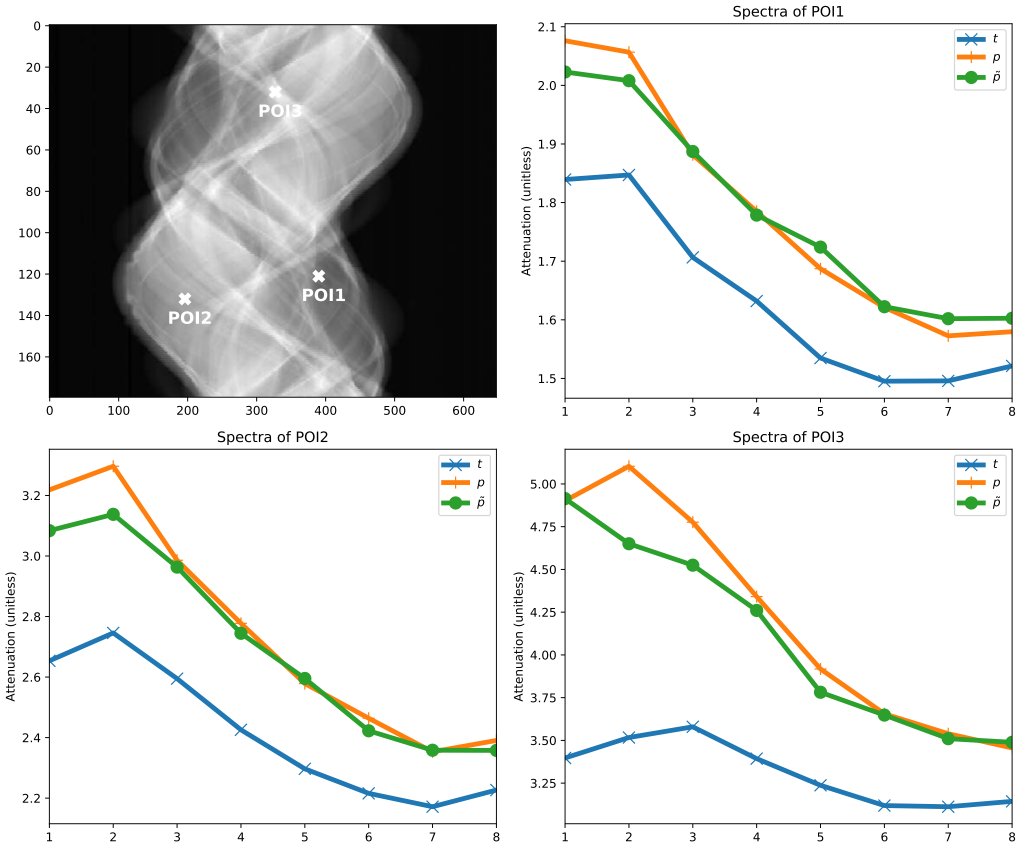

Figure 6.13 – Attenuation spectra of total, reference primary and estimated primary for different pixels of interest (POI) in the RANDO case.

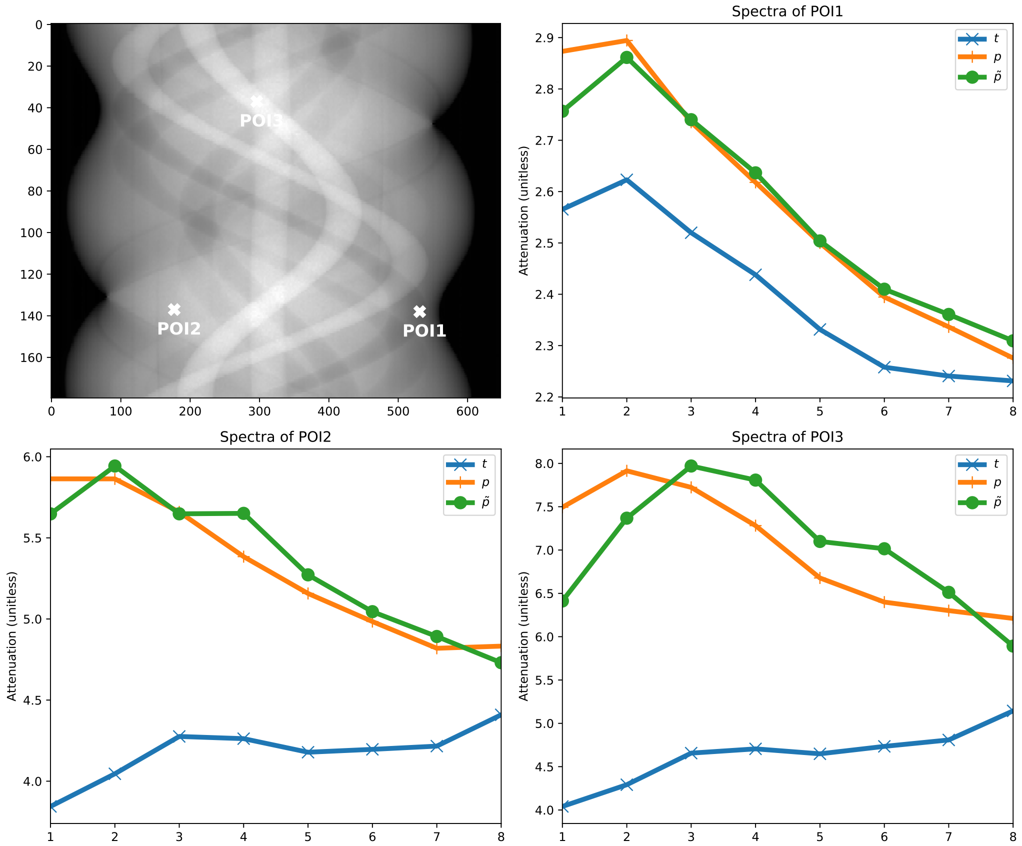

Figure 6.14 – Attenuation spectra of total, reference primary and estimated primary for different pixels of interest (POI) in the CIRS case.

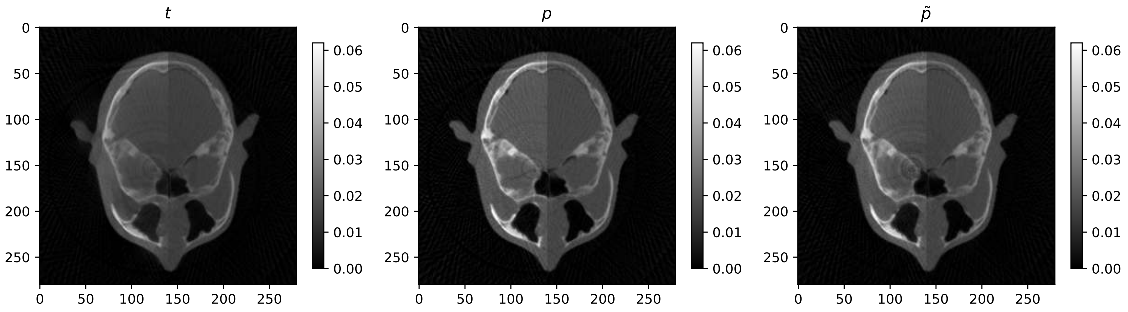

Figure 6.15 – CT slice of the RANDO head. Left: total, center: reference primary and right: estimated primary. Left parts of images: energy bin 2, right parts: energy bin 6.

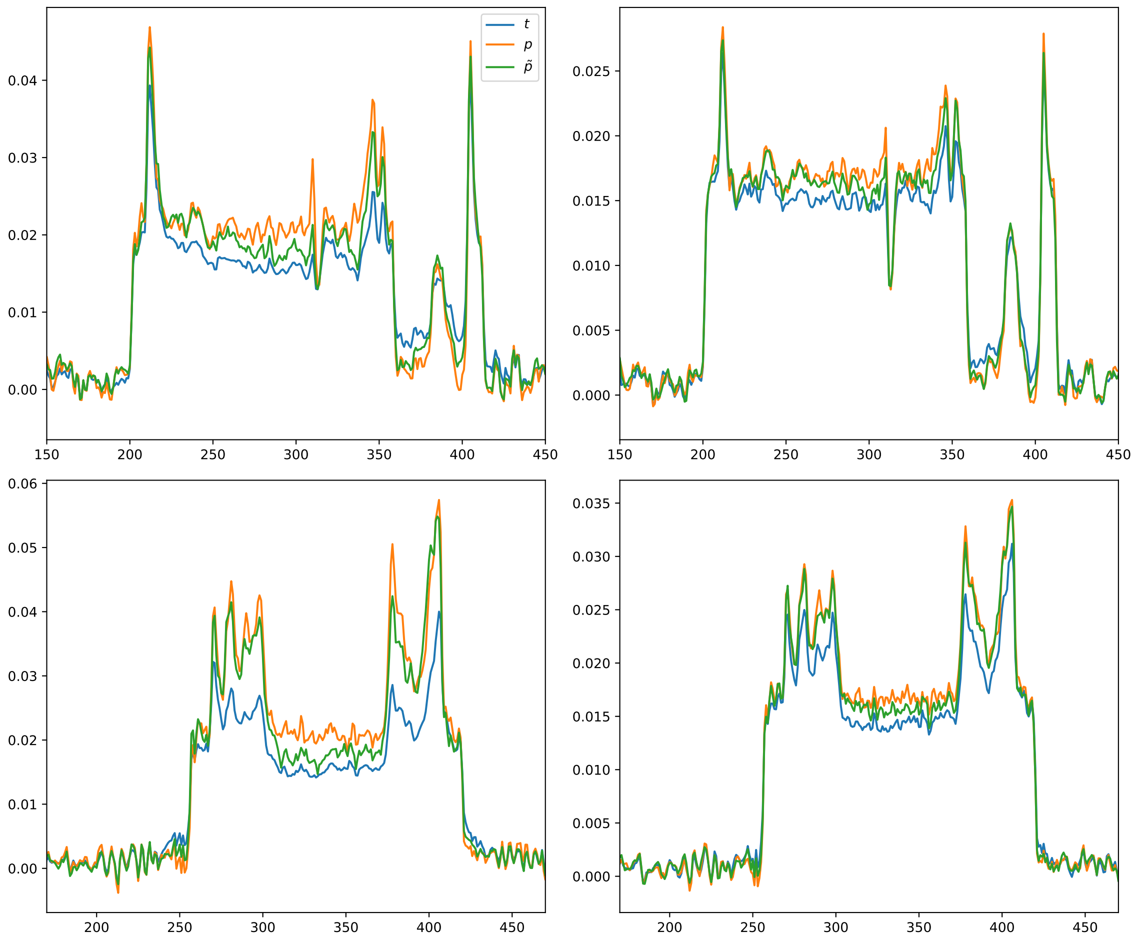

Figure 6.16 – Profiles of the RANDO CT slice (top: vertical profile (column index 163), bottom: horizontal profiles (row index 127); left: energy bin 2, right: energy-bin 6)

In the same way, figures 6.17 and 6.18 show a CT slice of the CIRS phantom and two profiles: a vertical one corresponding to voxel index 223 (top) and an horizontal one corresponding to voxel index 148 (bottom). Again, left subfigures represent energy bin 2 and right ones energy bin 6.

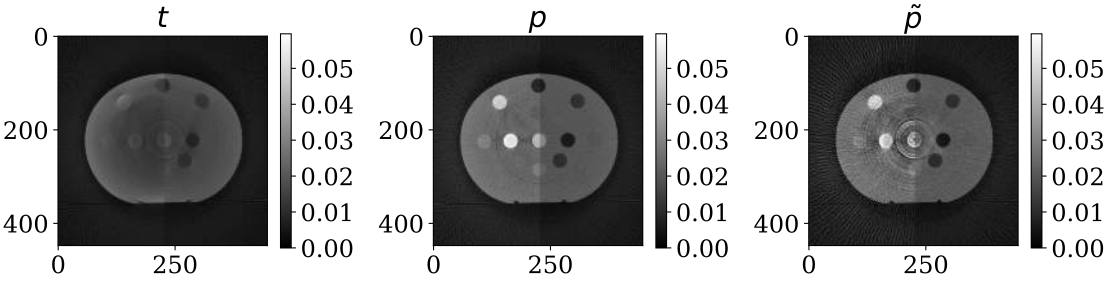

Figure 6.17 – CT slice of the CIRS phantom. Left: total, center: reference primary and right: estimated primary. Left parts of images: energy bin 2, right parts: energy bin 6.

The background ellipsoid of the CIRS phantom and the seventeen inserts were segmented resulting in eighteen regions of interest (ROI), which positions are shown in figure 6.19. The mean spectra and mean deviations (calculated according to equations 5.13 and 5.14) of regions of interest 8 and 9 are shown in figure 6.20. The mean spectra of each ROI are presented in appendix C.

6.6 Discussion

Projection images of figures 6.7 and 6.10, as well as attenuation sinograms of figures 6.9 and 6.12 show an impressive increase of contrast in the projection domain due to the proposed method. This is particularly obvious on the sinogram of the CIRS phantom at low energy (where the SPR is the largest): almost no structure can be distinguished in the scatter corrupted total image. On the contrary, the internal structures caused by the inserts are equally visible in the reference and estimated sinograms. The observation of the attenuation profiles of figures 6.8 and 6.11 confirms that the estimated primary fits well with the reference primary. In addition, one can remark a significant increase of statistical noise. This is particularly visible at low energy and high attenuation. The total sinogram contains the noises associated with both the primary and the scattered radiations. When we subtract the scatter estimate from the total sinogram, we obtain the estimated primary which still contains both noises, unlike the reference primary. As a result, the signal-to-noise ratio (SNR) of a pure primary image is expected to be greater than the one of a primary estimated from a scatter corrupted sinogram. Furthermore, the effect is exacerbated by the presence of the primary modulator mask, which lowers the primary levels and therefore

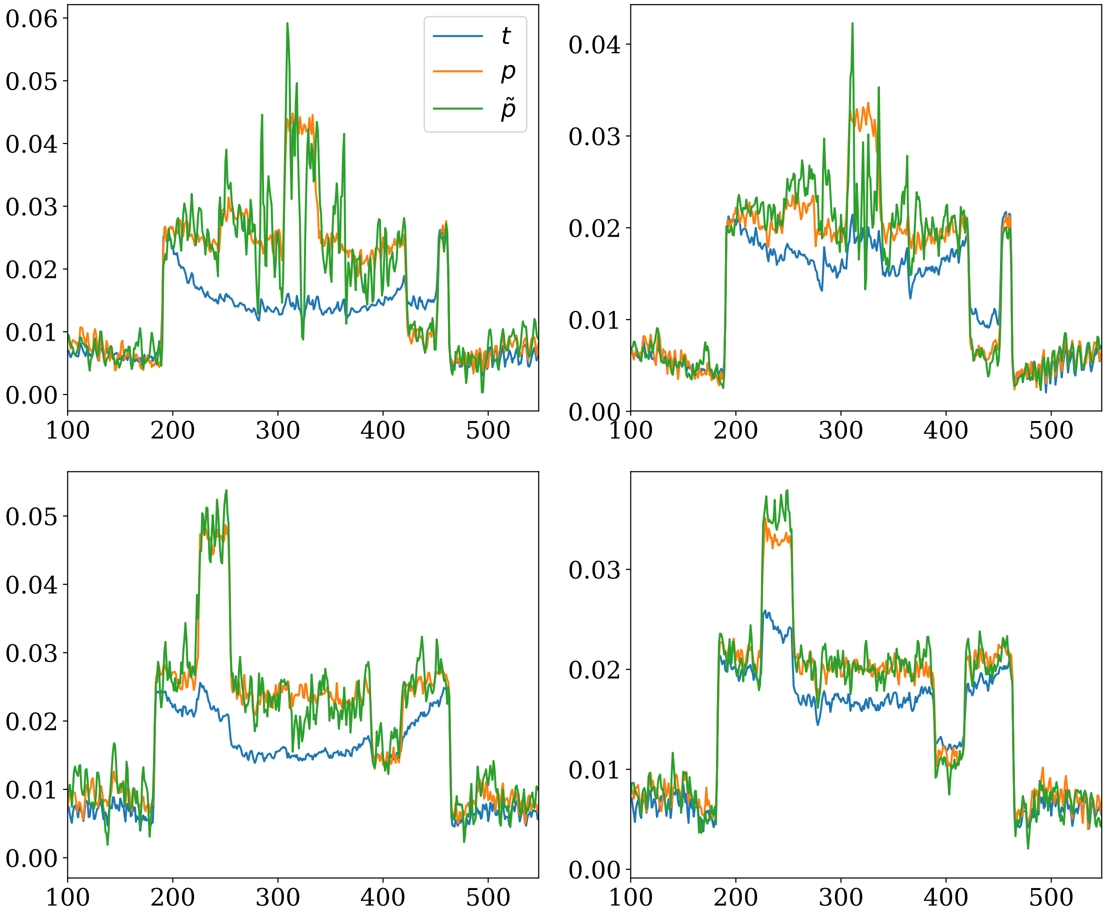

Figure 6.18 – Profiles of the CIRS CT slice (top: vertical profile (column index 223), bottom: horizontal profiles (row index 148); left: energy bin 2, right: energy-bin 6)

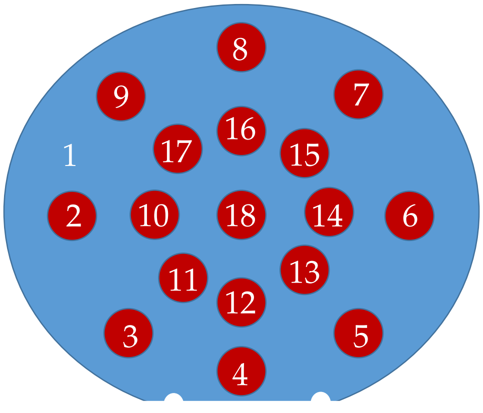

Figure 6.19 – Regions of interest locations in the CIRS phantom

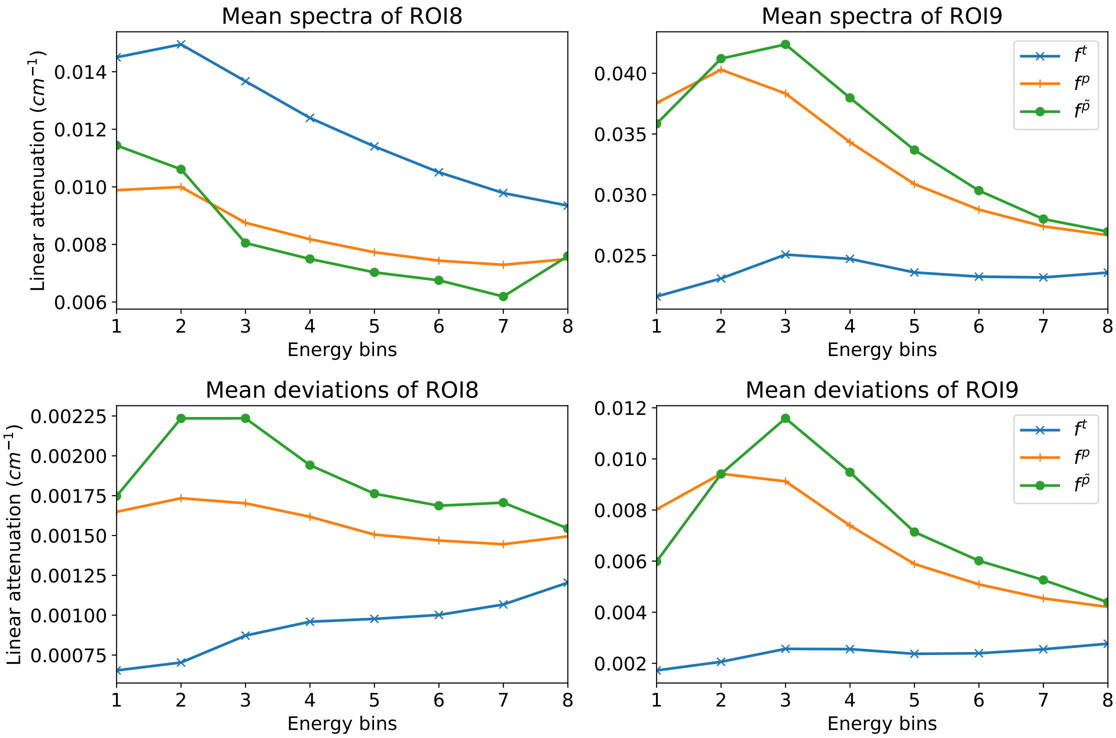

Figure 6.20 – Top: mean spectra of ROI8 and ROI9 ; Bottom: mean deviations of ROI8 and ROI9

decreases the SNR of the total sinogram. It is also worth noting that the sinograms display strong vertical stripes, in particular in total and estimated primary images. We could not find a satisfying explanation for this behavior.

The spectra of pixels of interest in figures 6.13 and 6.14 show the accuracy of the method in the energy domain. Indeed, the estimated primary fits very well with the reference at low and medium attenuation. However, the spectra of highly attenuated pixels (POI3 of the RANDO dataset and POI2 and POI3 of the CIRS one) reveal a significant bias which is caused in part by statistical noise.

The contrast enhancement allowed by the method is confirmed by the observation of the CT slices of figures 6.15 and 6.17. In particular, every insert of the CIRS phantom can be detected in scatter corrected images, unlike in scatter corrupted ones, where the inserts which attenuation is close to the ellipsoid background cannot be distinguished. Strong ring artifacts are present in the total and estimated primary images corresponding to the vertical stripes observed in the sinograms. Shading artifacts are also present in the estimated primary slice of the CIRS case, between highly attenuating inserts. However, they are also visible into the reference primary. It means that they are induced by the beam-hardening or that there is residual scatter in the reference primary.

The profiles of figures 6.16 and 6.18 indicate a good quantitative accuracy of the method, except in the region of the rotation center. In addition, the cupping artifact, significant in the total images of the CIRS case, was correctly removed.

The mean spectra of the eighteen regions of interest show a good quantitative accuracy in the energy domain, even in highly attenuated inserts (e.g. regions of interest 9 and 10) and weakly attenuated ones (e.g. regions of interest 8 and 14). However, the mean spectra of the estimated primary of the central insert (ROI 18) does not fit with the reference primary one. This can be linked to the strong ring artifacts in this region.

As for the simulation case, we tuned the scalar parameters η (defined in equation 4.24) and σ (defined in equation 4.27) with a grid search (with the objective of minimizing the norm of the difference between the reference and estimated primary), and the regularization parameters τ_b (defined in the diagonal matrix $\boldsymbol{T}$ in equation 4.26) manually (with the same objective). Again, the impact of the regularization parameters were significant, in particular for the CIRS case. Because of its great SPR, a small variation on the scatter map induces a great one on the estimate primary image.

6.7 Conclusion

We have seen in section 6.2 that some pixels of the ME100 detector suffer from instability. However, we successfully validated the correction matrix in section 6.3. We have then evaluated the optimal B-spline spacings for each of the two imaged phantoms in section 6.4, and concluded that angular spacings of 10° were optimal for both cases, while u-direction spacings of 128 and 64 pixels were the best choice for the RANDO and the CIRS phantoms respectively. The evaluation of the whole method on these datasets in section 6.5 have shown very good results in terms of contrast enhancement and cupping artifact removal. In particular for the CIRS case, where the scatter to primary ratio was particularly high. In addition, the mean spectra of the background and the seventeen inserts of the CIRS phantom indicate a good accuracy in the energy domain. As for the simulated case, we noticed the difficulty to tune the Tikhonov regularization parameters in section 6.6. However, strong vertical stripes in the sinograms and ring artifacts in the reconstructed CT slices have been observed. The next chapter tries to tackle this issue.

7

Ring artifact correction

7.1 Introduction

Chapter 6 presented the evaluation of the method on experimental data acquired with two phantoms. The results on both of them were satisfactory but strong vertical stripes were observed in the sinograms, as well as ring artifacts in the reconstructed slices. The present chapter shows some ring artifacts correction methods we implemented (section 7.2) and the results we obtained with each of them (section 7.3). Then, we discuss in section 7.4.

7.2 Methods

At the borders of the 32 pixels crystals of the ME100 detectors, pixels count less photons than at the center. This phenomenon is clearly visible on the white image on the top of figure 6.5. Moreover, the bottom subfigure indicates these pixels are not stable and vary with parameters we were not able to identify. This instability induces a variation in the measured attenuation, in particular in uncollimated acquisitions and leads to the vertical stripes in the projections and the ring artifacts noticed in the later section. Moreover, the interpolation between two ME100 is done using these defect pixels, resulting in some significantly wide stripes (up to 4 pixels). The fact that some stripes are several pixels wide is a major difficulty for the ring artifacts correction. Another strong limitation is the fact that the central insert of the CIRS phantom is close to the rotation center, resulting in a projection in the sinograms very similar to stripes.

By using a discrete reconstruction method which takes into account the defect pixels, it may be possible to remove the ring artifacts [79]. However, in the case of an analytical reconstruction, a dedicated ring correction method has to be implemented. Several ring artifact correction methods exist in the literature. They can be divided into three groups: hardware-based, projection-based and object-based methods. The first one consists in moving the detector in order to blur the variations of the detector response. Projection-based ring correction methods aim at correcting sinograms before the reconstruction process, by removing the vertical stripes. The third group is related to post-processing on the reconstructed images, usually rebinned into polar coordinates in order to convert the rings into stripes.

In our context, an hardware-based correction was not possible, as it requires a specific device for moving the detector. An object-based correction method has been tested [80], but gave unsatisfactory results due to two issues. First, the method requires a coordinate transformation between Cartesian to polar, which induce errors, in particular in regions away from the rotation center. The second issue is linked with the number of projection angles acquired in the CT scan: only 180 projections were acquired, resulting in wave-shaped reconstruction artifacts hindering the removal of stripes. Aiming at correcting the ring artifacts observed in the reconstructed images, we propose to compare some projection-based correction methods. These methods take as input the attenuation sinograms and not the transmission ones. This is the reason why we proposed to correct the ring artifacts after applying the scatter correction method.

For each of the seven tested methods, we denote $\boldsymbol{g}$ the input ring corrupted attenuation sinogram and $\boldsymbol{g}^{\mathrm{C}k}$ the sinogram corrected with the k-st method. In addition, for the methods using an error model, this error (associated with ring correction method k) is denoted $\boldsymbol{q}^{\mathrm{C}k}$.

Methods four, five, six and seven are original ones, inspired by [81], [82] and [83].

The first method is based on wavelet filtering and is described in [84].

The second one solves the problem formulated in [81]. It states that the error is additive and does not depend on the projection angle:

$$g^{\mathrm{C2}}_{u,\theta} = g_{u,\theta} + q^{\mathrm{C2}}_{u}. \tag{7.1}$$

Knowing the pixel dependent error $\boldsymbol{q}^{\mathrm{C2}} \in \mathbb{R}^{N_U}$, one can recover the corrected sinogram $\boldsymbol{g}^{\mathrm{C2}}$:

$$\boldsymbol{g}^{\mathrm{C2}} = \boldsymbol{g} + \boldsymbol{U}\boldsymbol{q}^{\mathrm{C2}}, \tag{7.2}$$

with $\boldsymbol{U} \in \mathbb{R}^{N_U N_\Theta \times N_U}$ the matrix which maps the N_U correction values onto the complete sinogram and the pixel dependent error to be estimated. The error is estimated by minimizing the u-direction gradient of the sinogram, under the constraint that the error is small:

$$\tilde{\boldsymbol{q}}^{\mathrm{C2}} = \underset{\boldsymbol{q}^{\mathrm{C2}} \in \mathbb{R}^{N_U}}{\arg\min} \, \|\boldsymbol{\nabla}_U(\boldsymbol{g} + \boldsymbol{U}\boldsymbol{q}^{\mathrm{C2}})\|_2^2 + \lambda \|\boldsymbol{q}^{\mathrm{C2}}\|_2^2, \tag{7.3}$$

where $\boldsymbol{\nabla}_U \in \mathbb{R}^{N_U N_\Theta \times N_U N_\Theta}$ is the matrix performing the spacial gradient in the u-direction.

The third method considers a pixel and projection dependent error on the sinograms. The model is presented in [82] and states that:

$$\boldsymbol{g}^{\mathrm{C3}} = \boldsymbol{g} + \boldsymbol{q}^{\mathrm{C3}}, \tag{7.4}$$

with $\boldsymbol{q}^{\mathrm{C3}} \in \mathbb{R}^{N_U N_\Theta}$ the pixel and projection dependent error which is again estimated by minimizing the u-direction gradient of the sinogram:

$$\tilde{\boldsymbol{q}}^{\mathrm{C3}} = \underset{\boldsymbol{q}^{\mathrm{C3}} \in \mathbb{R}^{N_U N_\Theta}}{\arg\min} \; \|\boldsymbol{\nabla}_U(\boldsymbol{g} + \boldsymbol{q}^{\mathrm{C3}})\|_2^2 + \lambda \|\boldsymbol{q}^{\mathrm{C3}}\|_2^2. \tag{7.5}$$

The fourth method considers a pixel dependent multiplicative error (as in [83]):

$$g_{u,\theta}^{\mathrm{C4}} = g_{u,\theta} q_u^{\mathrm{C4}}. \tag{7.6}$$

The corrected sinogram is then recovered from the error $\boldsymbol{q}^{\mathrm{C4}} \in \mathbb{R}^{N_U}$ with:

$$\boldsymbol{g}^{\mathrm{C4}} = \mathrm{diag}(\boldsymbol{g}) \boldsymbol{U} \boldsymbol{q}^{\mathrm{C4}}. \tag{7.7}$$

Again, the error is estimated as the one that minimizes the gradient of the sinogram in the u-direction, the error being close to one:

$$\tilde{\boldsymbol{q}}^{\mathrm{C4}} = \underset{\boldsymbol{q}^{\mathrm{C4}} \in \mathbb{R}^{N_U}}{\arg\min} \; \|\boldsymbol{\nabla}_U \mathrm{diag}(\boldsymbol{g}) \boldsymbol{U} \boldsymbol{q}^{\mathrm{C4}}\|_2^2 + \lambda \|\boldsymbol{I} \boldsymbol{q}^{\mathrm{C4}} - \mathbf{1}\|_2^2, \tag{7.8}$$

$\mathbf{1} \in \mathbb{R}^{N_U}$ being a vector of ones.

In the same way as the third method, the fifth one is the generalization of the pixel dependent multiplicative error model to pixel and projection angle dependent multiplicative model:

$$g_{u,\theta}^{\mathrm{C5}} = g_{u,\theta} q_{u,\theta}^{\mathrm{C5}}. \tag{7.9}$$

With the error $\boldsymbol{q}^{\mathrm{C5}} \in \mathbb{R}^{N_U N_\Theta}$, one can recover the corrected sinogram with the following:

$$\boldsymbol{g}^{\mathrm{C5}} = \mathrm{diag}(\boldsymbol{g}) \boldsymbol{q}^{\mathrm{C5}}. \tag{7.10}$$

The error is then estimated with:

$$\tilde{\boldsymbol{q}}^{\mathrm{C5}} = \underset{\boldsymbol{q}^{\mathrm{C5}} \in \mathbb{R}^{N_U N_\Theta}}{\arg\min} \; \|\boldsymbol{\nabla}_U \mathrm{diag}(\boldsymbol{g}) \boldsymbol{q}^{\mathrm{C5}}\|_2^2 + \lambda \|\boldsymbol{I} \boldsymbol{q}^{\mathrm{C5}} - \mathbf{1}\|_2^2, \tag{7.11}$$

$\mathbf{1} \in \mathbb{R}^{N_U N_\Theta}$ being another vector of ones.

The last two methods are the same as the second and fourth, except that the gradient in the u-direction is not applied on each projection angle but only on the sum of the sinogram along the projections.

The sixth method seeks for the error as follows:

$$\tilde{\boldsymbol{q}}^{\mathrm{C6}} = \underset{\boldsymbol{q}^{\mathrm{C6}} \in \mathbb{R}^{N_U}}{\arg\min} \|\boldsymbol{\nabla}_U \boldsymbol{S}(\boldsymbol{g} + \boldsymbol{U}\boldsymbol{q}^{\mathrm{C6}})\|_2^2 + \lambda\|\boldsymbol{q}^{\mathrm{C6}}\|_2^2, \tag{7.12}$$

$\boldsymbol{S} \in \mathbb{R}^{N_U \times N_U N_\Theta}$ being the matrix summing the projections along the θ-direction and $\boldsymbol{\nabla}_U \in \mathbb{R}^{N_U \times N_U}$ modified u-direction gradient matrix.

Finally, the seventh method estimates the error with:

$$\tilde{\boldsymbol{q}}^{\mathrm{C7}} = \underset{\boldsymbol{q}^{\mathrm{C7}} \in \mathbb{R}^{N_U}}{\arg\min} \|\boldsymbol{\nabla}_U \boldsymbol{S}\mathrm{diag}(\boldsymbol{g})\boldsymbol{U}\boldsymbol{q}^{\mathrm{C7}}\|_2^2 + \lambda\|\boldsymbol{I}\boldsymbol{q}^{\mathrm{C7}} - \mathbf{1}\|_2^2 1. \tag{7.13}$$

For each method, the scalar parameter is determined manually as the one which removes the most stripes without blurring the object structures, in particular the central insert of the CIRS phantom. The linear systems of methods two and three can be solved with an analytical formula [81][82], but the conjugate gradient was used for every method in this work. After the correction with additive error models, the unattenuated pixels (where there is no object) were set to zero.

7.3 Results

Figures 7.1 and 7.2 show the results on the CIRS images for each method on total and estimated primary images respectively. First row corresponds to uncorrected images, while rows two to eight refers to methods one to seven. First and second columns show the sinograms and the absolute difference between corrected and uncorrected sinograms respectively, while third and fourth present the slice and the absolute difference between corrected and uncorrected slices.

We applied method two (Titarenko's model) on both datasets at low and high energy. The results are presented in figures 7.3 and 7.4. Left images represent ring corrected total slices, while center and right ones the ring corrected reference and estimated primary respectively. Left parts of images represent energy bin 2 and right ones energy bin 6.

7.4 Discussion

Various methods of the second group (projection-based methods) have been tested. Münch et al [84] proposed a wavelet-based filtering of the projections. This algorithm

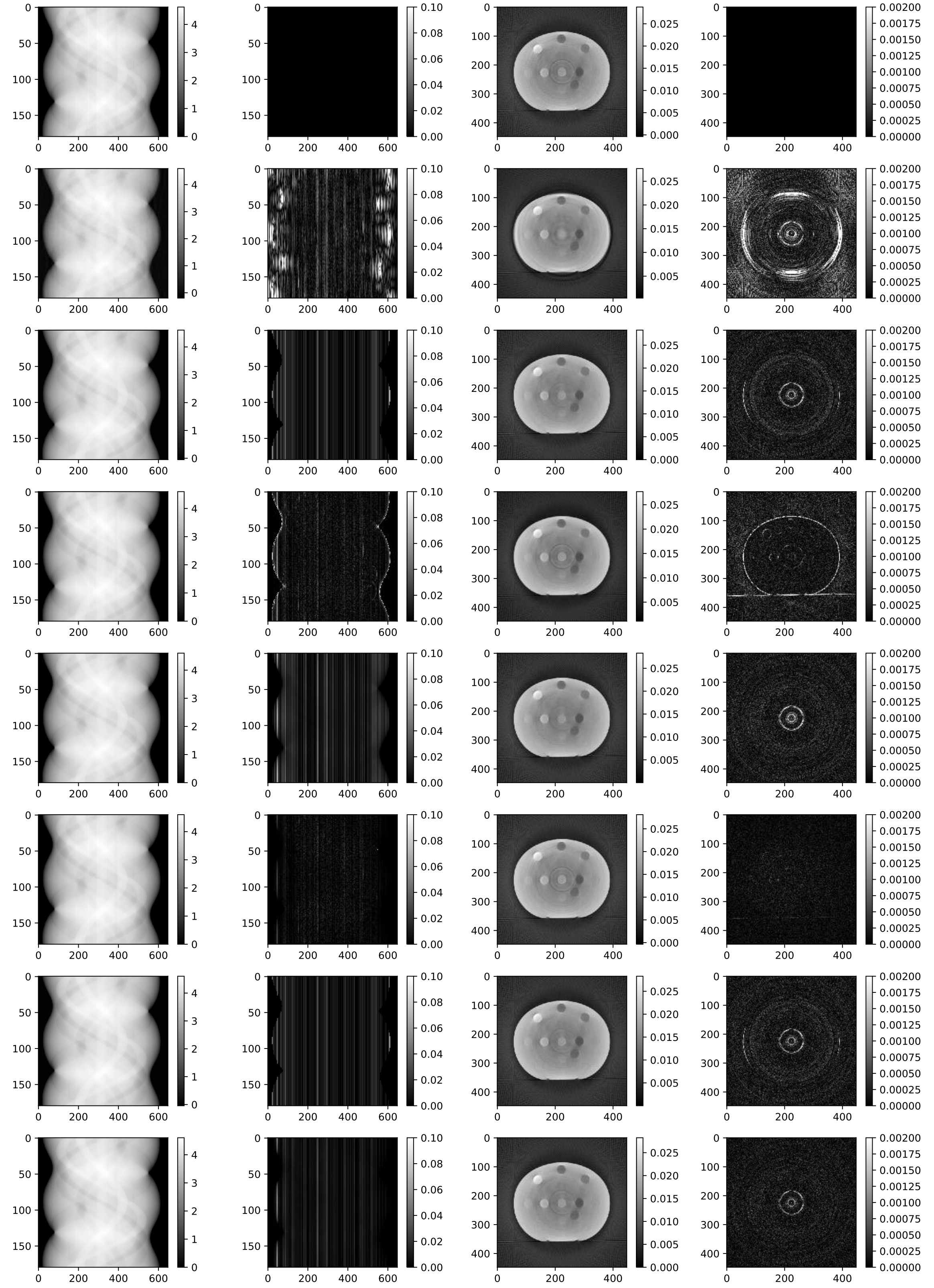

Figure 7.1 – Comparison of ring correction methods. First column: total sinogram; second column: absolute difference between corrected and uncorrected total sinograms; third column: ring corrected total slice; fourth column: absolute difference between corrected and uncorrected slices. First row: no correction; rows two to eight: methods one to seven

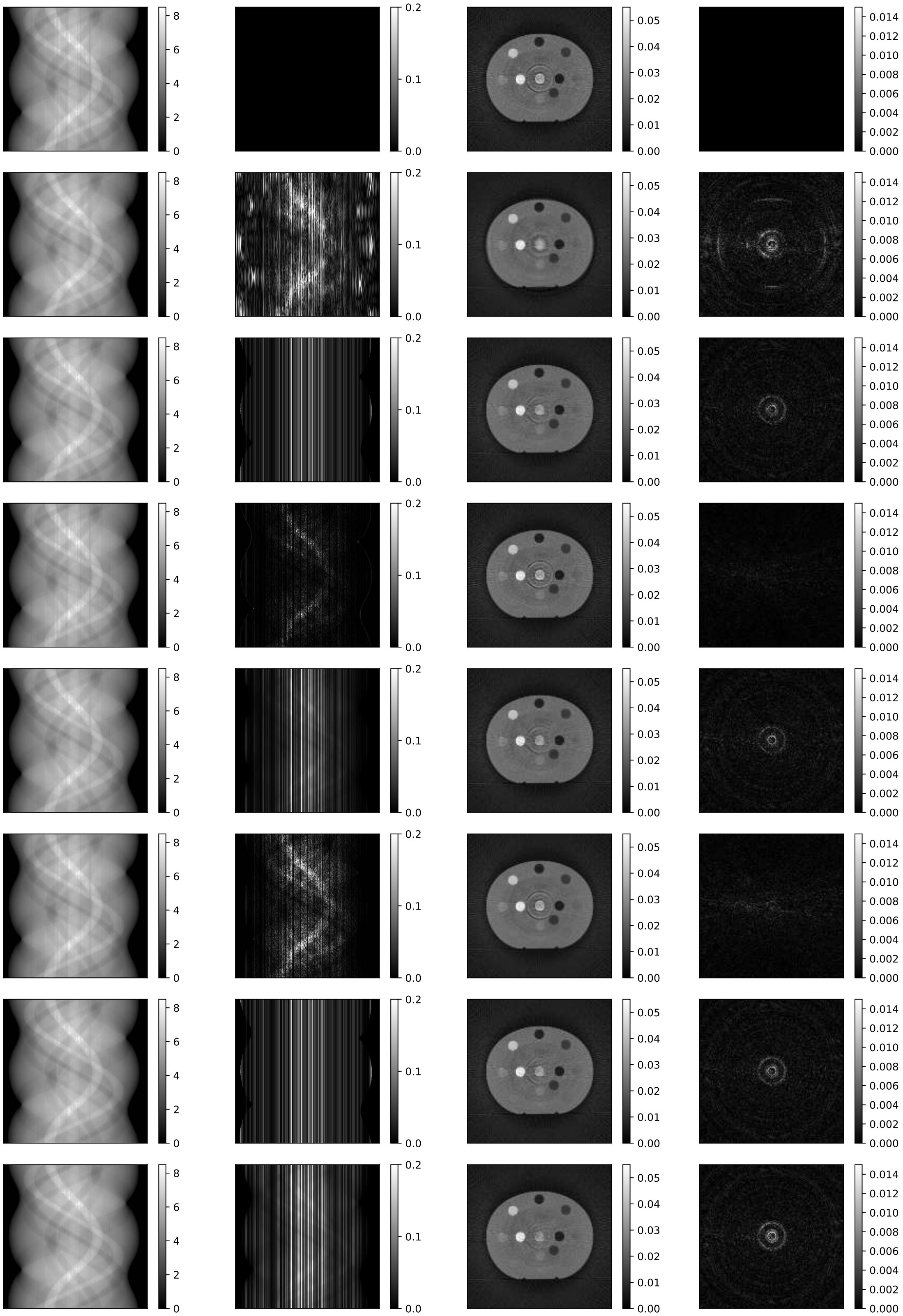

Figure 7.2 – Comparison of ring correction methods. First column: estimated primary sinogram; second column: absolute difference between corrected and uncorrected estimated primary sinograms; third column: ring corrected estimated primary slice; fourth column: absolute difference between corrected and uncorrected slices. First row: no correction; rows two to eight: methods one to seven

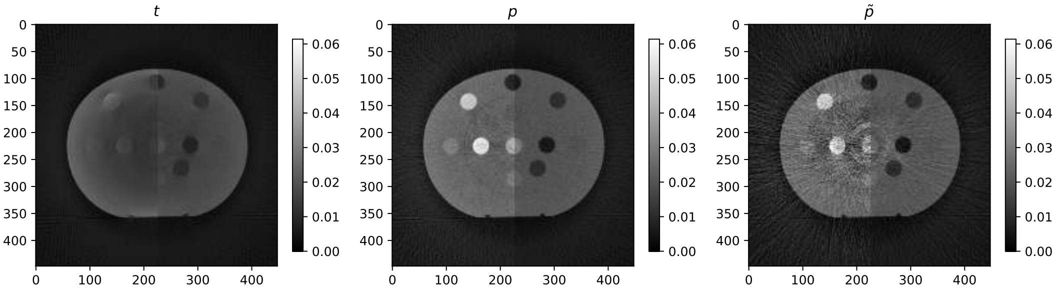

Figure 7.3 – CIRS slices after ring arifacts correction

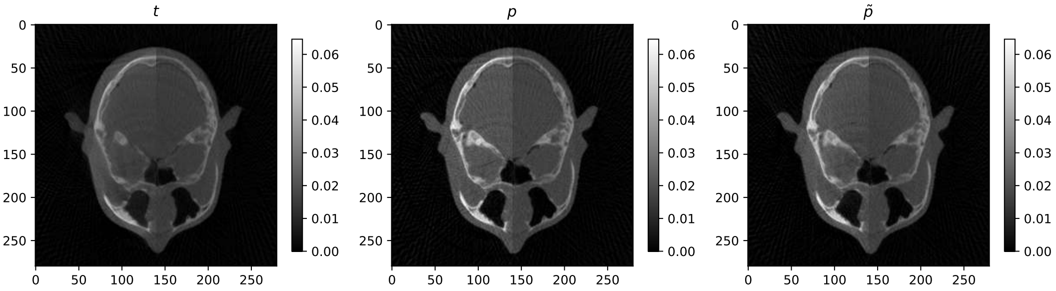

Figure 7.4 – RANDO slices after ring arifacts correction

is efficient for removing the stripes, but it also eliminated the structure caused by the central insert of the CIRS phantom. Other filtering strategies have been proposed in the literature but the similarity between stripes and central insert structures led us to focus on model-based variational approaches. The second method, with an additive error with no projection angle dependency, gave rather good results (see third rows of figures 7.1 and 7.2), most of the rings having been removed while the structures of the inserts are preserved. However, the wide stripe located around pixel of index $u = 385$ is still perceptible as well as the corresponding ring in the CT slice. The intensity of this stripe varies according to the projection angle, which justifies the testing of an additive error which depends on the projection angle (method three, fourth row of figures 7.1 and 7.2). However, it lowers the contrast of the object structures (in particular the ones induced by the highly attenuating insert corresponding to region of interest 10) more than the undesirable stripes, which is clear in the difference images. The same tests were performed using a multiplicative error model (methods four and five) which gave similar results as the additive ones due to the fact that the attenuation of a given pixel does not vary a lot along the projections. The stripes are more visible on the sinogram summed over the projections than on a single line of the sinogram. This is the reason why we tested methods six and seven, where the additive and multiplicative error are estimated by minimizing the gradient of the sum of the sinogram along the projections. No significant difference between summing and not summing over the projections have been observed.

In addition, for each method, a pixel binning has been tested before and after the correction. We also tested the generalization proposed in [85], where the second order derivative is used in place of the first derivative and a combined additive and multiplicative error model but no improvement has been obtained. Finally, we tried to replace the ℓ^2 norm by the ℓ^1 (generally preferred in denoising problems) but the lines of the corrected sinograms (or the sum of the lines in the case of methods six and seven) were piecewise constant, inducing a cupping artifact in each of the inserts.

Finally, we chose the second method, based on the model of [81]. Its application on single bin images (figures 7.3 and 7.4) show a significant improvement compared to uncorrected ones (figures 6.17 and 6.15), although we were not able to remove totally these ring artifacts.

7.5 Conclusion

Various ring artifact correction methods have been presented (section 7.2) and tested (section 7.3). Finally, as we have seen in section 7.4, we failed to remove totally the ring artifacts present in the CT slices, even if we rejected most of them.

8

Conclusion and perspectives

The objective of this PhD work was to develop a scatter correction method adapted to spectral computed tomography (CT) with photon counting detectors (PCD). We presented the basics of x-ray computed tomography in chapter 2, and explained the main differences between conventional CT using energy-integrating detectors and PCD along with a description of primary and scattered radiations and the influence of the latter on image quality.

Chapter 3 gave a state of the art of scatter correction methods. Recently introduced scatter correction methods using a semi-transparent primary modulator mask and based on the minimization of the primary gradient have shown promising results with energy-integrating detectors. Assuming that the scatter images are smooth and the primary ones are locally smooth, it states that the modulator pattern can be removed from the primary images if the scatter map is known, i.e the scatter map is the one which minimizes the primary gradient. Originally, the problem was formulated as a local minimization of the ℓ^1 norm of the primary gradient while a second study proposed a global minimization of its ℓ^2 norm with a specific weighting according to the object structures. The local minimization is generally more time consuming than the global one. The use of the ℓ^1 norm gives better results than the ℓ^2 one but its non differentiability makes it hard to minimize globally. Both of these methods decompose the acquired projection images into patches and a single value of scatter is associated with each one, resulting in a piece-wise constant scatter map. This enables to lower the dimensionality of the problem, but a smoothing step is required to retrieve the final scatter image. Moreover, the beam-hardening effect induced by the primary modulator mask affects the estimated primary images.

In chapter 4, we proposed a scatter correction method which fulfills the objectives of the thesis. We have presented a correction matrix which uses the spectral information to compensate for the mask attenuation with limited beam-hardening in section 4.3. We also proposed in section 4.4 a scatter model based on three dimensional B-spline functions, which gives directly smooth scatter sinograms. With this model, we were able to minimize the primary gradient according to the final scatter estimate, without the need of a smoothing step and using the redundancy of the images between adjacent projections. In section 4.5, a weighting according to the mask structures has been introduced and the object structures weighting was improved compared to the literature. The regularized cost function based on an approximation of the ℓ^1 norm that we designed was introduced in section 4.6. Finally, we presented in section 4.8 the Newton iteration that we used for the minimization.

The method has been successfully validated in chapter 5 on realistic simulated images using a 5 mm thick graphite primary modulator mask and a photon counting detector with 8 energy bins. We have shown that visually, a single iteration of the algorithm was sufficient to retrieve the scatter map, but a quantitative analysis indicates that a second one improves the results. We also pointed out the difficulty to tune the regularization parameters.

In chapter 6, we presented the experimental validation of the method on a parallel-beam x-ray tomographic system. We used the commercial line detector ME100 and two distinct phantoms. The results were satisfying, but strong ring artifacts degraded the reconstructed images, some of them being several pixels wide.

The problem of ring artifacts correction was tackled in chapter 7. We have tested various methods and model-based variational approaches gave the most satisfying results. Most of the ring artifacts have been correctly rejected, but we were not able to remove them totally.

Although the method has shown impressive results on both simulated and experimental images, some points may be improved. Regarding the correction matrix, we have shown that the empirical model we used is very accurate between two and twelve equally distributed energy bins. However, by modifying the model or by optimizing the spectral distribution of the energy bins, one may improve its accuracy. The dimensionality of the problem depends on the number of knots used in the B-spline based scatter model and we have seen that with a few number of regularly distributed knots, the model cannot represent accurately the highest frequencies of the scatter images, in particular near the object borders. Nevertheless, by placing more knots in the high scatter frequency regions and less in the others, the model accuracy may be improved without increasing dimensionality of the problem. Additionally, we explained that the design of the primary modulator mask follows a trade-off between several issues. According to these issues, we chose a 5 mm thick mask made with graphite. By using a mask made with aluminum, the error induced by the correction matrix inaccuracy would be greater, but its higher linear attenuation coefficient lead to lower parallax effect, for equal attenuation. Moreover, its mechanical properties are far better than the graphite ones, and a smaller pattern may be designed resulting in more mask edges pixels. Considering the full process of the scatter correction method, our graphite mask may not be the best trade-off. The design of the primary modulator mask is therefore still an open subject of investigation.

The use of a Tikhonov regularization has shown correct results, but the parameters controlling its strength are object-dependent and their tuning is a complicated task. It might be interesting to investigate on automatic procedures for the tuning of the Tikhonov parameters, as some authors already do in other applications. Another solution is more radical: changing the regularization function. A good candidate for such a regularization function could be based on data consistency conditions (DCC). DCC are necessary conditions that a sinogram must fulfill if it represents the x-ray transform of a given object [86].

$\mathcal{A}$

Smooth approximation of ℓ_1 norm using the Charbonnier function

The following appendix is a quick study of the Charbonnier function [75] used as a smooth approximation of the ℓ_1 norm for solving problems of the following form:

$$\tilde{\boldsymbol{x}} = \arg\min_{\boldsymbol{x}\in\mathbb{R}^M} \|\boldsymbol{b} - \boldsymbol{A}\boldsymbol{x}\|_1, \tag{A.1}$$

with $\boldsymbol{b} \in \mathbb{R}^N$, $\boldsymbol{A} \in \mathbb{R}^{N\times M}$ and $\boldsymbol{x} \in \mathbb{R}^M$.

The Charbonnier function of the ℓ_1 norm is defined as:

$$\begin{aligned} \mathcal{F}(\boldsymbol{x}) &= \|\boldsymbol{b} - \boldsymbol{A}\boldsymbol{x}\|_{1,\sigma} &\text{(A.2)}\\ &= \sum_n \sqrt{(b_n - \boldsymbol{a}_n^T\boldsymbol{x})^2 + \sigma^2} - \sigma, &\text{(A.3)} \end{aligned}$$

$\boldsymbol{a}_n$ being the n-th row of $\boldsymbol{A}$. This study presents the calculus of the first and second derivatives of $\mathcal{F}(\boldsymbol{x})$ (section A.1) and its minimization with the Newton's method (section A.2).

A.1 Derivatives

The first derivative of $\mathcal{F}(\boldsymbol{x})$ can be calculated directly from A.3:

$$\begin{aligned} \frac{\partial \mathcal{F}(x)}{\partial x_i} &= \sum_n \frac{1}{2} \frac{-2a_{i,n}(b_n - \boldsymbol{a}_n^T\boldsymbol{x})}{\sqrt{(b_n - \boldsymbol{a}_n^T\boldsymbol{x})^2 + \sigma^2}} &\text{(A.4)}\\ &= -\sum_n \frac{a_{i,n}(b_n - \boldsymbol{a}_n^T\boldsymbol{x})}{\sqrt{(b_n - \boldsymbol{a}_n^T\boldsymbol{x})^2 + \sigma^2}}. &\text{(A.5)} \end{aligned}$$

In the same manner, its second derivative comes directly from A.5:

$$\frac{\partial^2 \mathcal{F}(x)}{\partial x_i \partial x_j} = -\sum_n \frac{-a_{i,n}a_{j,n}\sqrt{(b_n - \boldsymbol{a}_n^T\boldsymbol{x})^2 + \sigma^2} + a_{i,n}(b_n - \boldsymbol{a}_n^T\boldsymbol{x})\frac{1}{2}\frac{-2a_{j,n}(b_n - \boldsymbol{a}_n^T\boldsymbol{x})}{\sqrt{(b_n - \boldsymbol{a}_n^T\boldsymbol{x})^2 + \sigma^2}}}{(b_n - \boldsymbol{a}_n^T\boldsymbol{x})^2 + \sigma^2} \tag{A.6}$$

$$= \sum_n \frac{a_{i,n}a_{j,n}}{\sqrt{(b_n - \boldsymbol{a}_n^T\boldsymbol{x})^2 + \sigma^2}} - \frac{a_{i,n}a_{j,n}(b_n - \boldsymbol{a}_n^T\boldsymbol{x})^2}{\Big((b_n - \boldsymbol{a}_n^T\boldsymbol{x})^2 + \sigma^2\Big)^{\frac{3}{2}}} \tag{A.7}$$

$$= \sum_n a_{i,n}a_{j,n}\left(\Big((b_n - \boldsymbol{a}_n^T\boldsymbol{x})^2 + \sigma^2\Big)^{-\frac{1}{2}} - (b_n - \boldsymbol{a}_n^T\boldsymbol{x})^2\Big((b_n - \boldsymbol{a}_n^T\boldsymbol{x})^2 + \sigma^2\Big)^{-\frac{3}{2}}\right) \tag{A.8}$$

From A.5, one can retrieve the matrix formulation of the gradient:

$$\boldsymbol{\nabla}[\mathcal{F}](\boldsymbol{x}) = -\boldsymbol{A}^T \mathrm{diag}\left(\Big(\sqrt{(\boldsymbol{b} - \boldsymbol{A}\boldsymbol{x})^2 + \sigma^2}\Big)^{-\frac{1}{2}}\right)(\boldsymbol{b} - \boldsymbol{A}\boldsymbol{x}), \tag{A.9}$$

and from A.8 the matrix formulation of the Hessian:

$$\boldsymbol{H}[\mathcal{F}](\boldsymbol{x}) = \boldsymbol{A}^T \mathrm{diag}\left(\Big(\sqrt{(\boldsymbol{b} - \boldsymbol{A}\boldsymbol{x})^2 + \sigma^2}\Big)^{-\frac{1}{2}} - (\boldsymbol{b} - \boldsymbol{A}\boldsymbol{x})^2\Big((\boldsymbol{b} - \boldsymbol{A}\boldsymbol{x})^2 + \sigma^2\Big)^{-\frac{3}{2}}\right)\boldsymbol{A}. \tag{A.10}$$

A.2 Minimization using the Newton's method

The minimization of $\mathcal{F}(\boldsymbol{x})$ can be done using Newton's method, starting with an initial guess $\boldsymbol{x}^{(0)}$ and building new estimates with the following update rule:

$$\boldsymbol{x}^{(n+1)} = \boldsymbol{x}^{(n)} + \delta\boldsymbol{x}^{(n)}, \tag{A.11}$$

where $\delta\boldsymbol{x}^{(n)} \in \mathbb{R}^M$ denotes Newton's step at iteration (n).

Newton's step is obtained solving the following linear system:

$$\boldsymbol{H}[\mathcal{F}](\boldsymbol{x}^{(n)})\delta\boldsymbol{x}^{(n)} = -\boldsymbol{\nabla}[\mathcal{F}](\boldsymbol{x}^{(n)}). \tag{A.12}$$

B

Relation between bin indices and energy range for several energy bin numbers

This appendix regroups the tables giving the relation between the bin indices and the energy range for various numbers of energy bins N_B going from 2 to 24.

b	Energy range
1	30 keV to 75 keV
2	75 keV to 120 keV

Table B.1 – Relation between bin index and energy range for $N_B = 2$

b	Energy range
1	30 keV to 52 keV
2	52 keV to 74 keV
3	74 keV to 96 keV
4	96 keV to 120 keV

Table B.2 – Relation between bin index and energy range for $N_B = 4$

b	Energy range
1	30 keV to 44 keV
2	44 keV to 58 keV
3	58 keV to 72 keV
4	72 keV to 88 keV
5	88 keV to 94 keV
6	104 keV to 120 keV

Table B.3 – Relation between bin index and energy range for $N_B = 6$

b	Energy range
1	30 keV to 40 keV
2	40 keV to 50 keV
3	50 keV to 60 keV
4	60 keV to 72 keV
5	72 keV to 84 keV
6	84 keV to 96 keV
7	96 keV to 108 keV
8	108 keV to 120 keV

Table B.4 – Relation between bin index and energy range for $N_B = 8$

b	Energy range
1	30 keV to 36 keV
2	36 keV to 42 keV
3	42 keV to 48 keV
4	48 keV to 56 keV
5	56 keV to 64 keV
6	64 keV to 72 keV
7	72 keV to 80 keV
8	80 keV to 88 keV
9	88 keV to 96 keV
10	96 keV to 104 keV
11	104 keV to 112 keV
12	112 keV to 120 keV

Table B.5 – Relation between bin index and energy range for $N_B = 12$

b	Energy range
1	30 keV to 40 keV
2	40 keV to 50 keV
3	50 keV to 60 keV
4	60 keV to 72 keV
5	72 keV to 84 keV
6	84 keV to 96 keV
7	96 keV to 108 keV
8	108 keV to 120 keV
9	30 keV to 40 keV
10	40 keV to 50 keV
11	50 keV to 60 keV
12	60 keV to 72 keV
13	72 keV to 84 keV
14	84 keV to 96 keV
15	96 keV to 108 keV
16	108 keV to 120 keV

Table B.6 – Relation between bin index and energy range for $N_B = 16$

b	Energy range
1	30 keV to 32 keV
2	32 keV to 34 keV
3	34 keV to 36 keV
4	36 keV to 40 keV
5	40 keV to 44 keV
6	44 keV to 48 keV
7	48 keV to 52 keV
8	52 keV to 56 keV
9	56 keV to 60 keV
10	60 keV to 64 keV
11	64 keV to 68 keV
12	68 keV to 72 keV
13	72 keV to 76 keV
14	76 keV to 80 keV
15	80 keV to 84 keV
16	84 keV to 88 keV
17	88 keV to 92 keV
18	92 keV to 96 keV
19	96 keV to 100 keV
20	100 keV to 104 keV
21	104 keV to 108 keV
22	108 keV to 112 keV
23	112 keV to 116 keV
24	116 keV to 120 keV

Table B.7 – Relation between bin index and energy range for $N_B = 24$

C

Mean spectra of regions of interest

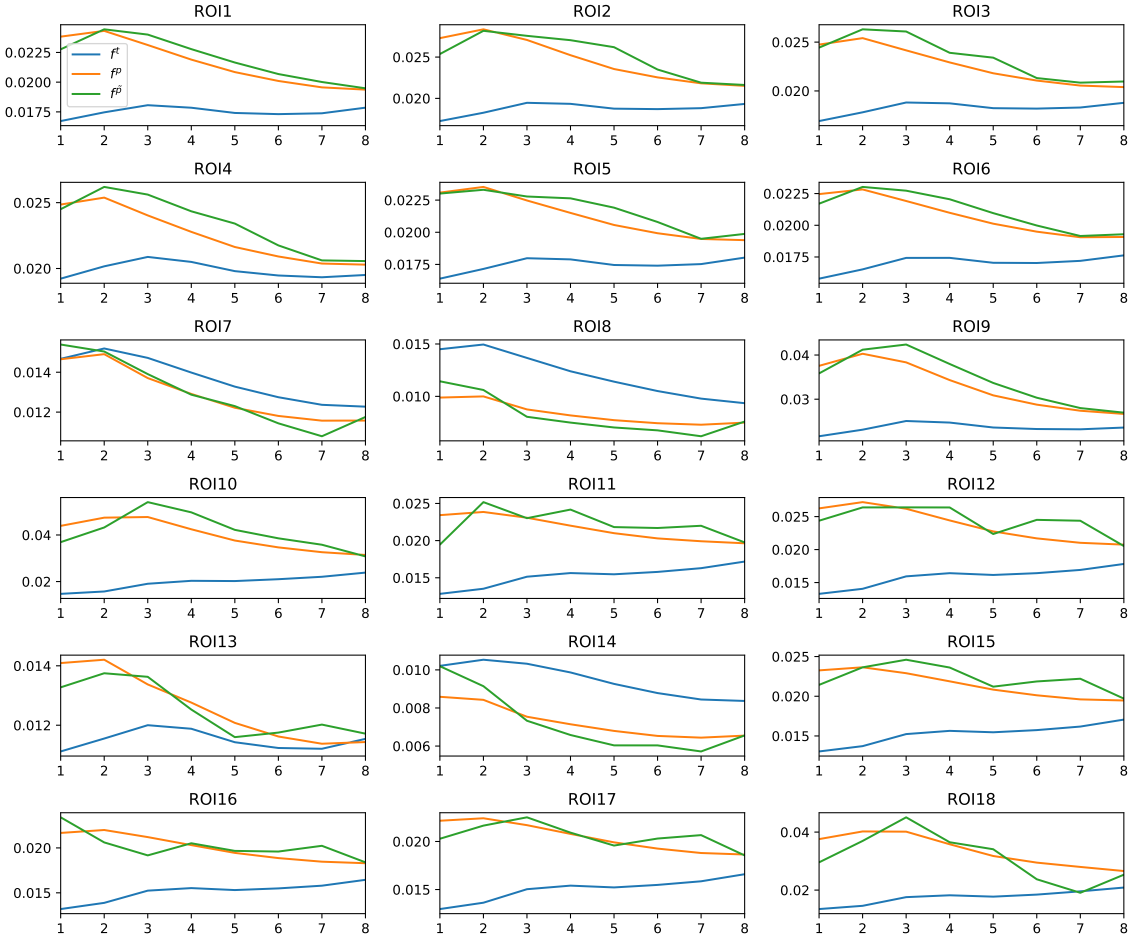

Figure C.1 – Mean spectra of regions of interest

D

Résumé de la thèse en français

D.1 Introduction

La tomographie par rayons x est une des principales modalités utilisées en imagerie médicale. Depuis l'invention du scanner tomographique par Godfrey Hounsfield en 1971, des avancées significatives ont été réalisées tant sur le matérial, avec l'amélioration des tubes à rayons x, des collimateurs, des systèmes de rotation et des détecteurs, que sur le logiciel avec le développement de nombreux algorithmes de reconstruction et d'élimination d'artéfacts.

Récemment, l'émergence des détecteurs à comptage de photons, une nouvelle technologie de détection basée sur l'utilisation de matériaux semi-conducteurs, permet de compter les photons indépendamment et de les classifier dans des canaux discrets en fonction de leur énergie. Cette nouvelle technologie (avec un nombre de canaux allant de 2 à 8) équipe d'ores et déjà quelques prototypes de scanners médicaux et est en cours d'évaluation dans des centres de recherche clinique. Pour d'autres applications industrielles, quelques détecteurs linéaires à comptage de photons ont jusqu'à une centaine de canaux d'environ 1 keV de large. Alors que les détecteurs à intégration utilisés dans les scanners conventionnels fournissent de simples images, les détecteurs à comptage de photons fournissent des images spectrales. L'utilisation de l'information spectrale ouvre de nouvelles perspectives comme la possibilité d'améliorer le rapport contraste sur bruit, la réduction de la dose ou l'élimination d'artéfacts. De plus, cela permet de quantifier chaque matériau constituant l'objet indépendamment en décomposant les images en fonctions de base, par exemple en images d'os et de tissus mous. Cependant, ces décompositions requièrent une haute précision quantitative des images pour chaque canal d'énerige. En particulier, le rayonnement diffusé induit un biais, une perte de contraste et des artéfacts. C'est la raison pour laquelle il est nécessaire de corriger ses effets.

L'objectif de ce travail de thèse est de développer une méthode de correction du diffusé adaptée à l'imagerie spectrale tomographique capable de fournir des images précises sans augmenter la dose ni le temps d'acquisition.

D.2 Fondamentaux de l'imagerie tomographique

Cette première section vise à introduire les fondamentaux de l'imagerie tomographique. Une acquisition tomographique consiste en un jeu d'acquisitions radiographiques effectuées à différents angles de projection autour de l'objet imagé. Après leur génération, les rayons x intéragissent avec l'objet en le traversant et sont ensuite détectés pour former les radiographies. Les images tomographiques sont ensuite générées avec un algorithme de reconstruction.

D.2.1 Les rayons x en imagerie médicale

Les rayons x ont été découverts en 1895 par Wilhelm Röntgen, et font partie du spectre électromagnétique. Dans un scanner médical, les rayons x sont générés par un tube à rayons x, dans lequel les électrons sont accélérés par une haute tension. L'énergie des photons est généralement exprimée en eV (l'énergie d'un photon accéléré sous la tension de 1 V) plutôt qu'en J.

D.2.2 Rayonnements primaire et diffusé

En traversant un objet, le flux de rayons x intéragit par le biais de différents phénomènes physiques : l'effet photoélectrique, la diffusion Rayleigh et la diffusion Compton.

Les phénomènes de diffusion Rayleigh et Compton induisent une modification de la trajectoire du photon et, pour l'effet Compton, une baisse de son énergie. Le flux résultant peut être divisé en un flux de rayonnement primaire (les photons n'ayant pas intéragi, et conservant donc leur trajectorie initiale) et un flux de rayonnement diffusé.

Le rayonnement primaire peut être obtenu analytiquement par la formule de Beer-Lambert.

Bien que le rayonnement diffusé ne soit pas facilement modélisable comme le primaire, nous avons un a priori fort sur son comportement : les images du diffusé sont lisses dans les deux directions du détecteur et dans la direction des projections.

D.2.3 Détection des rayons x

En imagerie x conventionnelle, les détecteurs utilisés sont dits "à intégration". Ils fournissent une valeur scalaire en chaque pixel, qui dépend de l'intégrale sur l'énergie du flux incident pondéré par une fonction de détection.

La technologie récente des détecteurs à comptage de photons, basée sur des matériaux semiconducteurs, permet de compter indépendamment les photons, et de les classifier dans des canaux discrets en fonction de leur énergie. Chaque canal comportant sa propre fonction de réponse, il est possible de construire une matrice de réponse du détecteur en concaténant les fonctions de réponse discrétisées pour chaque canal. Un exemple de matrice de réponse du détecteur est présenté sur la figure D.1.

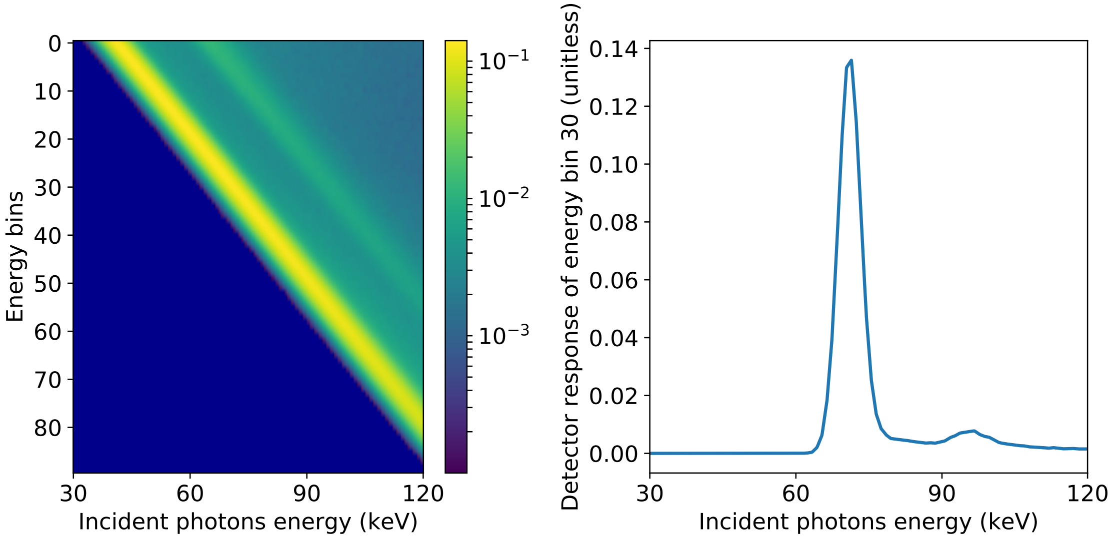

FIGURE D.1 – Exemple de matrice de réponse d’un détecteur en CdTe avec $N_B = 90$ canaux d’environ 1 keV de large (gauche). Réponse du canal 30, centré sur 70 keV (droite).

D.2.4 Reconstruction tomographique

Un algorithme de reconstruction tomographique est un algorithme qui permet de reconstruire l’image en atténuation de l’objet à partir des données tomographiques acquises. Deux classes de méthodes de reconstruction se distinguent : les méthodes de reconstruction analytique et les méthodes discrètes.

D.2.5 Influence du diffusé

Nous avons vu que les images de diffusé contiennent essentiellement des basses-fréquences. Cependant, son influence sur les images en atténuation dépend du rapport diffusé/primaire. Le biais qu’il induit dépend donc à la fois du primaire et du diffusé.

Les effets principaux du diffusé sont une baisse du contraste sur les images (tant sur les projections que sur les volumes reconstruits), et un artéfact en forme de coupe sur les images reconstruites.

D.3 Correction du rayonnement diffusé : état de l'art

Le problème du rayonnement diffusé est connu depuis les débuts de l'imagerie par rayons x, et a donné lieu à une multitude de méthodes que l'on peut classer en deux familles : les méthodes matérielles et les méthodes logicielles.

D.3.1 Méthodes matérielles

La famille des méthodes de correction du diffusé matérielles consiste à adapter la géométrie ou à utiliser un dispositif additionnel pour réduire la quantité de rayonnement diffusé détéctée.

La stratégie la plus commune pour limiter le diffusé détecté consiste à collimater les pixels du détecteur avec une grille anti-diffusé. Une seconde consiste à augmenter la distance entre l'objet et le détecteur. Finalement, il est également possible de limiter la diffusion en collimatant le champ de vue.

D.3.2 Méthodes logicielles

Les méthodes logicielles visent à modifier les données acquises afin de corriger l'effet du diffusé.

Parmis elles, on peut isoler la famille des méthodes basées sur un modèle. Ces méthodes cherchent à estimer l'image de diffusé afin de la soustraire à l'image acquise. L'approche la plus classique consiste à modéliser le diffusé comme une fonction de l'image acquise, à laquelle on applique un filtre passe-bas : le scatter kernel. D'autres méthodes utilisent des simulations Monte Carlo, capables de fournir une grande précision mais dans des temps prohibitifs.

Une autre grande famille de méthodes consiste à utiliser un dispositif, généralement placé entre la source et l'objet, qui modifie le flux de rayons x de sorte que l'on puisse en déduire l'image du diffusé. L'approche la plus répandue, la méthode d'arrêt du faisceau, permet d'obtenir des images très précises, mais nécessite une seconde acquisition sans le dispositif modifiant le flux. Cela signifie une augmentation du temps d'acquisition et de la dose déposée.

D.3.3 Correction basée sur le gradient du primaire modulé

Cette sous-famille de méthodes, qui est à la base de la méthode développée dans cette thèse, propose de placer un masque semi-transparent (appelé masque modulateur de primaire) entre la source et l'objet, comme sur la figure D.2.

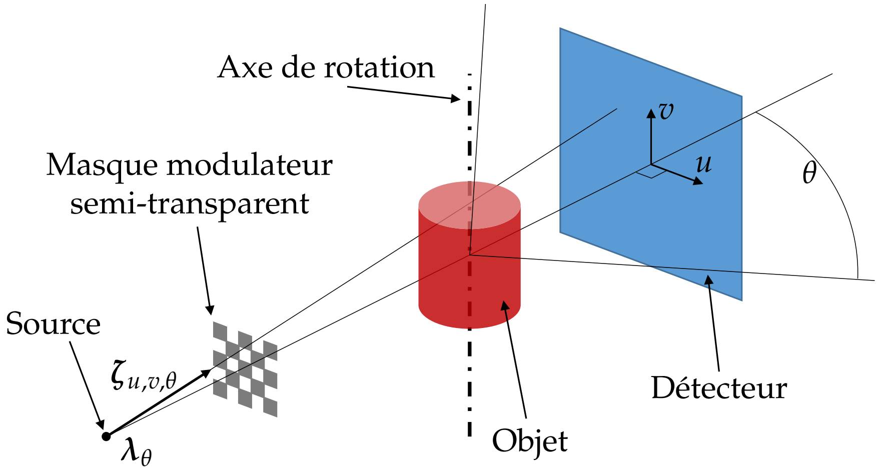

FIGURE D.2 – Système d'imagerie avec un masque modulateur de primaire

Dans cette situation, la mesure $\hat{\boldsymbol{t}}$ est la somme de la composante du primaire modulé par le masque $\hat{\boldsymbol{p}}$ et du diffusé $\boldsymbol{s}$:

$$\hat{\boldsymbol{t}} = \hat{\boldsymbol{p}} + \boldsymbol{s}. \tag{D.1}$$

Si on connait une matrice $\boldsymbol{C}$ capable de compenser l'atténuation du masque (c'est-à-dire capable de retrouver le primaire que l'on aurait mesuré sans masque à partir du primaire modulé par le masque), et l'image de diffusé $\boldsymbol{s}$, on peut retrouver le primaire directement :

$$\boldsymbol{p} = \boldsymbol{C}\hat{\boldsymbol{p}} = \boldsymbol{C}(\hat{\boldsymbol{t}} - \boldsymbol{s}). \tag{D.2}$$

Si on considère une estimation biaisée du diffusé, l'estimation correspondante du primaire contiendra le motif du masque, et si le masque a des bords francs, la présence de son motif va engendrer une augmentation du gradient spatial de l'image de primaire. La méthode consiste donc à chercher l'image (lisse) de diffusé qui minimise le gradient spatial du primaire estimé.

Les limitations de cette méthodes sont plurielles. Une limitation importante est la difficulté de trouver une matrice $\boldsymbol{C}$ qui compense l'attenuation du masque, à cause du durcissement du faisceau qu'il induit.

D.3.4 Conclusion et motivation de la thèse

Le contexte de cette thèse est l'imagerie tomographique spectrale, basée sur l'utilisation de détecteurs à comptage de photons. La plupart des méthodes décrites dans la littérature ont été développées pour la tomographie conventionnelle (utilisant des détecteurs à intégration). Si la majorité d'entre elles peuvent être appliquées indépendamment sur les données issues de chaque canal d'une acquisition spectrale, l'information sur l'énergie des photons peut améliorer les performances de certaines d'entre elles. En particulier, celà peut permettre de limiter le durcissement du faisceau induit par un masque modulateur de primaire dans les méthodes de correction basées sur le gradient du primaire modulé, qui est l'inconvénient majeur de ces méthodes.

Dans la section suivante, nous présentons une méthode de correction du diffusé adaptée à l'imagerie spectrale et basée sur le gradient du primaire modulé.

D.4 Correction du rayonnement diffusé en imagerie tomographique spectrale basée sur l'utilisation d'un masque modulateur de primaire

D.4.1 Matrice de correction

La méthode nécessite la connaissance d'une matrice de correction $\boldsymbol{C}$ capable de compenser l'atténuation du masque, en étant idéalement indépendant du durcissement du faisceau. Son calcul par une formule analytique, bien que possible en théorie, se révèle impossible en pratique. Nous avons donc choisis de la calculer par le biais d'un modèle. Les paramètres optimaux du modèle sont ensuite estimé à l'aide d'images de calibration acquises avec différents niveaux d'atténuation.

D.4.2 Modèle de diffusé

Afin de représenter des images lisses de diffusé avec un nombre très limité de paramètres, nous avons choisi de le représenter dans une base de B-splines d'ordre 2. Concrètement, nous avons défini une grille régulière de noeuds le long des trois dimensions spatiales (deux directions du détecteur et une direction angulaire). À chaque noeud B-spline est associé une fonction de base B-spline et un poids, l'image totale de diffusé étant la somme des contributions de chaque fonction de base pondérée par le poids correspondant.

Les fonctions de base B-spline sont concaténées dans une matrice $\boldsymbol{B}$, de telle sorte que l'image de diffusé $\boldsymbol{s}$ soit obtenue à partir du vecteur $\boldsymbol{x}$ contenant les poids associés à chacun des noeuds B-spline :

$$\boldsymbol{s} = \boldsymbol{B}\boldsymbol{x} \tag{D.3}$$

D.4.3 Pondération en fonction des structures du masque et de l'objet

Afin de s'affranchir de la dépendance de la méthode aux structures de l'objet, nous avons proposé de pondérer le gradient du primaire estimé en utilisant deux matrices (diagonales) de pondération distinctes. La première, $\boldsymbol{W}_1$ permet de selectionner les pixels aux bords du masque, c'est-à-dire ceux portant l'information de la présence ou l'absence du motif du masque dans le primaire. La seconde, $\boldsymbol{W}_2$, permet de donner moins d'importance aux zones de l'image où les structures de l'objet sont fortes, par exemple aux bords de l'objet.

D.4.4 Fonction de coût

Nous avons ensuite conçu une fonction de coût régularisée permettant de quantifier précisément la présence du motif du masque dans le primaire. Les paramètres du modèle de diffusé s'estiment donc en résolvant le problème d'optimisation suivant :

$$\tilde{\boldsymbol{x}} \in \underset{\boldsymbol{x} \in \mathbb{R}^{N_B N_K}}{\arg\min}\, \mathcal{F}(\boldsymbol{x}) + \mathcal{R}(\boldsymbol{x}), \tag{D.4}$$

avec

— $\mathcal{F}(\boldsymbol{x}) = \left\| \boldsymbol{W}_1 \boldsymbol{W}_2 \boldsymbol{\nabla} \boldsymbol{C}(\hat{\boldsymbol{t}} - \boldsymbol{B}\boldsymbol{x}) \right\|_{1,\sigma}$,
le terme d'attache aux données, correspondant au gradient pondéré du primaire estimé. Nous avons choisi une approximation douce de la norme ℓ^1 afin de limiter la dépendance de la méthode aux données aberrantes : la fonction de Charbonnier.

— $\mathcal{R}(\boldsymbol{x})$,
une fonction de régularisation de type Tikhonov.

D.5 Résultats

La méthode a été testée sur un jeu de données simulées et deux jeux de données experimentales. Les données simulées ont été obtenues à partir d'un fantôme anthropomorphique numérique, l'acquisition est centrée sur la tête. Le premier jeu de données expérimentales a été acquis avec un fantôme de tête humaine, et le second avec un fantôme de la taille d'un thorax, consistant à une ellipsoïde de plastique imitant l'atténuation de l'eau, avec des inserts cylindriques représentant l'atténuation de différents tissus biologiques. Le masque que nous avons conçu est une plaque de

5 mm d'épaisseur, en graphite, percée de trous.

La figure D.3 représente une coupe tomographique des données simulées à deux énergies (les sous-images de gauche représentent le canal 2, alors que les sous-images de droite représentent le canal 6). L'image de gauche correspond à l'acquisition avec diffusé, celle du milieu à une acquisition sans diffusé, et l'image de droite à l'image obtenue après application de la méthode proposée. Les figures D.4 et D.5 représentent des coupes tomographiques des deux jeux de données experimentales.

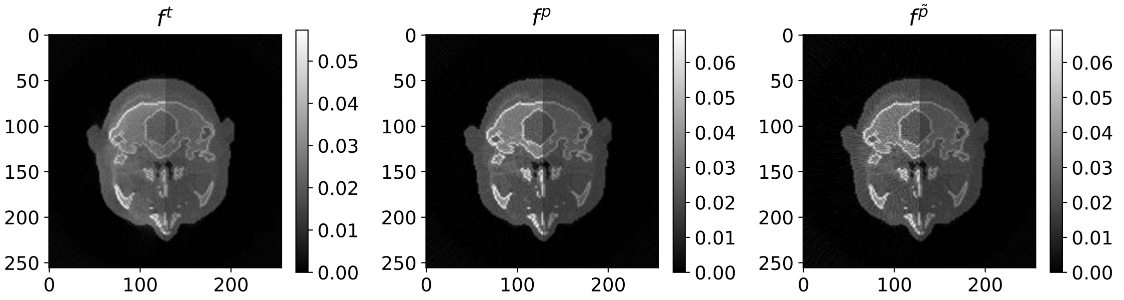

FIGURE D.3 – Coupe tomographique du fantôme simulé. Total (gauche), primaire (centre) et primaire estimé (droite) à basse énergie (canal 2, sous-figures gauches) et haute énergie (canal 6, sous-figures droites)

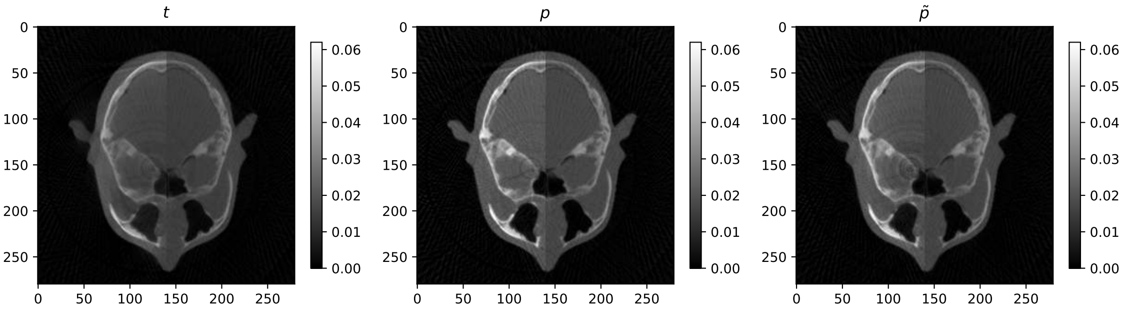

FIGURE D.4 – Coupe tomographique du fantôme de tête. Total (gauche), primaire (centre) et primaire estimé (droite) à basse énergie (canal 2, sous-figures gauches) et haute énergie (canal 6, sous-figures droites).

D.6 Discussion

La méthode proposée a montré, tant sur les données simulées qu'experimentales, une réduction satisfaisante du diffusé sur les images. On peut voir sur les figures D.3, D.4 et D.5 que le contraste a été considérablement réhaussé, en particulier sur le

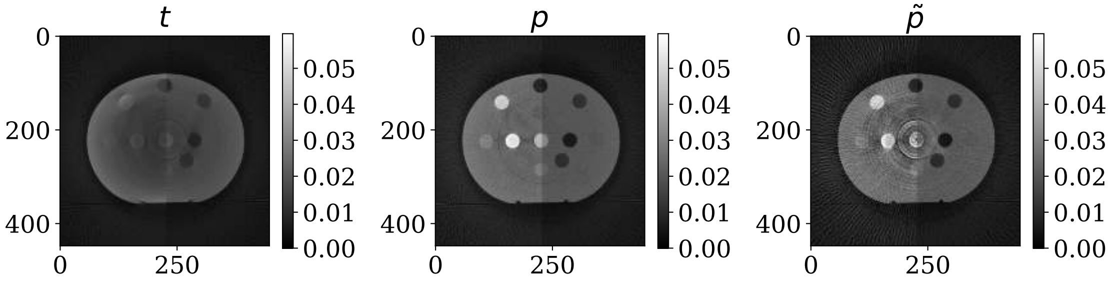

FIGURE D.5 – Coupe tomographique du fantôme immitant des tissus biologiques. Total (gauche), primaire (centre) et primaire estimé (droite) à basse énergie (canal 2, sous-figures gauches) et haute énergie (canal 6, sous-figures droites)

dernier cas.

La méthode nécessite le réglage de différents paramètres scalaires (non présentés dans ce document), et est très sensible à certains d'entre eux. La difficulté de régler certains paramètres est une faiblesse majeure de la méthode proposée, car elle limite son indépendance vis à vis de l'objet.

Sur les données simulées, la différence de réponse entre les différents pixels a induit des artéfacts en anneaux, visibles en particulier sur la figure D.5. La correction de cet artéfact a été l'objet d'une étude, mais aucune méthode testée n'a réussi à le corriger de manière satisfaisante.

D.7 Conclusion

L'objectif de ce travail de thèse était de développer une méthode de correction du diffusé adaptée à l'imagerie tomographique spectrale basée sur l'utilisation de détecteurs à comptage de photons. Nous avons proposé une méthode qui satisfait ces objectifs. Cependant, différents points restent à améliorer. D'abord, la conception du masque peut être optimisée (matériau, épaisseur, motif). Ensuite, il conviendrait de trouver une méthode permettant de régler automatiquement les paramètres optimaux nécessaires à une correction effective du diffusé. Il parait également possible d'améliorer la méthode en modifiant le terme de régularisation de la fonction de coût. Nous avons utilisé une régularisation de type Tikhonov, mais une régularisation basée sur un critère de consistance des données tomographiques pourrait s'avérer pertinent.

E

Scientific contributions

Publications

O. Pivot, C. Fournier, J. Tabary, J.M. Létang, S. Rit. Scatter correction for spectral CT using a primary modulator mask. *IEEE Transactions on Medical Imaging*, to be published.

Conferences

Oral presentation at the 2018 IEEE Nuclear Science Symposium and Medical Imaging Conference entitled:
"Scatter estimation for spectral CT using a primary modulator mask."

Patents

The proposed method has been the subject of a patent.

Bibliography

[1] J. Hsieh. *Computed Tomography: Principles, Design, Artifacts, and Recent Advances*. SPIE PRESS BOOK, 2003.

[2] A. Sossin. *Correction of scattered radiation in multi-energy radiography and tomography*. PhD thesis, 2016.

[3] D. Peplow and K. Verghese. Measured molecular coherent scattering form factors of animal tissues, plastics and human breast tissue. *Physics in Medicine and Biology*, 43(9):2431–2452, 1998.

[4] J. H. Hubbell, W. J. Veigele, E. A. Briggs, R. T. Brown, D. T. Cromer, and R. J. Howerton. Atomic form factors, incoherent scattering functions, and photon scattering cross sections. *Journal of Physical and Chemical Reference Data*, 4(3):471, 2009.

[5] J. H. Hubbell and S.M. Seltzer. Tables of x-ray mass attenuation coefficients and mass energy-absorption coefficients 1 kev to 20 mev for elements z = 1 to 92 and 48 additional substances of dosimetric interest. *International Journal of Applied Radiation and Isotopes*, 1269(33), 1982.

[6] G. J. Bootsma, F. Verhaegen, and D. A. Jaffray. Spatial frequency spectrum of the x-ray scatter distribution in CBCT projections. *Medical Physics*, 40(11):111901, 2013.

[7] A. Sossin, V. Rebuffel, J. Tabary, J. M. Létang, N. Freud, and L. Verger. Characterizing the behavior of scattered radiation in multi-energy x-ray imaging. *Nuclear Instruments and Methods in Physics Research Section A: Accelerators, Spectrometers, Detectors and Associated Equipment*, 850:25–34, 2017.

[8] K. Taguchi and J. Iwanczyk. Vision 20/20: Single photon counting x-ray detectors in medical imaging. *Medical Physics*, 40(10):100901, 2013.

[9] A. Brambilla, P. Ouvrier-Buffet, G. Gonon, J. Rinkel, V. Moulin, C. Boudou, and L. Verger. Fast CdTe and CdZnTe semiconductor detector arrays for spectroscopic x-ray imaging. *IEEE Transactions on Nuclear Science*, 60(1):408–415, 2013.

[10] S. Leng, W. Zhou, Z. Yu, A. Halaweish, B. Krauss, B. Schmidt, L. Yu, S. Kappler, and C. McCollough. Spectral performance of a whole-body research photon counting detector CT: quantitative accuracy in derived image sets. *Physics in Medicine and Biology*, 62(17):7216 – 7232, 2017.

[11] A. Brambilla, P. Ouvrier-Buffer, J. Rinkel, G. Gonon, C. Boudou, and L. Verger. CdTe linear pixel x-ray detector with enhanced spectrometric performance for high flux x-ray imaging. In *IEEE Nuclear Science Symposium Conference Record*, pages 4825–4828, 2011.

[12] L. A. Feldkamp, L. C. Davis, and J. W. Kress. Practical cone-beam algorithm. *Journal of the Optical Society of America A*, 1(6):612–619, 1984.

[13] M. Beister, D. Kolditz, and W. Kalender. Iterative reconstruction methods in x-ray CT. *Physica medica*, 28(2):94–108, 2012.

[14] C. Maaß, M. Baer, and M. Kachelrieß. Image-based dual energy CT using optimized precorrection functions: A practical new approach of material decomposition in image domain. *Medical Physics*, 36(8):3818–3829, 2009.

[15] J.P. Schlomka, E. Roessl, R. Dorscheid, S. Dill, G. Martens, T. Istel, C. Bäumer, C. Herrmann, R. Steadman, G. Zeitler, A. Livne, and R. Proksa. Experimental feasibility of multi-energy photon-counting K-edge imaging in pre-clinical computed tomography. *Physics in Medicine and Biology*, 53(15):4031–4047, 2008.

[16] R. F. Barber, E. Y. Sidky, T. Gilat-Schmidt, and X. Pan. An algorithm for constrained one-step inversion of spectral ct data. *Physics in Medicine and Biology*, 61(10):3784–3818, 2016.

[17] J. Siewerdsen and D. Jaffray. Cone-beam computed tomography with a flat-panel imager: Magnitude and effects of x-ray scatter. *Medical Physics*, 28(2):220–231, 2001.

[18] E. P. Rührnschopf and K. Klingenbeck. A general framework and review of scatter correction methods in x-ray cone-beam computerized tomography. Part 1: Scatter compensation approaches. *Medical Physics*, 38(7):4296–4311, 2011.

[19] E. P. Rührnschopf and K. Klingenbeck. A general framework and review of scatter correction methods in cone beam CT. Part 2: Scatter estimation approaches. *Medical Physics*, 38(9):5186–5199, 2011.

[20] J. H. Siewerdsen, D. J. Moseley, B. Bakhtiar, S. Richard, and D. A. Jaffray. The influence of antiscatter grids on soft-tissue detectability in cone-beam computed tomography with flat-panel detectors. *Medical Physics*, 31(12):3506–3520, 2004.

[21] J. A. Sorenson and J. Floch. Scatter rejection by air gaps: An empirical model. *Medical Physics*, 12(3):308–316, 1985.

[22] J. Persliden and G. A. Carlsson. Scatter rejection by air gaps in diagnostic radiology. Calculations using a Monte Carlo collision density method and consideration of molecular interference in coherent scattering. *Physics in Medicine and Biology*, 42(1):155–175, 1997.

[23] C. J. Lai, L. Chen, H. Zhang, X. Liu, Y. Zhong, Y. Shen, T. Han, S. Ge, Y. Yi, T. Wang, W. Yang, G. Whitman, and C. Shaw. Reduction in x-ray scatter and radiation dose for volume-of-interest (VOI) cone beam breast CT—a phantom study. *Physics in medicine and Biology*, 54(21):6691–6709, 2009.

[24] L. Chen, C. Shaw, M. Altunbas, C.J. Lai, X. Liu, T. Han, T. Wang, Wei T. Yang, and Gary J. Whitman. Feasibility of volume-of-interest (VOI) scanning technique in cone beam breast CT—a preliminary study. *Medical Physics*, 35(8):3482–3490, 2008.

[25] R. Clackdoyle and M. Defrise. Tomographic Reconstruction in the 21st Century. *IEEE Signal Processing Magazine*, 27(4):60–80, 2010.

[26] M. Altunbas and A Haibel. Compensation of ring artefacts in synchrotron tomographic images. *Optics Express*, 14(25):12071–12075, 2006.

[27] J. Wiegert, S. Hohmann, and M. Bertram. Iterative scatter correction based on artifact assessment. In *Medical Imaging 2008: Physics of Medical Imaging*, volume 6913, page 69132B. International Society for Optics and Photonics, 2008.

[28] Y. Kyriakou, M. Meyer, R. Lapp, and W. A. Kalender. Histogram-driven cupping correction (HDCC) in CT. In *Medical Imaging 2010: Physics of Medical Imaging*, volume 7622, page 76221S. International Society for Optics and Photonics, 2010.

[29] J. Maier, S. Sawall, M. Knaup, and M. Kachelrieß. Deep scatter estimation (DSE): Accurate real-time scatter estimation for x-ray CT using a deep convolutional neural network. *Journal of Nondestructive Evaluation*, 37(3):57, 2018.

[30] D. C. Hansen, G. Landry, F. Kamp, M. Li, C. Belka, K. Parodi, and C. Kurz. ScatterNet: A convolutional neural network for cone-beam CT intensity correction. *Medical Physics*, 45(11):4916–4926, 2018.

[31] S. Xie, C. Yang, Z. Zhang, and H. Li. Scatter artifacts removal using learning-based method for CBCT in IGRT system. *IEEE Access*, 6:78031–78037, 2018.

[32] Y. Nomura, Q. Xu, H. Shirato, S. Shimizu, and L. Xing. Projection-domain scatter correction for cone beam computed tomography using a residual convolutional neural network. *Medical Physics*, 46(7):3142–3155, 2019.

[33] L. A. Love and R. A. Kruger. Scatter estimation for a digital radiographic system using convolution filtering. *Medical Physics*, 14(2):178–185, 1987.

[34] J. A. Seibert and J. M. Boone. X-ray scatter removal by deconvolution. *Medical Physics*, 15(4):567–575, 1988.

[35] J. Rinkel, L. Gerfault, F. Estève, and J. M. Dinten. A new method for x-ray scatter correction: first assessment on a cone-beam CT experimental setup. *Physics in Medicine and Biology*, 52(15):4633–4652, 2007.

[36] M. Sun and J. M. Star-Lack. Improved scatter correction using adaptive scatter kernel superposition. *Physics in Medicine and Biology*, 55(22):6695–6720, 2010.

[37] E Meyer, C Maas, M Baer, R Raupach, B Schmidt, and M Kachelrieß. Empirical scatter correction (esc): A new CT scatter correction method and its application to metal artifact reduction. In *IEEE Nuclear Science Symposuim and Medical Imaging Conference*, pages 2036–2041. IEEE, 2010.

[38] C. Kim, M. Park, Y. Sung, J. Lee, J. Choi, and S. Cho. Data consistency-driven scatter kernel optimization for x-ray cone-beam CT. *Physics in Medicine and Biology*, 60(15):5971–5994, 2015.

[39] M. Hoffmann, T. Würfl, N. Maaß, F. Dennerlein, A. Aichert, and A. Maier. Empirical scatter correction using the epipolar consistency condition. In *CT-Meeting*, 2018.

[40] J. H. Mason, A. Perelli, W. H. Nailon, and M. E. Davies. Quantitative cone-beam CT reconstruction with polyenergetic scatter model fusion. *Physics in Medicine and Biology*, 63(22):225001, 2018.

[41] E. Mainegra-Hing and I. Kawrakow. Fast Monte Carlo calculation of scatter corrections for CBCT images. *Journal of Physics: Conference Series*, 102:012017, 2008.

[42] G. Poludniowski, P. M. Evans, V. N. Hansen, and S. Webb. An efficient Monte Carlo-based algorithm for scatter correction in keV cone-beam CT. *Physics in Medicine and Biology*, 54(12):3847–3864, 2009.

[43] G. Jarry, S. A. Graham, D. A. Jaffray, D. J. Moseley, and F. Verhaegen. Scatter correction for kilovoltage cone-beam computed tomography (CBCT) images using Monte Carlo simulations. In *Medical Imaging 2006: Physics of Medical Imaging*, volume 6142, page 614254. International Society for Optics and Photonics, 2006.

[44] E. Mainegra-Hing and I. Kawrakow. Variance reduction techniques for fast Monte Carlo CBCT scatter correction calculations. *Physics in Medicine and Biology*, 55(16):4495–4507, 2010.

[45] G. J. Bootsma, F. Verhaegen, and D. A. Jaffray. Efficient scatter distribution estimation and correction in CBCT using concurrent Monte Carlo fitting. *Medical Physics*, 42(1):54–68, 2015.

[46] R. Ning, X. Tang, and D. Conover. X-ray scatter correction algorithm for cone beam CT imaging. *Medical Physics*, 31(5):1195–1202, 2004.

[47] W. Cai, R. Ning, and D. L. Conover. Simplified method of scatter correction using a beam-stop-array algorithm for cone-beam computed tomography breast imaging. *Optical Engineering*, 47(9):097003, 2008.

[48] A. Peterzol, J. M. Létang, and D. Babot. A beam stop based correction procedure for high spatial frequency scatter in industrial cone-beam x-ray CT. *Nuclear Instruments and Methods in Physics Research Section B: Beam Interactions with Materials and Atoms*, 266(18):4042–4054, 2008.

[49] J. H. Siewerdsen, M. J. Daly, B. Bakhtiar, D. J. Moseley, S. Richard, H. Keller, and D. A. Jaffray. A simple, direct method for x-ray scatter estimation and correction in digital radiography and cone-beam CT. *Medical Physics*, 33(1):187–197, 2006.

[50] B. Meng, H. Lee, L. Xing, and B. P. Fahimian. Single-scan patient-specific scatter correction in computed tomography using peripheral detection of scatter and compressed sensing scatter retrieval. *Medical Physics*, 40(1):011907, 2013.

[51] L. Zhu, N. Strobel, and R. Fahrig. X-ray scatter correction for cone-beam CT using moving blocker array. In *Medical Imaging 2005: Physics of Medical Imaging*, volume 5745, pages 251–258. International Society for Optics and Photonics, 2005.

[52] X Liu, C. C. Shaw, T. Wang, L. Chen, M. C. Altunbas, and S. C. Kappadath. An accurate scatter measurement and correction technique for cone beam breast CT imaging using scanning sampled measurement (SSM) Technique. In *Medical Imaging 2006: Physics of Medical Imaging*, volume 6142, pages 6142341–6142347. International Society for Optics and Photonics, 2006.

[53] H. Yan, X. Mou, S. Tang, Q. Xu, and M. Zankl. Projection correlation based view interpolation for cone beam CT: primary fluence restoration in scatter measurement with a moving beam stop array. *Physics in Medicine and Biology*, 55(21):6353–6375, 2010.

[54] J. Wang, W. Mao, and T. Solberg. Scatter correction for cone-beam computed tomography using moving blocker strips: a preliminary study. *Medical Physics*, 37(11):5792–5800, 2010.

[55] L. Ouyang, K. Song, and J. Wang. A moving blocker system for cone-beam computed tomography scatter correction. *Medical Physics*, 40(7):071903, 2013.

[56] T. Lee, C. Lee, J. Baek, and S. Cho. Moving beam-blocker-based low-dose cone-beam CT. *IEEE Transactions on Nuclear Science*, 63(5):2540–2549, 2016.

[57] X. Liang, Y. Jiang, W. Zhao, Z. Zhang, C. Luo, J. Xiong, S. Yu, X. Yang, J. Sun, Q. Zhou, T. Niu, and Y. Xie. Scatter correction for a clinical cone-beam CT system using an optimized stationary beam blocker in a single scan. *Medical Physics*, 46(7):3165–3179, 2019.

[58] H. Lee, L. Xing, R. Lee, and B. P. Fahimian. Scatter correction in cone-beam CT via a half beam blocker technique allowing simultaneous acquisition of scatter and image information. *Medical Physics*, 39(5):2386–2395, 2012.

[59] Y. Zhou, T. Mathur, and S. Molloi. Scatter and veiling glare estimation based on sampled primary intensity. *Medical Physics*, 26(11):2301–2310, 1999.

[60] K. Yang, G. Burkett, and J. M. Boone. A breast-specific, negligible-dose scatter correction technique for dedicated cone-beam breast CT: a physics-based approach to improve Hounsfield Unit accuracy. *Physics in Medicine and Biology*, 59(21):6487–6505, 2014.

[61] K. Schörner, M. Goldammer, and J. Stephan. Comparison between beam-stop and beam-hole array scatter correction techniques for industrial x-ray cone-beam CT. *Nuclear Instruments and Methods in Physics Research Section B: Beam Interactions with Materials and Atoms*, 269(3):292–299, 2011.

[62] A. Sossin, V. Rebuffel, J. Tabary, J. M. Létang, N. Freud, and L. Verger. A novel scatter separation method for multi-energy x-ray imaging. *Physics in Medicine and Biology*, 61(12):4711–4728, 2016.

[63] A. Sossin, V. Rebuffel, J. Tabary, J. M. Létang, N. Freud, and L. Verger. Experimental validation of a multi-energy x-ray adapted scatter separation method. *Physics in Medicine and Biology*, 61(24):8625–8639, 2016.

[64] L. Zhu, N. R. Bennett, and R. Fahrig. Scatter correction method for x-ray CT using primary modulation: Theory and preliminary results. *IEEE Transactions on Medical Imaging*, 25(12):1573–1587, 2006.

[65] J. S. Maltz, W. E. Blanz, D. Hristov, and A. Bani-Hashemi. Cone beam x-ray scatter removal via image frequency modulation and filtering. In *2005 IEEE Engineering in Medicine and Biology 27th Annual Conference*, volume 2, pages 1854–1857, 2005.

[66] H. Gao, R. Fahrig, N. R. Bennett, M. Sun, J. Star-Lack, and L. Zhu. Scatter correction method for x-ray CT using primary modulation: Phantom studies. *Medical Physics*, 37(2):934–946, 2010.

[67] H. Gao, L. Zhu, and R. Fahrig. Modulator design for x-ray scatter correction using primary modulation: Material selection. *Medical Physics*, 37(8):4029–4037, 2010.

[68] H. Gao, L. Zhang, R. Grimmer, and R. Fahrig. Physics-based spectral compensation algorithm for x-ray CT with primary modulator. *Physics in Medicine and Biology*, 64(12):125006, 2019.

[69] L Ritschl, R. Fahrig, M. Knaup, J. Maier, and M. Kachelrieß. Robust primary modulation-based scatter estimation for cone-beam CT. *Medical Physics*, 42(1):469–478, 2015.

[70] Y. Chen, Y. Song, J. Ma, and J. Zhao. Optimization-based scatter estimation using primary modulation for computed tomography. *Medical Physics*, 43(8Part1):4753–4767, 2016.

[71] B. Bier, M. Berger, A. Maier, M. Kachelrieß, L. Ritschl, K. Müller, J.H. Choi, and R. Fahrig. Scatter correction using a primary modulator on a clinical angiography C-arm CT system. *Medical Physics*, 44(9):e125–e137, 2017.

[72] A. Sossin, V. Rebuffel, and J. Tabary. Method for correcting a spectrum (patent number 10079078). US Patent 10,079,078.

[73] J. A. Nelder and R. Mead. A Simplex Method for Function Minimization. *The Computer Journal*, 7(4):308–313, 1965.

[74] M. Unser, A. Aldroubi, and M. Eden. B-spline signal processing. I. Theory. *IEEE Transactions on Signal Processing*, 41(2):821–833, 1993.

[75] P. Charbonnier, L. Blanc-Feraud, G. Aubert, and M. Barlaud. Deterministic edge-preserving regularization in computed imaging. *IEEE Transactions on Image Processing*, 6(2):298–311, 1997.

[76] H. G. Menzel, C. Clement, and P. DeLuca. ICRP Publication 110. Realistic reference phantoms: an ICRP/ICRU joint effort. A report of adult reference computational phantoms. *Annals of the ICRP*, 39(2):1–164, 2009.

[77] S. Jan, D. Benoit, E. Becheva, T. Carlier, F. Cassol, P. Descourt, T. Frisson, L. Grevillot, L. Guigues, L. Maigne, C. Morel, Y. Perrot, N. Rehfeld, D. Sarrut, D. R. Schaart, S. Stute, U. Pietrzyk, D. Visvikis, N. Zahra, and I. Buvat. GATE V6: a major enhancement of the GATE simulation platform enabling modelling of CT and radiotherapy. *Physics in Medicine and Biology*, 56(4):881–901, 2011.

[78] S. Rit, M. V. Oliva, S. Brousmiche, R. Labarbe, D. Sarrut, and G. C. Sharp. The Reconstruction Toolkit (RTK), an open-source cone-beam CT reconstruction toolkit based on the Insight Toolkit (ITK). *Journal of Physics: Conference Series*, 489:012079, 2014.

[79] P. Paleo and A. Mirone. Ring artifacts correction in compressed sensing tomographic reconstruction. *Journal of Synchrotron Radiation*, 22(Pt 5):1268–1278, 2015.

[80] L Yan, T Wu, S Zhong, and Q Zhang. A variation-based ring artifact correction method with sparse constraint for flat-detector CT. *Physics in Medicine and Biology*, 61(3):1278–1292, 2016.

[81] S Titarenko, P J. Withers, and A Yagola. An analytical formula for ring artefact suppression in x-ray tomography. *Applied Mathematics Letters*, 23(12):1489–1495, 2010.

[82] S. Titarenko, V. Titarenko, A. Kyrieleis, P. Withers, and F. De Carlo. Suppression of ring artefacts when tomographing anisotropically attenuating samples. *Journal of Synchrotron Radiation*, 18(3):427–435, 2011.

[83] Y Kim, J Baek, and D Hwang. Ring artifact correction using detector line-ratios in computed tomography. *Optics Express*, 22(11):13380–13392, 2014.

[84] B Münch, P Trtik, F Marone, and M Stampanoni. Stripe and ring artifact removal with combined wavelet–Fourier filtering. *Optics Express*, 17(10):8567–8591, 2009.

[85] E. X. Miqueles, J. Rinkel, F. O'Dowd, and J. S. V. Bermúdez. Generalized Titarenko's algorithm for ring artefacts reduction. *Journal of Synchrotron Radiation*, 21(6):1333–1346, 2014.

[86] J. Lesaint. *Data consistency conditions in x-ray transmission imaging and their application to the self-calibration problem.* PhD thesis, 2018.

FOLIO ADMINISTRATIF

THESE DE L'UNIVERSITE DE LYON OPEREE AU SEIN DE L'INSA LYON

NOM : PIVOT DATE de SOUTENANCE : 22/11/2019

Prénoms : Odran

TITRE : Scatter correction for spectral computed tomography

NATURE : Doctorat Numéro d'ordre : 2019LYSEI102

Ecole doctorale : EEA

Spécialité : Traitement du Signal et de l'Image

RESUME :
Scattered radiation is a major cause of bias, loss of contrast and artifacts in x-ray computed tomography (CT). Many correction methods have been proposed for conventional CT (using energy-integrating detectors) but it is still an open research topic in the field of spectral CT, a novel imaging technique based on the use of energy selective photon counting detectors. The main objective of the present thesis was to investigate scatter correction techniques adapted to spectral CT. The chosen solution refines a scatter correction method developed for integration-mode CT which uses a semi-transparent primary modulator mask. The attenuation of the primary modulator mask is first compensated for with a correction matrix which takes advantage of the spectral information. The other contributions are a scatter model based on B-splines allowing an accurate representation of scatter maps with the aid of a very few parameters and a cost function which takes into account the structures of the mask and the object. The accuracy of the correction matrix, the scatter model and the whole proposed scatter correction process were tested on simulated data and have shown a significant bias reduction, contrast enhancement and artifact removal. In addition, physical experiments were performed using a parallel fan-beam set-up with a commercial energy-resolved detector. The method was successfully validated in the case of two phantoms dedicated to medical image quality measurements, with a remarkable improvement.

MOTS-CLÉS :
Scatter, spectral CT, photon counting detector, primary modulation

Laboratoires de recherche :
CEA/LETI et CREATIS

Directeur de thèse:

LÉTANG, Jean Michel	Maître de Conférences HDR (INSA Lyon)	

Président de jury :

RODET, Thomas	Professeur (ENS CACHAN)	

Composition du jury :

BUVAT, Irène	Directeur de recherche (Université Paris Sud)	Rapporteure
MAIER, Andreas	Professeur (FAU Erlangen-Nürnberg)	Rapporteur
DESBAT, Laurent	Professeur (Université Grenoble Alpes)	Examinateur
FOURNIER, Clarisse	Ingénieur chercheur (CEA/LETI)	Invitée
TABARY, Joachim	Ingénieur chercheur (CEA/LETI)	Invité
RIT, Simon	Chargé de recherche (CNRS)	Invité